MASTERARBEIT | MASTER'S THESIS

Titel | Title

Stellar activity characterisation of Ariel targets

verfasst von | submitted by

Isabella Wizani BSc

angestrebter akademischer Grad | in partial fulfilment of the requirements for the degree of

Master of Science (MSc)

Wien | Vienna, 2024

Studienkennzahl lt. Studienblatt | Degree programme code as it appears on the student record sheet:	UA 066 861
Studienrichtung lt. Studienblatt | Degree programme as it appears on the student record sheet:	Masterstudium Astronomie
Betreut von | Supervisor:	Ass.-Prof. Dr. Sudeshna Boro Saikia

Stellar activity characterisation of Ariel targets

Isabella Wizani, BSc

Abstract

The chromospheric activity of a star is triggered by its magnetic field. Stellar activity is an important parameter in the observation of exoplanets. Strong activity of the star can impact the habitability of the planet and the characterisation of the planetary atmosphere (Danielski et al., 2022; Bellotti et al., 2024). The determination of stellar activity is therefore important for the ARIEL mission, that will observe over a thousand exoplanets (Tinetti et al., 2018). In this work, the activity of 127 F-G-K-M stars from the ARIEL target catalogue was determined. For this purpose, the Mount-Wilson S-index and based on this, the $\log R'_{\mathrm{HK}}$ values of the stars were calculated. The Mount-Wilson S-index uses a ratio of the line fluxes in the Calcium II H and K lines over the fluxes of two nearby continuum bands. The Calcium II H and K lines can show emission in the cores of broad absorption wings. The strength of the emission is considered an indicator of the activity of a star. The hotter stars in this work show higher $\log R'_{\mathrm{HK}}$ values than the cooler stars. However, the cooler stars also have a greater scatter of $\log R'_{\mathrm{HK}}$ values. The spectra were also manually sorted into two groups based on an existence of an emission feature. Even though the analysed F-stars have high $\log R'_{\mathrm{HK}}$ values, they do not show any emission in the Calcium II H and K lines. In conclusion the high values are most likely caused by rotational line broadening due to their fast rotations.

Zusammenfassung

Die chromosphärische Aktivität eines Sternes wird durch dessen Magnetfeld ausgelöst. Sternaktivität ist ein wichtiger Parameter bei der Beobachtung von Exoplaneten. Starke Aktivität des Sterns kann die Habitabilität des Planeten und die Charakterisierung der planetaren Atmosphäre beeinflussen (Danielski et al., 2022; Bellotti et al., 2024). Die Bestimmung der stellaren Aktivität ist dadurch für die ARIEL Mission, die über tausend Exoplaneten beobachten wird, von Bedeutung (Tinetti et al., 2018). In dieser Arbeit wurde die Aktivität von 127 F-G-K-M Sternen des Input-Kataloges der ARIEL Mission bestimmt. Dazu wurde der Mount-Wilson S-index und der darauf basierende $\log R'_{\mathrm{HK}}$ Wert der Sterne berechnet. Für den Mount-Wilson S-index wird ein Verhältnis der Flüsse der Calcium II H und K Linien zu den Flüssen zweier naheliegender Kontinuumsbänder bestimmt. Die Calcium II H und K Linien können eine Emissionslinie in den Kernen der breiten Absorptionslinien aufweisen. Die Stärke der Emission gilt dabei als Indikator für die Aktivität eines Sterns. Die heißeren Sterne in dieser Arbeit weisen dabei höhere $\log R'_{\mathrm{HK}}$ Werte auf, als die kühleren Sterne. Allerdings weisen die kühleren Sterne auch eine größere Streuung der $\log R'_{\mathrm{HK}}$ Werte auf. Die Spektren wurden manuell in zwei Gruppen eingeteilt, basierend auf der Existenz einer Emission. Obwohl die analysierten F-Sterne höhere $\log R'_{\mathrm{HK}}$ Werte aufweisen, zeigen sie in ihren Spektren keine sichtbare Emission in den Calcium II H und K Linien. Die hohen Werte werden wahrscheinlich durch eine Rotationsverbreiterung der Linien erzeugt, die durch deren schnelle Rotation ausgelöst wird.

Contents

1 Stellar activity **11**

1.1 Introduction 11

1.2 Solar magnetic field and activity 11

1.3 Stellar magnetic fields and activity 14

1.3.1 Spectral lines in the chromosphere 14

1.3.2 Calcium lines 15

1.3.3 Magnesium lines 15

1.3.4 Hydrogen lines 16

1.4 The Mount Wilson survey of stellar chromospheric activity 16

1.5 The Ariel space mission 17

2 Data collection and analysis **19**

2.1 Observation 19

2.1.1 HARPS 19

2.1.2 HARPS-N 19

2.1.3 UVES 20

2.1.4 The spectra 20

2.1.5 Luminosity classes 22

2.1.6 Orbital parameters 22

2.1.7 Solar analogues 25

2.2 Calibration 25

3 Methods **29**

3.1 The Mount Wilson S-index 29

3.2 Colour-independence 30

3.3 Photospheric Contribution 33

3.4 Hα-index 34

4 Results **35**

4.1 S-index calibration 35

4.2 Temperature dependence of S_{MWO} 37

4.3 Solar-analogues 37

4.4 $\log R'_{\mathrm{HK}}$ values 38

4.5 Temperature and $\log R'_{\mathrm{HK}}$ . . . 41
4.6 Metallicity and $\log R'_{\mathrm{HK}}$ . . . 41
4.7 Visible Ca II HK emission and $\log R'_{\mathrm{HK}}$ . . . 41
4.7.1 Rotation . . . 43
4.7.2 Age . . . 45
4.8 Most active star . . . 47
4.9 Hα-index . . . 47

5 Conclusion **49**

A Tables **53**

List of Figures

1.1 Solar butterfly diagram. Image taken from Hathaway (2015) under the terms of the Creative Commons Attribution 4.0 International License 12
1.2 Sunspot, Plage and Flare. Image taken from Hall (2008) under the terms of the Creative Commons Attribution 4.0 International License 14
1.3 Sketch of the triangle bandpass at the Ca II K line 17

2.1 Two spectra with different SNR 21
2.2 Two spectra with and without emission 21
2.3 Spectra with the used bandpasses for the S_{MWO} 22
2.4 Effective temperature vs. surface gravity 23
2.5 Positions of the stars 24
2.6 Computed orbit of a star 25
2.7 Histograms of orbital parameters 26

3.1 Peaks of the black body radiation. Image taken from Marvin et al. (2023) under the terms of the Creative Commons Attribution 4.0 International License. 32

4.1 S_{MWO} calibrations 36
4.2 Effective temperature vs. S_{MWO} 38
4.3 Effective temperature vs. S_{SA} 39
4.4 Histogram of $\log R'_{\text{HK}}$ 40
4.5 Histogram of $\log R'_{\text{HK}}$ for F-, G- and K-stars 40
4.6 Effective temperature vs. $\log R'_{\text{HK}}$ 42
4.7 Metallicity vs. $\log R'_{\text{HK}}$ 43
4.8 Spectral type vs. $\log R'_{\text{HK}}$, separated by the emission group 44
4.9 Effective temperature vs. $\log R'_{\text{HK}}$, coloured by the emission group 44
4.10 Effective temperature vs. $\log R'_{\text{HK}}$, coloured by the rotation period 46
4.11 Effective temperature vs. $\log R'_{\text{HK}}$, coloured by age 46
4.12 Hα-index vs. S_{MWO} of the Ariel sample 48
4.13 S_{SA} vs. Hα-index 48

Chapter 1

Stellar activity

1.1 Introduction

Since the first detection of an exoplanet by Mayor and Queloz (1995) over 5800[1] exoplanets are confirmed today. Knowing the parameters of the host stars is crucial for the characterisation of exoplanets (Brucalassi et al., 2022). Especially the activity of the star can affect the characterisation of the planets atmosphere (Danielski et al., 2022). Strong magnetic activity can put the planets habitability at risk, since it is connected to phenomena which can change the chemical composition of the atmosphere (Bellotti et al., 2024). Magnetized stellar winds are also responsible for an exoplanets atmospheric loss (Boro Saikia et al., 2023). Therefore, knowledge about the activity of host stars is important so the effects caused by it can be corrected (Tinetti et al., 2018). The term stellar activity is very general and covers a wide range of phenomena that occur in the individual layers of the stellar atmosphere. This work focuses on the chromospheric activity triggered by the magnetic field of the star.

1.2 Solar magnetic field and activity

The suns atmosphere is commonly divided into four layers. Starting from the outermost layer, the layers are referred to as the corona, the transition region, the chromosphere and the photosphere (Mariska, 1992). This work focuses on the magnetic field of the chromosphere. As discussed in Carlsson et al. (2019) and Pietrow (2022), in the chromosphere the density decreases exponentially with height. In the underlying photosphere the gas pressure usually dominates over the magnetic pressure, at least outside of strong magnetic concentrations. But due to the much lower density in the upper chromosphere, the gas pressure is no longer dominant. Here the magnetic field defines the dynamics. Due to the decreasing gas pressure, the magnetic field is able to spread horizontally, which means that at some height the entire chromosphere is covered by the magnetic field, even at regions where the magnetic field in the underlying photosphere is very weak (Carlsson et al., 2019).

The sun is the only star where the magnetic field can be studied with great spatial resolution

[1] `https://exoplanetarchive.ipac.caltech.edu/`

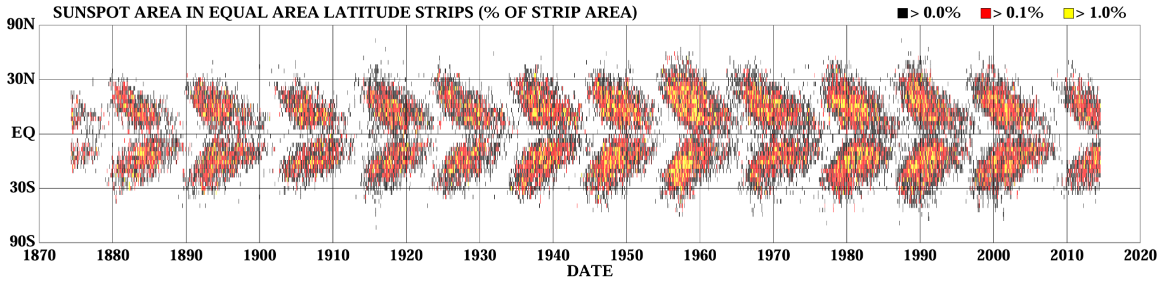

Figure 1.1: Solar butterfly diagram. The sunspots appear approximately between a latitude of 20° to 25° at the beginning of a cycle. Within the cycle they spread out more and they also move closer to the equator (Hathaway, 2015). Image taken from Hathaway (2015) under CC BY 4.0.

and nearly constant time coverage (Basri, 2021). To create a magnetic field, the star must rotate, needs convection and a conducting fluid (Basri, 2021). The generation of the solar magnetic field can be described by a $\alpha\Omega$ dynamo (Brun and Browning, 2017). The "α"-effect, which describes a rising and twisting motion of the magnetic field lines (Engvold et al., 2019). The "Ω" effect causes a stretching of the magnetic field lines by differential rotation (Brun and Browning, 2017). In general, the mean large-scale solar magnetic field can be split into two components, the toroidal and the poloidal component (Schrijver and Zwaan, 2000). The toroidal field is an east-west oriented field, whereas the poloidal field lines emerge from one polar cap to the other (Babcock, 1961; Fan, 2009). The problem within the dynamo theory is the change in polarity, or more precisely how a toroidal field is generated from a pre-existing poloidal field, and vice versa (Charbonneau, 2010). The $\alpha\Omega$ dynamo uses the "α" effect to create a poloidal field and the "Ω" effect to create the toroidal field (Engvold et al., 2019). Certainly, the sun was the first star for which a magnetic field could be observed, but it surely isn't an exception.

The dynamo process leads to the magnetic solar cycle. In 1908, George Hale first detected the solar magnetic field when he observed Zeeman splitting in spectral lines of sunspots (Hale, 1908). A few years later, in 1919, he also discovered that sunspots in the northern hemisphere have an opposite polarization to the ones on the southern hemisphere and that the polarities change after a sunspot-minimum (Hale et al., 1919). This happens every 11 years and the so-called "Hale-cycle" consists of two sunspot cycles and is therefore 22 years long (Gil and Mursula, 2017). Apart from that, the minimum and maximum of sunspots also follow an average cycle of 11 years (Basri, 2021). By using a so-called "butterfly diagram", which can be seen in Figure 1.1, it becomes clear that the spots are not randomly distributed over the solar surface, but rather appear at two mid-latitude bands, approximately 20° - 25°, at the beginning of a cycle. As the cycle continues, the bands are getting wider and move towards the solar equator. Additionally, the solar polar fields are linked to the sunspot cycle, but are out of phase. The polar field's strength reaches its maximum, when the number of spots is at a minimum, and they reverse their polarity when the number of spots is at a maximum (Hathaway, 2015).

On the sun, different phenomena caused by the magnetic field over a solar cycle can directly be seen. Regions where the average magnetic field is stronger than in the quiet sun are called “active regions” (Carlsson et al., 2019). These active regions are for example sunspots, faculae, plages or flares (Basri, 2021).

The continuous record of sunspots began around 1849, even though general observations have been made earlier, and it is the oldest indicator of solar activity (Ferreira et al., 2024). Sunspots appear as darker and cooler spots with the strongest magnetic fields. They are surrounded by the so-called penumbra, a lighter radially extending structure, while the even darker core is called the umbra (Pietrow, 2022). They are created when magnetic lines intersect the photosphere and suppress the convective plasma, causing the energy transport to be restrained (Johnson, 2024). An example of a sunspot in the photosphere can be seen in the upper left panel of Figure 1.2 (Hall, 2008).

Active regions do not necessarily have to be darker than their surroundings. Faculae for example are brighter regions and can usually be seen near the limb (Hall, 2008). They are surrounding the sunspots and cause an even greater change in brightness, so that the sun appears brightest when there is a maximum number of spots (Johnson, 2024).

The chromospheric counterparts of faculae are the so-called plages (Hall, 2008). As discussed in Carlsson et al. (2019), they appear at the footpoints of most coronal loops and are the brightest regions of the chromosphere. They are even relevant for the upper atmosphere of Earth, since they are an important contribution to the UV emission of the star. Furthermore, plages induce flux variations in the emission cores of the Calcium II H and K lines, that are of interest in this work (Berdyugina, 2005). In the upper right panel of Figure 1.2 an example of a plage can be seen. It shows the same area at the same time as the top left panel, but now in the chromosphere instead of the photosphere (Hall, 2008).

If energy in the stellar atmosphere gets suddenly released it is called a “flare” (Engvold et al., 2019). From time to time, magnetic field lines need to reconnect into a simpler form in order to get rid of a stressed configuration and by doing so, energy gets released (Basri, 2021). With accelerated particles the energy gets carried back to the chromosphere or further into interplanetary space. Another phenomena, that sometimes occurs together with flares are coronal mass ejections (CMEs) (Benz and Güdel, 2010). They are massive solar plasma ejections due to disruptions of coronal loops. CMEs can cause losses of planetary atmospheres and are responsible for the Earths aurorae. Flares and CMEs are both energetic events (Basri, 2021). The magnetic energy in the corona is linked to the magnetic fields in the photosphere, therefore flares occur above or near photospheric active regions (Benz and Güdel, 2010). In the bottom panel of Figure 1.2 an example of a flare can be seen. The flare took place two days after the images of the top panels were taken (Hall, 2008).

For other stars the observations of the magnetic field is not as easy due to the lack of spatial and temporal resolution (Basri, 2021). Therefore, other techniques need to be used, for example the study of chromospheric activity by observing the Calcium II H and K lines, which is discussed in this work.

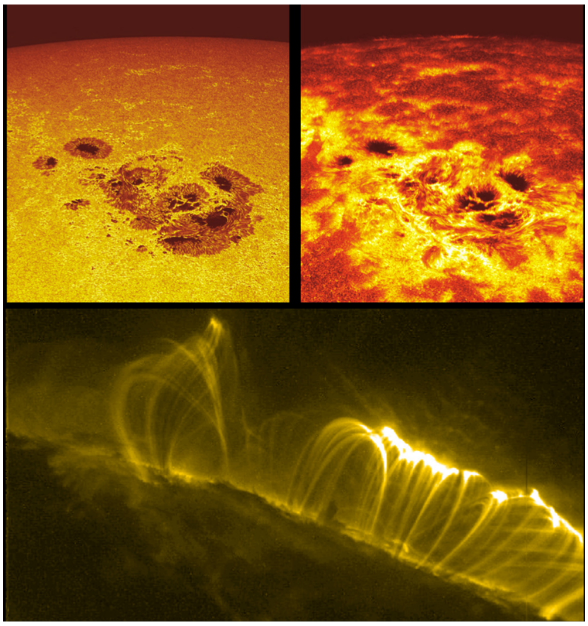

Figure 1.2: Top left: An example of a sunspot in the photosphere can be seen. They appear as dark, cool spots. Top right: It shows the same are at the same time as the top left panel, but the chromosphere instead of the photosphere. Here the plages which typically lie under sunspots can be seen. Bottom panel: the image shows a flare, which took place two days after the images of the upper panels were taken (Hall, 2008). This Figure was taken from Hall (2008) under CC BY 4.0.

1.3 Stellar magnetic fields and activity

Studying the sun is important to understand different phenomena of stellar activity and the sun is for sure the best studied star. However, it is a star with particular parameters and only acts as one specific example. It is therefore important to study a variety of stars with different parameters to understand stellar activity as a whole (Hall, 2008; Basri, 2021). Stellar activity is also important for exoplanets, since the planets habitability can be at risk due to strong stellar activity and the exoplanets atmosphere can experience mass loss caused by magnetized stellar winds (Boro Saikia et al., 2023; Bellotti et al., 2024). For stars other than the sun, high-resolution observation or direct images of phenomena caused by activity are not available, so different approaches, like the formation of emission lines in the chromosphere, can be used (Hall, 2008; Basri, 2021).

1.3.1 Spectral lines in the chromosphere

In general an absorption line is formed when an electron gets excited into a higher energy level. This happens when the energy of a photon corresponds to the energy difference between the current energy level of the electron and a higher one. The photon gets absorbed, which results in less flux at the wavelength corresponding to the energy of the photon. This localised lack of flux can be observed as an absorption line. If an electron is already at a higher energy level and falls back to a lower energy level, then the corresponding energy gets released as a photon, resulting in an increase in flux at the corresponding wavelength, which in turn creates an emission line (Weigert, 2009; Hanslmeier, 2020).

As discussed in Hall (2008) and Linsky (2017), there are different ways in which a spectral line can be created, such as radiative or collisional processes. In sun-like chromospheres the dominating process for ionized metals is the collisional one, since it is linked to the local electron temperature. There are a few lines that arise as absorption lines in the photosphere, but also have a emission feature in their line cores, which originates in the chromosphere (Hall, 2008; Linsky, 2017). This is because the temperature drops in the photosphere, but rises again when it crosses the chromosphere, resulting in an emission feature of high-temperature ionized elements (Carlsson et al., 2019). This can for example be seen in the Ca II H and K lines or in the Mg h and k lines (Linsky, 2017).

1.3.2 Calcium lines

The Ca II H and K lines lie at 3968 Å and 3934 Å respectively (Baliunas et al., 1995). These lines show an emission feature in the cores of very broad absorption wings (Linsky, 2017). This spectral feature was also observed in stars other than the sun first by Eberhard and Schwarzschild (1913). At the center of the emission line is again an absorption feature, which gives them their distinctive M-shape (Engvold et al., 2019). The name Ca II already makes it clear that these lines occur from single ionized calcium atoms, which is the dominant ionisation stage in the chromosphere up to about 13 000 K (Hall, 2008; Carlsson et al., 2019). The line core center is formed high in the chromosphere, whereas the emission peak arises slightly below (Linsky, 2017). The strength of the emission features correlates with the activity level of a star. For regions with only low activity the emission lines are weak. In cases of a very quiet region, they may not even be observable. In contrast, in very active regions the lines can even exceed the local continuum (Linsky, 2017; Loaiza-Tacuri et al., 2024). They reflect the non-thermal heating of the chromosphere (Astudillo-Defru et al., 2017).

Since the Ca II H and K lines lie in the blue part of the optical wavelength range, it makes them accessible for ground-based observations (Pietrow, 2022). Due to the relatively short wavelength, a high diffraction-limited spatial resolution can be achieved. However, the low number of photons emitted by late-type stars around this wavelength also leads to a rather small signal-to-noise ratio (Carlsson et al., 2019). The Ca II H and K lines are also the spectral lines that were used in this work, to determine the chromospheric activity of a sample of stars (for further information see Section 1.4 and Chapter 3).

The Ca II IR triplet is also a popular indicator of chromospheric activity. Especially the line at 8542 Å is quite sensitive to the magnetic field (Carlsson et al., 2019). The opacity of the line is more temperature-dependent than the Ca II H and K lines, therefore it is a good indicator of the local temperature (Pietrow, 2022).

1.3.3 Magnesium lines

The Mg II h and k lines are also used as chromospheric diagnostic lines. They lie at 2803 Å and 2796 Å respectively and are correspondingly in the ultraviolet, which makes them unsuitable for ground-based observations (Carlsson et al., 2019; Pietrow, 2022). Like the Ca II

H and K lines, they consist of an emission peak within an absorption feature. Their emission would even be brighter since the background photosphere is weaker in the UV than in the optical (Linsky, 2017). Magnesium is also 15 times more abundant, which makes the lines more opaque compared to the Ca II H and K lines (Hall, 2008).

1.3.4 Hydrogen lines

The Hα line at 6562.8 Å is also often used as a diagnostic line for chromospheres (Linsky, 2017). Especially for late type stars, the position of this line is an advantage compared to the Ca II H and K lines, due to their black body energy distribution (Pasquini and Pallavicini, 1991). It is very temperature dependent and displays a very large thermal broadening, so that the line width works as a temperature diagnostic (Carlsson et al., 2019). With an increase in temperature the Hα line first shows deep absorption feature, but then fills to a more shallow absorption line, which can even result in an emission feature. This makes an interpretation of the absorption depth difficult (Linsky, 2017). Nevertheless, especially for M dwarfs, the line has some advantages. For instance, the continuum is much stronger compared to the Ca II H and K lines, and since there is no photospheric absorption it can be used without the need to subtract a photospheric contribution (Johnson, 2024).

1.4 The Mount Wilson survey of stellar chromospheric activity

As mentioned in Section 1.3.2, for this work the Calcium II H and K lines were used to determine the chromospheric activity of stars. Those specific lines were chosen because they form the foundation of the popular Mount Wilson survey. This survey is a commonly used catalogue of chromospheric activity. It was started by O.C. Wilson in March 1966 and contains measurements of numerous stars, which were observed over decades (Baliunas et al., 1995). The original idea behind the survey conducted by Wilson (1968, 1978) was to uncover potential chromospheric variability similar to the well-known solar cycle. The connection between the solar cycle and the number of sunspots was already known at that time, but since the change in luminosity between a minimum and a maximum of sunspots is rather small, a pure observation of a change in brightness would have been quite difficult. Therefore a different observing method needed to be carried out instead. Since the magnetic field is reflected by the strength of the Calcium II H and K lines, as already mentioned in Section 1.3.2, O.C. Wilson decided to use those lines as a proxy for the magnetic field (Wilson, 1968). More precisely, the survey determined the flux ratio of the Ca II H and K lines to two areas in the continuum on both sides of the lines. The observations were carried out at the Mount Wilson Observatory, thus the calculated value is therefore called Mount Wilson S-index (S_{MWO}). The identical names of O.C. Wilson and the Mount Wilson Observatory is pure coincidence (Wilson, 1968; Duncan et al., 1991; Baliunas et al., 1995).

As discussed by Vaughan et al. (1978) and Duncan et al. (1991), the survey was originally carried out using the 2.5 m telescope at the Mount Wilson Observatory in 1966. After 11 years, in April 1977, they got an improved instrument for the 1.5 m telescope, which they used from then on. The channels of the continuum bands were centered at 4001.07 Å for the so called R-band and at 3901.07 Å for the so called V-band and are 20 Å wide each. The

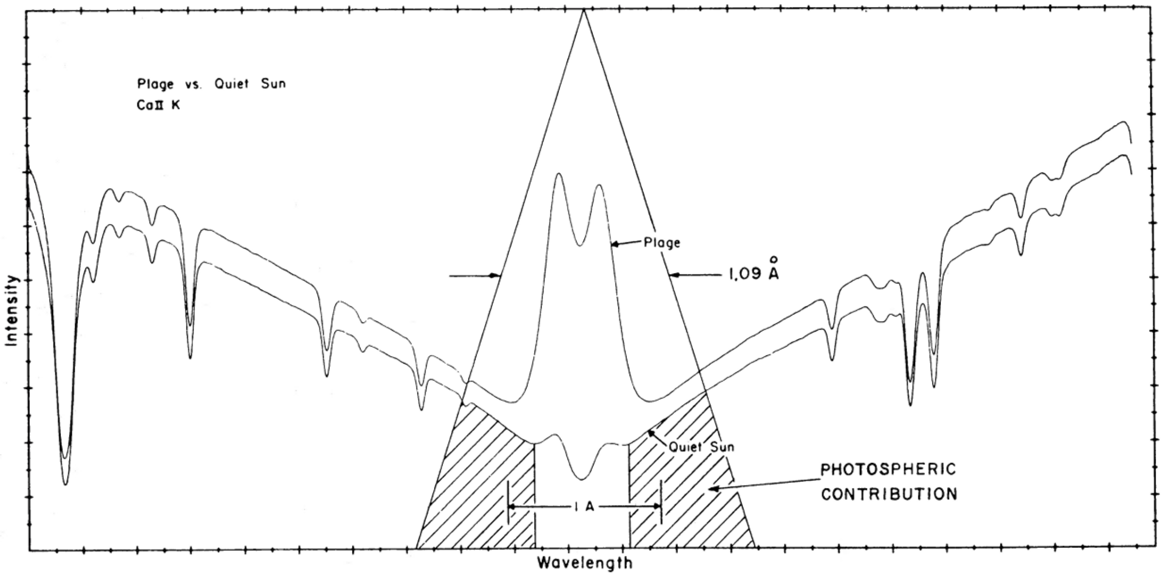

Figure 1.3: The instrumental profile at the Ca II K lines is a triangle with a FWHM of 1.09 Å. The sketch compares the spectral line of a quiet sun without emission to the spectral line of a more active star with an emission feature triggered by a plage. Also very clearly to see is the photospheric contributions, which needs to be subtracted. Sketch taken from Hartmann et al. (1984).

channels for the Ca II H and K lines were centered at the line cores. The entrance and the exit slit were 1 Å wide, which lead to a triangular instrumental profile with a FWHM of 1.09 Å. Figure 1.3 shows a sketch of the resulting triangular instrumental profile over the Ca K line, as seen by Hartmann et al. (1984). It compares the spectral line of a quiet sun with no emission at all to an active one with an emission feature triggered by a plage. The typical core absorption can also be seen. The sketch also shows the problematic of the photospheric contribution. The Mount-Wilson survey resulted in observations of over a thousand stars.

Nevertheless, the S_{MWO} has one disadvantage. The fluxes of the continuum bands are not the same for all spectral types, which means the S_{MWO} value is inherently colour dependent. Therefore, stars of different spectral types are not comparable. This problem was later solved by Noyes et al. (1984) and Hartmann et al. (1984). They established a value called the R'_{HK}. This is a continuation of the S_{MWO}, which contains a correction for the influence of the colour-dependence of the S-index. By this, stars of different spectral classes are now comparable with each other. They also subtracted the photospheric contribution, so that indeed only the chromospheric activity remains (Noyes et al., 1984; Hartmann et al., 1984; Marvin et al., 2023).

1.5 The Ariel space mission

The goal of this work is to analyse the stellar activity of a specific sample of stars. Those stars are part of the target catalogue of the Atmospheric Remote-sensing Infrared Exoplanet

Large-survey (ARIEL), which will be the next medium-class science mission, M4, of the European Space Agency. After the launch in 2029 Ariel will observe exoplanets and their host stars from the Lagrange point L2 (Tinetti et al., 2018; Magrini et al., 2022). Its focus lies in the observation of exoplanet atmospheres and determination of their chemical compositions. By studying about 1000 exoplanets of all types, Ariel will answer fundamental questions in the research area of exoplanets, e.g. what different planets are made of and how planets and their systems form or how their atmospheres evolve over time (Danielski et al., 2022). The main observing methods are transit, eclipse and phase-curved spectroscopy, while the spectra of the host stars and planets will be analysed in and out of transits. The signal of the planetary atmosphere can be as small as 10-100ppm relative to the star (Brucalassi et al., 2022). To achieve this, Ariel has to have knowledge not only about planetary parameters, but also about the stellar parameters. The spectrum of the host star needs to be as well known as the wanted signal of the planet to avoid misinterpreted results regarding the exoplanet, due to intrinsic stellar variations, e.g. triggered by the stellar magnetic field.

An exoplanet cannot be observed, without thinking about its star. Therefore obtaining an exact understanding of the stars parameters even before the launch of Ariel is crucial (Danielski et al., 2022; Brucalassi et al., 2022). Especially the activity level of the stars is important, since it is one of the greatest noise source, when it comes to observations of exoplanets and it can affect the planetary atmosphere characterisation. By knowing the intensity of the activity of the star, the influence on the Ariel observations can be evaluated (Danielski et al., 2022).

This work is organised as follows: in Chapter 2 the analysed archival data together with their observing telescopes are described. In Chapter 3 the method used, to determine the chromospheric activity is explained in detail. In Chapter 4 the results are presented as well as discussed and compared to already existing literature. In Chapter 5 a short conclusion of the work is presented.

Chapter 2

Data collection and analysis

This project used archival data collected by three high-resolution spectrographs, as discussed below. The sample consists a total of 127 stars and it contains one star of spectral type A, 46 F-type stars, 42 G-type stars, 33 K-type stars and 5 M-type stars. The sample was provided by the Ariel science consortium[1].

2.1 Observation

2.1.1 HARPS

Sixty-three stars, were observed with the High-Accuracy Radial velocity Planetary Searcher (HARPS). It is an echelle spectrograph operated by the European Southern Observatory (ESO). It is located at the 3.6 m telescope in La Silla, Chile and was established in 2003. It covers a wavelength range of 3800 to 6900 Å, with a spectral resolution of $R = 115\,000$, producing extracted and wavelength calibrated high-resolution spectra of stars. HARPS is designed to search for extrasolar planets and to estimate their radial velocity up to about 1 m/s (Mayor et al., 2003).

2.1.2 HARPS-N

Forty-seven stars of the analysed sample were observed with the High-Accuracy Radial velocity Planetary Searcher - North (HARPS-N), which is the northern equivalent to HARPS. It is a collaboration of a few observatories with the Astronomical Observatory of the Geneva University as the lead. HARPS-N is based at the 3.6 m Telescopio Nazionale Galileo (TNG) at the Roque de los Muchachos Observatory at La Palma, Canary Islands. Like its predecessor, HARPS-N is a fiber-fed, cross-dispersed echelle spectrograph, covering the same spectral

[1]Taken from ESO (with UVES during P105, P106) and at the TNG (with HARPS-N during A41, A42). Based on observations collected at the European Southern Observatory under ESO programmes 105.20P2.001, 106.21QS.001; at the Italian Telescopio Nazionale Galileo (TNG) under programmes AOT41_TAC25 and AOT42_TAC20. I acknowledge the use of the archival data from the following ESO programs: 093.C-0417, 094.C-0428, 095.C-0367, 096.C-0417, 097.C-0571, 098.C-0292, 099.C-0374, 0101.C-0407, 099.C-0491, 0100.C-0487, 098.C-0820, 099.C-0303, 0100.C-0474, 0101.C-0497, 097.C-0948, 098.C-0860, 0100.C-0808, 0101.C-0829, 074.C-0364, 60.A-9700(G), 198.C-0169, 096.C-0657, 0102.C- 0618, 0102.C-0319, 191.C-0873.

range from 3800 to 6900 Å. Also achieving an average spectral resolution of $R = 115\,000$, it is designed for the confirmation and characterisation of exoplanets, likewise focusing on the search of terrestrial planets in the habitable zone (Cosentino et al., 2012).

2.1.3 UVES

The remaining 24 stars of the analysed sample were observed with the Ultraviolet and Visual Echelle Spectrograph (UVES). It is installed at the Very Large Telescope (VLT) at the Paranal Observatory from ESO in Chile. It is attached to the second 8.2 m telescope (UT2 or "Kueyen"[2]). UVES is a cross-dispersion, echelle-spectrograph containing a red and a blue arm. The blue arm, which is needed for this work, covers a wavelength range of 3000 to 5000 Å, with a maximum spectral resolution of approximately $R = 80\,000$. UVES is not specifically designed for the search or characterisation of exoplanets like HARPS and HARPS-N, but rather for spectroscopic observations in general considering different object types (Dekker et al., 2000; D'Odorico et al., 2000).

2.1.4 The spectra

Some of the spectra were already co-added from multiple observations other consists of only one single observation. As a result, the signal-to-noise ratios (SNR) varies highly from star to star and some SNR values are not even known, since the value is not mentioned in the header of the datafile. This has implications on the precision of any resulting calculations. In Figure 2.1, two spectra with very different SNR values are shown. The upper panel has a SNR of approximately 1000, representing a very high value within the sample, whereas the bottom panel has a value of around 30, where the Ca II H and K absorption features are visible, but smaller lines disappear in the noise.

The important spectral feature for this work are the emission lines in the Ca II H and K lines (see Chapter 3.1). The strength of these emissions correlates with the chromospheric activity of its star (see Chapter 1.3.2). An example of a very strong emission feature and therefore quite active star can be seen in the upper panel of Figure 2.2. This star is GJ143, a K-type star observed with the HARPS instrument. In this case the emission line is even slightly exceeding the continuum nearby. In comparison to this quite active star, a spectrum with no emission can also be seen in the Figure 2.2, but in the bottom panel. It is the spectrum of star HD39091, a G-type star also observed with the HARPS instrument. A comparison between the two panels in Figure 2.2 clearly shows the difference between stars with high and low activity levels.

To measure the emission and thus the activity, a total of four passbands are needed as described in Chapter 1.4 and 3.1. Two of them are rectangular passbands on the left and right side of the Ca II H and K lines, which measure the local continuum flux. The other two are triangular shaped and lie directly on the calcium lines. An example of the four passbands can be seen in Figure 2.3, where they are shown in red.

[2] `https://www.eso.org/public/teles-instr/paranal-observatory/vlt/vlt-names/`

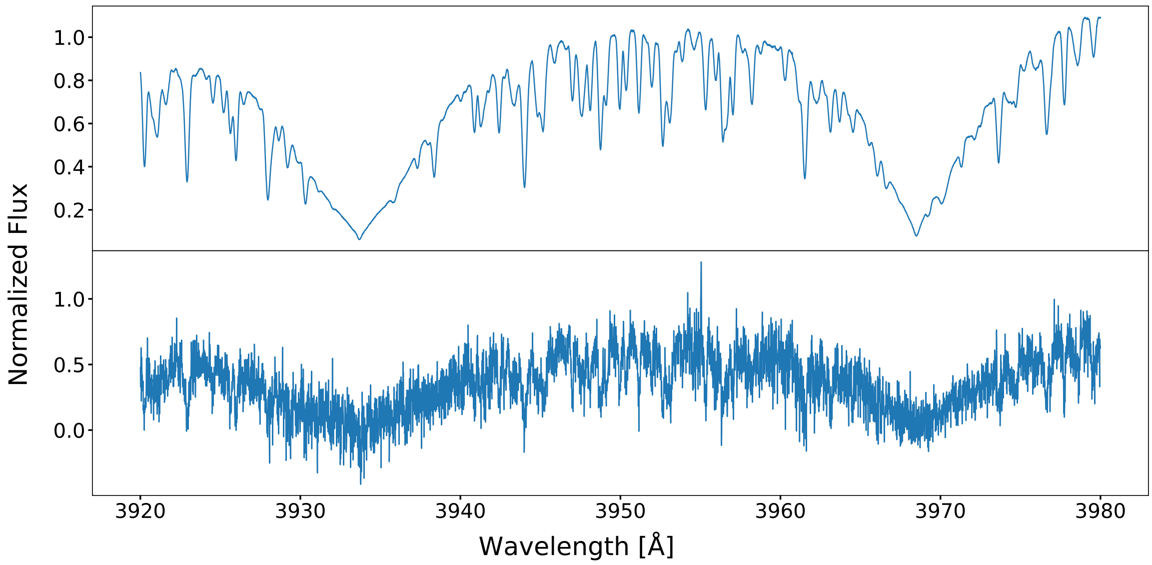

Figure 2.1: The upper panel shows a spectrum with a relatively high signal-to-noise ratio. Individual absorption lines are clearly visible and can be easily identified. The spectrum of the lower panel however, has a relatively low signal-to-noise ratio. The entire spectrum is strongly influenced by noise. Individual spectral lines are quite difficult to distinguish.

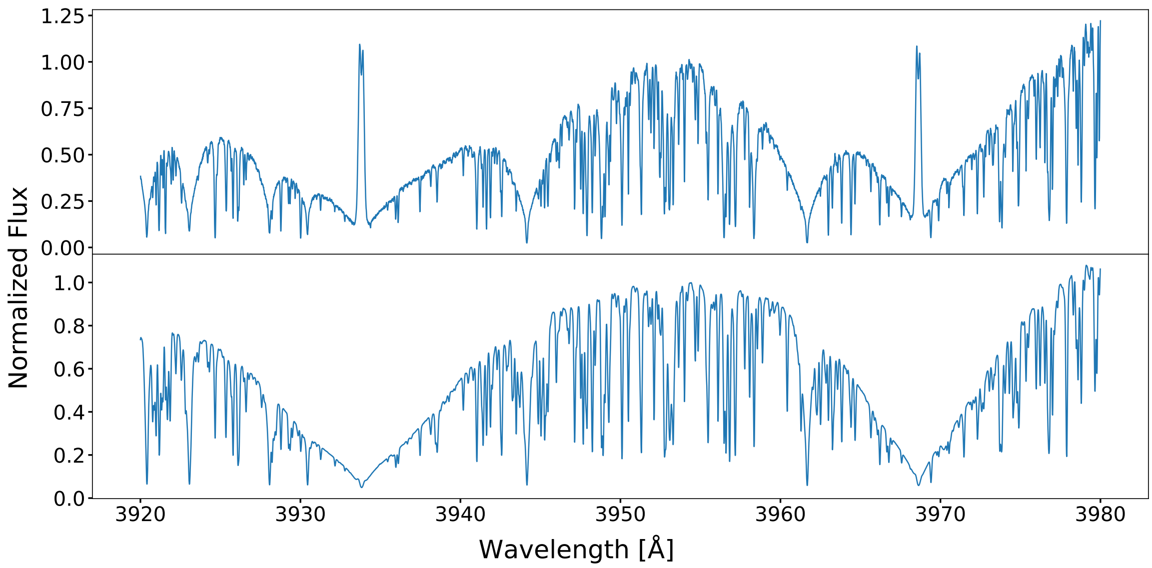

Figure 2.2: The upper panel shows the spectrum of GJ143, a very active K-type star. The emission features of the Ca II H and K lines can be seen very prominently, which indicates a strong chromospheric activity. For comparison, the lower panel shows a spectrum of the G-type star HD39091 with a very low activity and no observable emission of the Ca II H and K lines.

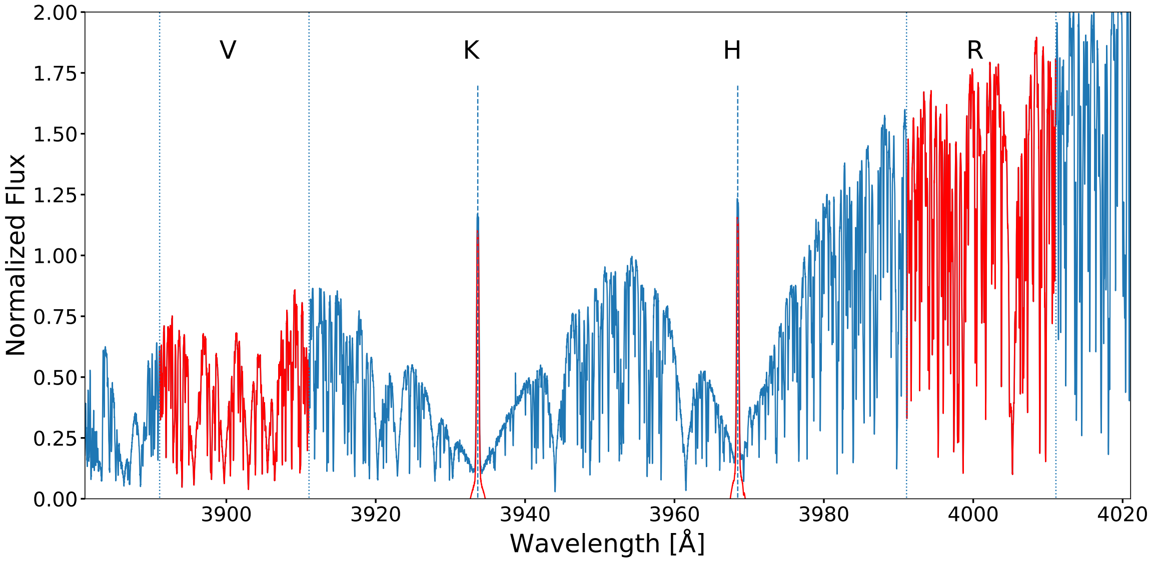

Figure 2.3: The red "V" and "R" areas are the rectangular continuum passbands, which are needed to measure the continuum flux in order to calculate the Mount-Wilson S-index (see Chapter 1.4 and 3). The emission of the Ca II H and K lines are measured using a triangular passband, also marked in red and labelled with the respective letter.

2.1.5 Luminosity classes

It is important to know if the analysed stars are main-sequence stars or if they belong to a different luminosity class. Magnetic fields of giants are generated differently, therefore they are not comparable to main-sequence stars (Basri, 2021). The luminosity class was determined using the surface gravity. As listed in Gray (2008), dwarf stars with spectral types between F to M cover a surface gravity ($\log g$) range of about 4.22 to 4.81. The sun lies right in the middle of this interval with a $\log g$ value of 4.438. In Figure 2.4 a comparison between the surface gravity $\log g$ and effective temperature is shown. It is clearly noticeable that most stars of the sample are dwarfs, with very few exceptions of (sub)giants with $\log g$ of 3 to 3.75.

2.1.6 Orbital parameters

Additionally, the current positions of the stars in the Milky Way and their galactic orbital parameters were analysed. In the upper panel of Figure 2.5 the positions of the stars compared to the Sun can be seen. The plot represents an edge-on view, where the x-axis represents the distance from the galactic center and the y-axis the distance from the galactic plane. The Sun is marked with a $\odot$ symbol. The colour of the dots represents the activity level $\log R'_{\mathrm{HK}}$, where yellow indicates a higher activity and purple a lower activity level. The more active stars tend to be closer to the sun. In the lower panel of Figure 2.5, a face-on view of the same data can be seen in a polar plot centered on the galactic center. Again, the more active stars are still closer to the Sun. This also confirms that all stars of the sample are indeed part of the solar neighbourhood.

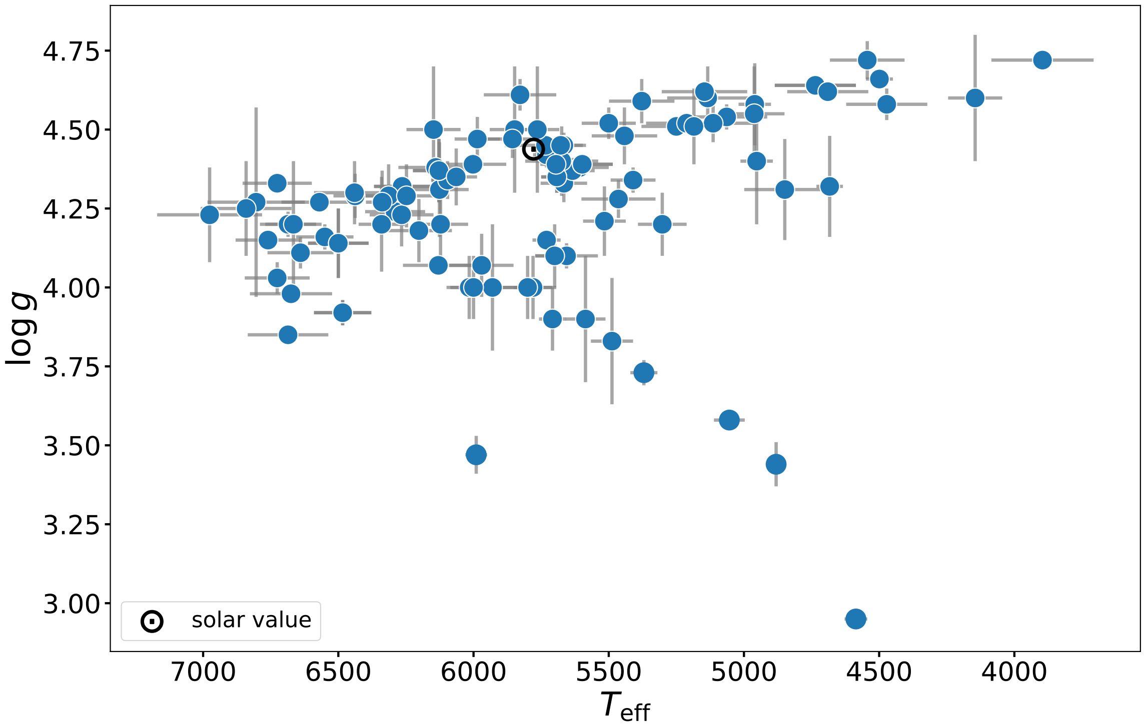

Figure 2.4: Effective temperature (x-axis) vs. surface gravity ($\log g$) (y-axis). The majority of the stars in the sample are on the main sequence, the few ones in the lower half of the plot are (sub)giants.

Furthermore, the galactic orbits of the stars were estimated from their current positions. The required proper motion data was taken from the Gaia DR3 (Gaia Collaboration et al., 2016a, 2023a; Babusiaux et al., 2023a) and the distances from Bailer-Jones et al. (2021). The computation itself was performed using the Python package "Gala"(Price-Whelan, 2017; Price-Whelan et al., 2020). For the gravitational potential of the Milky Way the default one from Bovy (2015), was used. The orbits were integrated for a period of 2 Gyr using a 1 Myr step size. For each star, a random sample of 128 variations was drawn from the initial set of parameters, assuming a normal distribution of each parameter with a standard deviation corresponding to its uncertainty (1σ interval). The final orbital parameters obtained from those samples were then again assumed to be normally distributed and a simple skewnormal fit was used to estimate the best-fit value and 1σ-uncertainty for each parameter. For a handful of the stars, determination of the orbits were not possible.

All stars have quite circular and pretty flat orbits. An example can be seen in Figure 2.6. The left panel shows the orbit face-on and the right panel shows an edge-on view. All of the stars can be considered disk stars, since their distances from the galactic plane don't even exceed 2.5 kpc (Jurić et al., 2008).

In the left panel of Figure 2.7, a histogram of the maximum vertical distances from the galactic plane can be seen. It clearly shows that most stars of the sample reach a maximum height of 0.5 kpc. The middle panel of Figure 2.7 shows two histograms in one: The blue

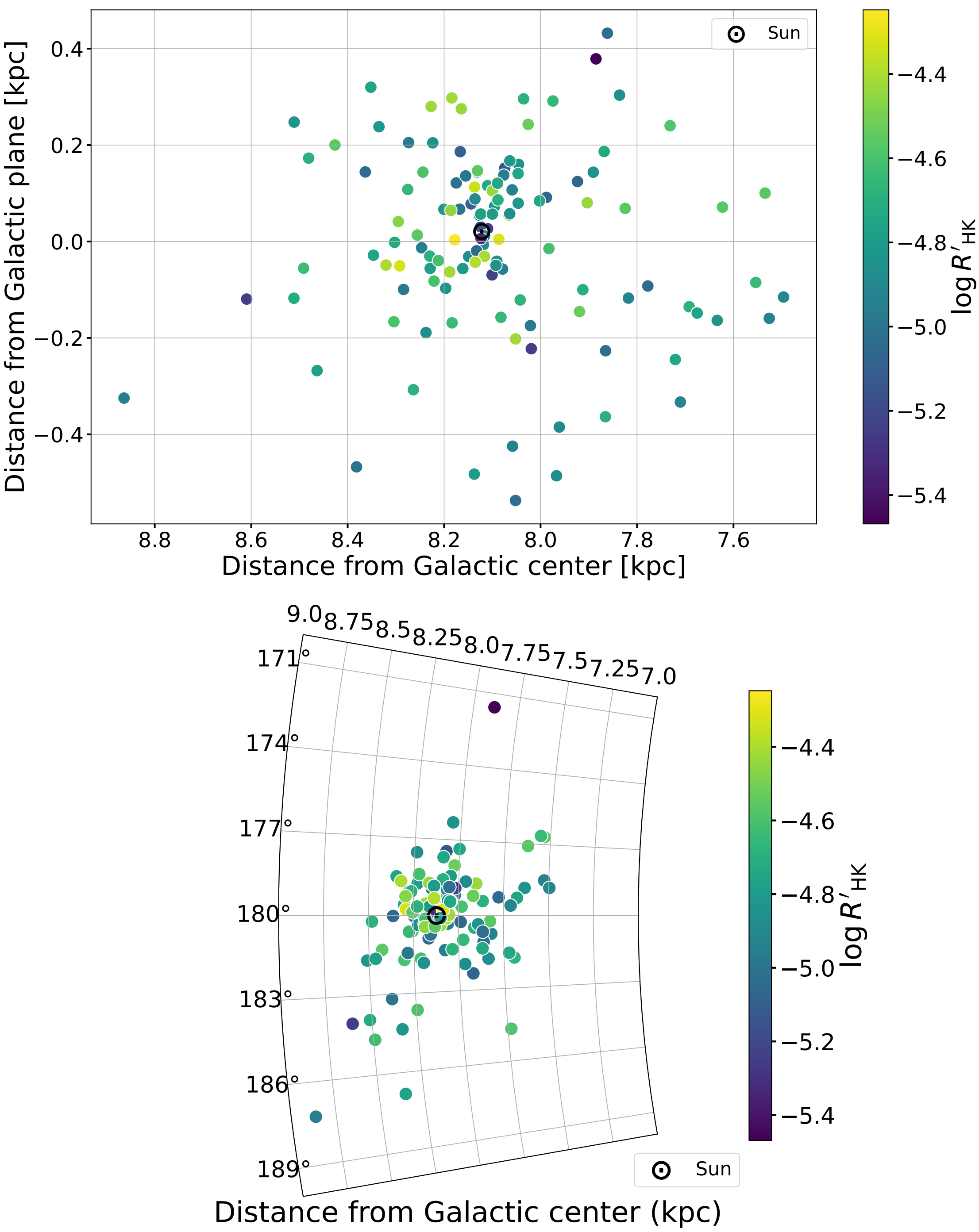

Figure 2.5: Both panels show the positions of the stars in the Milky Way with galactocentric coordinates. The upper panel gives an edge-on view and the lower panel a face-on view. All stars can be considered to be in the solar neighbourhood.

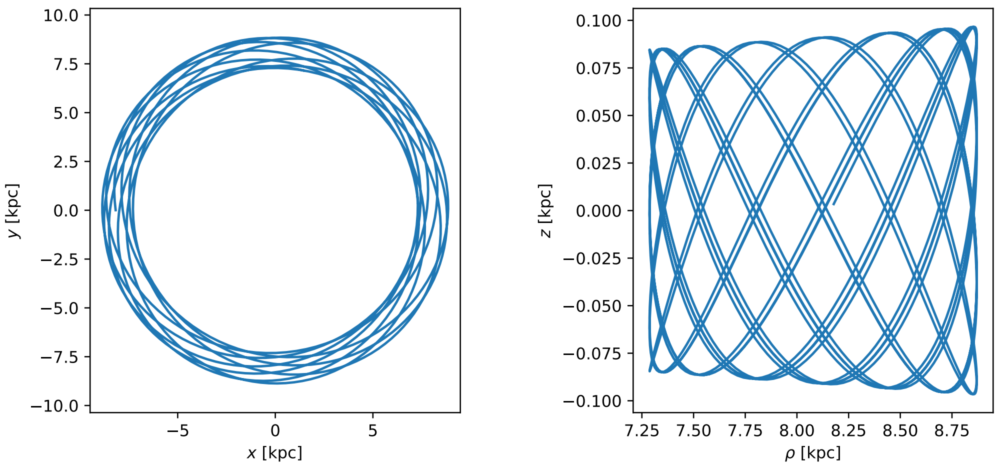

(a) Here a face-on view of the computed orbit can be seen.

(b) Here the edge-on view of the orbit in polar coordinates is visualised.

Figure 2.6: The figure shows an example of a computed orbit of one of the stars.

one describes the apocenter of the orbits and it can be seen that most of the stars do not go further out than 10 kpc and only very few stars reach a greater distance to the galactic center than 15 kpc. The orange histogram shows the pericenter of the orbits. Only a few stars are actually closer than 5 kpc to the center and the majority lies at a similar distance as the Sun. This means that together with the apocenter, the orbits are not only circular, but also have minimal radial variation. The right panel in Figure 2.7 shows another histogram, with the eccentricities of the orbits. Unsurprisingly, almost all stars have a low eccentricity of smaller than 0.2, corresponding to a very circular orbit. The exact values of all orbital parameters are listed in Table A.1.

2.1.7 Solar analogues

A second sample of stars was analysed separately. The sample consists of 18 solar-analogue stars, which are very similar in most parameters, for example their effective temperatures lie between the range of 5710 K and 6030 K (for more details see Beck et al. (2017)). The stars were observed using the Hermes spectrograph located at the 1.2 m Mercator telescope from the Spanish Observatorio del Roque de los Muchachos of the Instituto de Astrofísica de Canarias (Raskin et al., 2011). The data was taken from an observing program by Beck et al. (2016, 2017) and Salabert et al. (2016a,b), which was later continued for a larger sample, where these stars were continued to be observed to obtain a higher signal-to-noise. The data was provided via private communication.

2.2 Calibration

In order to calculate the Mount Wilson S-index (see Section 1.4 and Chapter3 for further information) with telescopes other than the Mount Wilson Observatory, a calibration should be applied. To calibrate the different instruments I used standard stars that are common

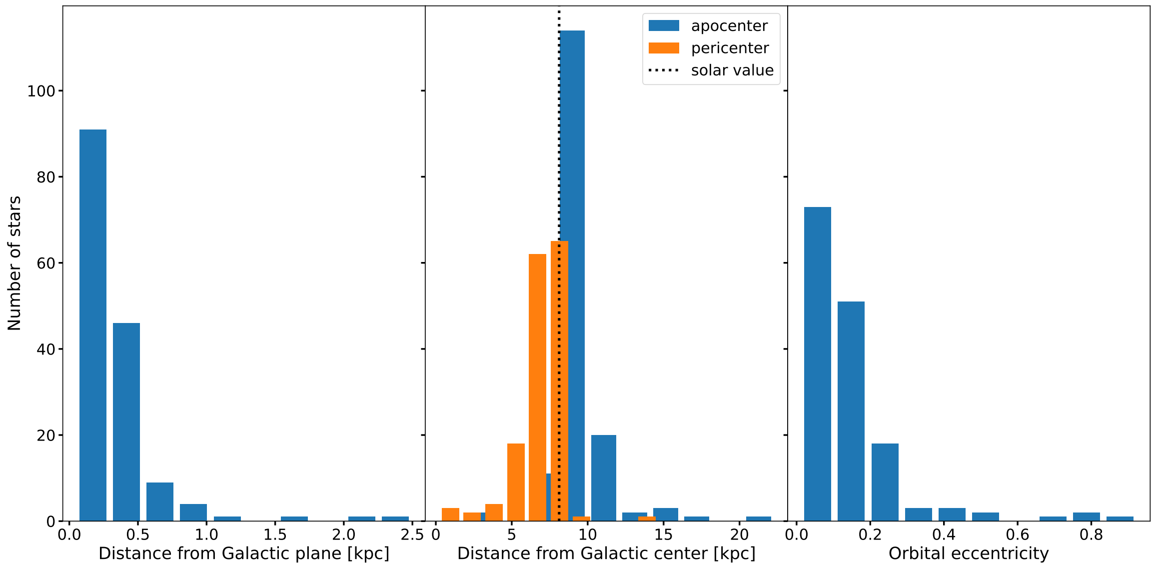

Figure 2.7: The left panel shows a histogram with the maximum vertical distances from the galactic plane. All stars are part of the galactic disc. The middle panel shows two histograms, the blue one indicates the apocenter of the orbits and the orange one the pericenter. The right panel shows a histogram of the orbital eccentricities, which clearly shows that most stars have a very circular orbit.

between the different instruments. Table 2.1 shows the standard stars used for the calibration.

For the HARPS[3] and HARPS-N[4] instruments, 7 stars each were used for the calibration. They were downloaded directly from the respective archives. However, UVES did not have enough stars with publicly available observation data to create a reliable calibration. This is probably also due to the fact that the VLT, where UVES is based, is located in the southern hemisphere, unlike the Mount-Wilson Observatory. An overlap of stars observed with both telescopes is therefore rather small, only two stars were found after an extensive matching of the public data archives, which is too little for a calibration. To solve this problem, the HARPS calibration was used to calculate the Mount-Wilson-values for 6 individual stars, which were observed with both HARPS and UVES. The values obtained with the HARPS calibration were then used to calibrate UVES. The spectra of these stars were downloaded from the HARPS and UVES archives[5]. These 6 stars and their spectral types can also be found in Table 2.1. The results of the calibration and the calculated values for each individual star are discussed in Chapter 4.

For the data of the solar analogues (see Section 2.1.7) no calibration was needed and therefore no S_{MWO} values were determined, since these stars were only compared within their sample. This is only possible because they were all observed with the same instrument on the same

[3]HARPS archive: http://archive.eso.org/eso/eso_archive_main.html
[4]HARPS-N archive: http://archives.ia2.inaf.it/tng/
[5]UVES archive: http://archive.eso.org/eso/eso_archive_main.html

Table 2.1: The stars and their spectral type, that were used for the calibrations, separated by instrument.

HARPS-N	Spectral type	HARPS	Spectral type	UVES	Spectral type
HD10700	G8V[1]	HD10700	G8V[1]	HD39194	K0V[4]
HD16160	K3V[1]	HD16160	K3V[1]	HD46375	G9V[6]
HD115404	K2V[2]	HD23249	K0IV[1]	HD73256	G8IV-V[4]
HD120136	F7IV-V[3]	HD152391	G8.5V[4]	HD75289	F9V[4]
HD14100	G0V[1]	HD160346	K3V[1]	HD140538	G2.5V[1]
HD182572	G7IV[1]	HD216385	F6V[5]	HD193901	F7V[7]
HD217014	G2IV[1]	HD219834	G8.5IV[4]		

References for spectral types:
1. Keenan and McNeil (1989)
2. White et al. (2007)
3. Gray et al. (2001)
4. Gray et al. (2006)
5. Gray et al. (2003)
6. Grieves et al. (2018)
7. Houk and Smith-Moore (1988)

telescope. Without a calibration this sample cannot be compared to a different sample of stars. Since their parameters are very similar, a temperature dependence does not lead to a misinterpretation of the compared values.

Chapter 3

Methods

In this chapter, the method used to determine the chromospheric activity of the stars is explained in more detail.

3.1 The Mount Wilson S-index

The S_{MWO}, as already mentioned in Chapter 1, is a spectroscopic parameter derived from the Calcium H and K lines, which are located at wavelengths of 3968.47 Å and 3933.664 Å respectively (Baliunas et al., 1995). The fluxes of these lines are put into relation with two nearby continuum bands, one at the red side and one at the blue side of the spectrum. This leads to the following formula, described by Vaughan et al. (1978) and later by Duncan et al. (1991):

$$S = \alpha \cdot \frac{N_{\text{H}} + N_{\text{K}}}{N_{\text{R}} + N_{\text{V}}} \tag{3.1}$$

N_{H}, N_{K}, N_{R} and N_{V} are the respective number of counts in the H- and K-bands and the continuum bands in the redder and more violet region of the spectrum. The corresponding areas of those continuum bands are each 20 Å wide and cover wavelengths from 3991.07 to 4011.07 Å on the red side and from 3891.07 to 3911.07 Å on the violet side of the spectrum (Duncan et al., 1991). α is a proportionality constant, which was originally measured individually for every night from the standard stars used by (Vaughan et al., 1978). Later, a fixed value of $\alpha = 2.4$ was determined from many observations. Its purpose was to get a consistent conversion from the first to the second detector used on the Mount Wilson Observatory (Duncan et al., 1991). O. C. Wilson used a photomultiplier for his original observations, which had an 8-times longer exposure time in the H and K bands compared to the nearby continuum bands. Since modern observations are based on spectrographs which have an equal exposure time throughout the whole spectrum, this factor 8 now needs to be taken into account separately, which changes the formula 3.1 to the following (Duncan et al., 1991; Astudillo-Defru et al., 2017):

$$S = 8 \cdot \alpha \cdot \frac{N_{\mathrm{H}} + N_{\mathrm{K}}}{N_{\mathrm{R}} + N_{\mathrm{V}}} \tag{3.2}$$

It is important to note, that the equations 3.1 or 3.2 do not provide the wanted Mount-Wilson S-index, but just an S-index. If the observation was not taken with the Mount Wilson observatory, but with a different telescope, the values need to be calibrated to get a comparable S_{MWO} value. This calibration is a simple linear fit, as seen for example in Lovis et al. (2011). As already mentioned in Chapter 2, observations from three different instruments on different telescopes are used in this work, therefore an individual calibration is necessary for each instrument. The calibrations can be found in Chapter 4.

The S_{MWO} however, has one great disadvantage when it comes to comparing different types of stars. Since the calculation uses two continuum bands of the spectra, the values depend on the spectral types of the stars. This is because the fluxes in the continuum bands are not the same for different spectral classes. For later-type stars, the maximum flux shifts more towards the longer wavelengths, while the flux in the R and V bands decreases correspondingly. This leads to a smaller S_{MWO} value for a typical F or G star compared to a typical K star. Furthermore, a K-type star might in general be more active than a younger-type star, which makes a comparison of different spectral types even more difficult (Marvin et al., 2023; Boro Saikia et al., 2018).

3.2 Colour-independence

To account for the colour-dependence, a new quantity, R'_{HK}, was introduced by Middelkoop (1982a) and Noyes et al. (1984). Instead of using the number of counts in the H- and K-bands, Middelkoop (1982a) uses the total fluxes, by neglecting wavelength dependent factors within the conversion, thus writing:

$$\mathscr{F}_{\mathrm{H}} + \mathscr{F}_{\mathrm{K}} = \frac{S(\mathscr{F}_{\mathrm{R}} + \mathscr{F}_{\mathrm{V}})}{\alpha} \tag{3.3}$$

Here, $\mathscr{F}_{\mathrm{H}}$, $\mathscr{F}_{\mathrm{K}}$, $\mathscr{F}_{\mathrm{R}}$ and $\mathscr{F}_{\mathrm{V}}$ are the total fluxes per unit area of the stellar surface, of the continuum band and the H and K bands, respectively. For the total fluxes in the continuum bands the following applies:

$$\mathscr{F}_{\mathrm{R}} + \mathscr{F}_{\mathrm{V}} = \frac{\beta(N_{\mathrm{R}} + N_{\mathrm{V}})F_{\mathrm{BOL}}}{f_{\mathrm{BOL}}} \tag{3.4}$$

Since no instrumental variation and a constant extinction is assumed, β is an unspecified constant (Rutten, 1984). F_{BOL} and f_{BOL} indicate the absolute and apparent bolometric flux respectively. They are also known as:

$$F_{\mathrm{BOL}} = \sigma T_{\mathrm{eff}}^4 \tag{3.5}$$

$$f_{\mathrm{BOL}} = \gamma 10^{-0.4(m_{\mathrm{V}}+BC)} \tag{3.6}$$

Where equation 3.5 resembles the Stefan-Boltzmann-law (Weigert, 2009) and f_{BOL} was taken from Middelkoop (1982b). The constant σ is the Stefan-Boltzmann-constant (Weigert, 2009) and γ is the irradiance corresponding to the zero point of the apparent bolometric magnitude, given by Mamajek et al. (2015) as $2.518 \cdot 10^{-8}\,\mathrm{W/m^2}$. The value m_{V} is the apparent magnitude in the visual and BC is the bolometric correction. T_{eff} labels the effective temperature of the star. Inserting equation 3.5 and 3.6 into equation 3.4 results in:

$$\mathscr{F}_{\mathrm{R}} + \mathscr{F}_{\mathrm{V}} = \frac{\beta(N_{\mathrm{R}} + N_{\mathrm{V}})\sigma T_{\mathrm{eff}}^4}{\gamma 10^{-0.4(m_{\mathrm{V}}+BC)}} \tag{3.7}$$

By now combining equation 3.7 with equation 3.3 it leads to:

$$\mathscr{F}_{\mathrm{H}} + \mathscr{F}_{\mathrm{K}} = S\frac{\beta(N_{\mathrm{R}} + N_{\mathrm{V}})\sigma T_{\mathrm{eff}}^4}{\gamma 10^{-0.4(m_{\mathrm{V}}+BC}}/\alpha \tag{3.8}$$

Defining a conversion factor C_{cf} as:

$$C_{\mathrm{cf}} = (N_{\mathrm{R}} + N_{\mathrm{V}})10^{0.4(m_{\mathrm{V}}+BC)} \tag{3.9}$$

and rearranging equation 3.8, the final equation by Middelkoop (1982a) reads as follows:

$$F_{\mathrm{HK}} = F_{\mathrm{H}} + F_{\mathrm{K}} = \frac{(\mathscr{F}_{\mathrm{H}} + \mathscr{F}_{\mathrm{K}})\alpha\gamma}{\beta\sigma} = S\frac{(N_{\mathrm{R}} + N_{\mathrm{V}})}{10^{-0.4(m_{\mathrm{V}}+BC)}}T_{\mathrm{eff}}^4 = SC_{\mathrm{cf}}T_{\mathrm{eff}}^4 10^{-14} \tag{3.10}$$

The factor 10^{-14} does not appear in the publication by Middelkoop (1982a), but he introduced it in his PhD thesis as "arbitrarily chosen to provide nice numbers"[1] Middelkoop (1982b).

The empirical colour-dependent conversion factor C_{cf} was determined by Middelkoop (1982a) using the following fit:

$$\log C_{\mathrm{cf}} = 1.13(B-V)^3 - 3.91(B-V)^2 + 2.84(B-V) - 0.47 \tag{3.11}$$

which is suitable for stars in the range of $0.45 \leq (B-V) \leq 1.5$.

(Middelkoop, 1982a) and Noyes et al. (1984) later introduced a value called R_{HK}. It is a physical quantity and it describes the emission of the H and K lines (Hartmann et al., 1984). It is defined as:

[1] This was directly quoted from Middelkoop (1982b), who does not provide any further explanation why this number was chosen.

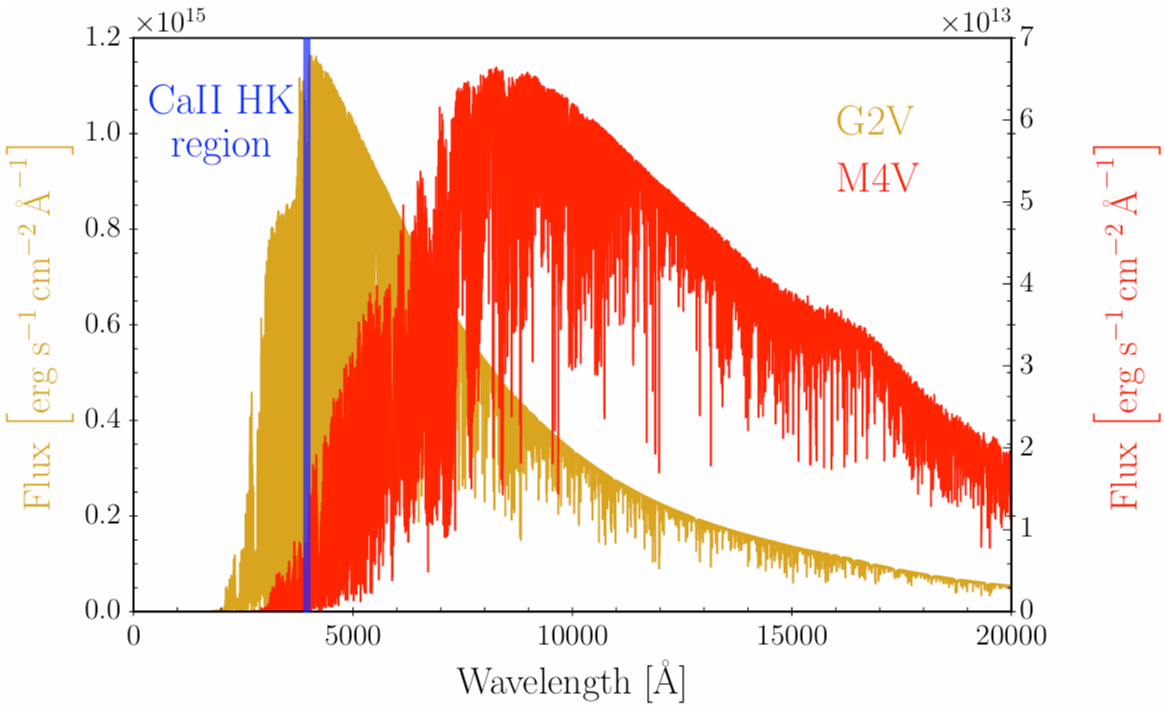

Figure 3.1: Peaks of the blackbody radiation of a G type star and a M type star differ in wavelength. This is especially crucial for the S-index calibration of M-stars since their stellar flux is very weak in the region around the Ca II H and K lines. Therefore the S-index is not suitable when it comes to a comparison between different spectral types of stars. The image was taken from Marvin et al. (2023) under CC By 4.0.

$$R_{\mathrm{HK}} = \frac{F_{\mathrm{HK}}}{\sigma T_{\mathrm{eff}}^4} \tag{3.12}$$

Where F_{HK} is the total flux of the H and K bands per cm^2. Since only the counts in the bands are measured, Noyes et al. (1984) used equation 3.10, a conversion factor K and σ as the Stefan-Boltzmann-constant in CGS units, to end up with the equation:

$$R_{\mathrm{HK}} = 1.34 \cdot 10^{-4} S C_{\mathrm{cf}} \tag{3.13}$$

The conversion factor C_{cf} only depends on the colour index $(B - V)$ of each star. However, the colour index is affected by extinction (reddening) and also not suitable for cooler stars, especially M-stars, which lie outside of the valid $(B - V)$ range. This is because the peak of their blackbody radiation is shifted too far to the red side of their spectrum, so that there is only little to no flux in the B-band. This can be seen in Figure 3.1 (Marvin et al., 2023). However, the colour of a star is directly related to its effective temperature (T_{eff}) and the estimation of T_{eff} is nowadays based on high-resolution spectroscopy, which makes it independent of extinction (Afşar et al., 2023).

Marvin et al. (2023) developed a method, which only depends on the effective temperature of a star instead of its colour index. Using equation 3.3 and combining it with equation 3.10, including the conversion factor K to convert it in absolute units and solving for C_{cf}, results in:

$$C_{\mathrm{cf}} = 4.8676 \cdot 10^6 \frac{\mathscr{F}_{\mathrm{RV}}}{T_{\mathrm{eff}}^4} \tag{3.14}$$

To eliminate $\mathscr{F}_{\mathrm{RV}}$, Marvin et al. (2023) made a fit, which includes different values of metallicity and surface gravity. This results in:

$$\begin{aligned}\log C_{\mathrm{cf}} = &-2.9679 + 2.6864 \cdot 10^{-2} T_{\mathrm{eff}} - 1.0268 \cdot 10^{-5} T_{\mathrm{eff}}^2 + 1.9866 \cdot 10^{-9} T_{\mathrm{eff}}^3 \\ &- 1.9017 \cdot 10^{-13} T_{\mathrm{eff}}^4 + 7.1548 \cdot 10^{-18} T_{\mathrm{eff}}^5\end{aligned} \tag{3.15}$$

Now R_{HK} can be calculated using the equations 3.13 and 3.15.

3.3 Photospheric Contribution

By measuring the S_{MWO} and therefore the R_{HK} only the chromospheric emission is wanted, but the measurement will always contain some photospheric flux as well. This varies for different spectral types. In order to only measure the chromospheric activity, the photospheric contribution needs to be subtracted (Noyes et al., 1984). Originally, Noyes et al. (1984) determined empirically a correction of the photospheric contribution depending on the colour index $(B-V)$:

$$\log R_{phot} = -4.898 + 1.918(B-V)^2 - 2.893(B-V)^3 \tag{3.16}$$

Equation 3.16 is suitable for $0.44 \leq (B-V) \leq 0.82$. Like in Section 3.2, Marvin et al. (2023) used stellar atmosphere models to create another fit, which represents the photospheric flux:

$$\begin{aligned}\log R_{\mathrm{phot,\,M}} = &-3.755 + 3.2131 \cdot 10^{-2} T_{\mathrm{eff}} - 1.3177 \cdot 10^{-5} T_{\mathrm{eff}}^2 + 2.7133 \cdot 10^{-9} T_{\mathrm{eff}}^3 \\ &- 2.7466 \cdot 10^{-13} T_{\mathrm{eff}}^4 + 1.0887 \cdot 10^{-17} T_{\mathrm{eff}}^5\end{aligned} \tag{3.17}$$

This method depends on the effective temperature instead of the colour index and is suitable for a bigger range of spectral types, including M-type stars. Unfortunately, this calibration gets higher values than the original formula used by Noyes et al. (1984). However, the calibration by Marvin et al. (2023) will be used here, since it again depends on T_{eff} instead of the colour index, so a homogeneous system can be maintained. To compensate the offset, Marvin et al. (2023) introduced the following correction:

$$\log R_{\mathrm{phot}} = \log R_{\mathrm{phot,\,M}} - 0.4612 \tag{3.18}$$

Finally, subtracting the non-logarithmic form of equation 3.18 from equation 3.13 leads to the desired value R'_{HK}, describing the chromospheric activity:

$$R'_{\mathrm{HK}} = R_{\mathrm{HK}} - R_{\mathrm{phot}} \tag{3.19}$$

3.4 Hα-index

Another index for the activity of a star is the $H\alpha$-index. The method is very similar to the Mount-Wilson S-index. It is also the relation of the flux in a passband centered at the Hα line to two passbandes of the continuum on the left and right side of that line. The Hα line lies at 6562.08 Å (Balmer, 1885). The problem here is that there is no standardised form, so that the passbandes over the Hα line and the two continuum bands have different widths depending on the study (e.g. Pasquini and Pallavicini (1991); Cincunegui et al. (2007); Gomes da Silva et al. (2011a); Marsden et al. (2014). For this work the definitions from Marsden et al. (2014) were used:

$$H\alpha = \frac{F_{H\alpha}}{F_{VH\alpha} + F_{RH\alpha}} \tag{3.20}$$

Here, $F_{H\alpha}$, is the flux in the passband centered at the Hα line. The bandpass is rectangular and 3.6 Å wide. The continuum bands on the left an right side of Hα, $F_{VH\alpha}$ and $F_{RH\alpha}$ respectively, are rectangular as well and 2.2 Å wide each. They are centered at 6558.85 Å and 6567.30 Å.

Chapter 4

Results

For this work I characterised the chromospheric activity of 127 F-G-K-M stars and 18 solar analogues. The main parameters, that I determined were the Mount Wilson S-index and the $\log R'_{\mathrm{HK}}$ value.

4.1 S-index calibration

As mentioned in Chapter 2 the S_{MWO} is calibrated individually for each instrument. This was done by simply comparing the uncalibrated calculated values to the values obtained by the original Mount-Wilson survey from Baliunas et al. (1995) using a linear fit. The outcome of this can be seen in Figure 4.1. The top left panel is a visualisation for the calibration of the HARPS-N instrument. The x-axis indicates the calculated values of the S-index with HARPS-N before calibration. The y-axis denotes the Mount Wilson S-index (S_{MWO}) from the literature. The dashed grey line is a line of equality, every blue dot marks a star and the orange line is the resulting linear fit. The fitted linear equation is shown in equation 4.1. With this equation, all stars observed with HARPS-N can be calibrated to get the desired S_{MWO} value. A more detailed explanation of the stars that were used together with a list of their individual spectral types can be found in Chapter 2 and Table 2.1. The top right and the bottom left panel in Figure 4.1 show the same concept, but for different instruments. The top right one displays the linear fit for HARPS and the bottom left one for UVES. A more detailed explanation of the UVES calibration can be found in Chapter 2. The fitted calibration equations are 4.2 and 4.3 respectively. The calculated values for each star as well as their literature S_{MWO} values are listed in Table A.2, separated by instrument. Additionally in this table the associated uncertainties (S_{err}), the difference between the S_{MWO} and calibrated values (ΔS), as well as the number of observation (N_{obs}) can be found. For most stars, (ΔS) is rather small, which indicates an appropriate calibration. For the calculation of (S_{err}) the Gaussian error propagation was applied. The S^{*}_{MWO} from equation 4.3 denotes, that for this calibration the values were not compared directly to the literature, but to calculated values using the HARPS calibration.

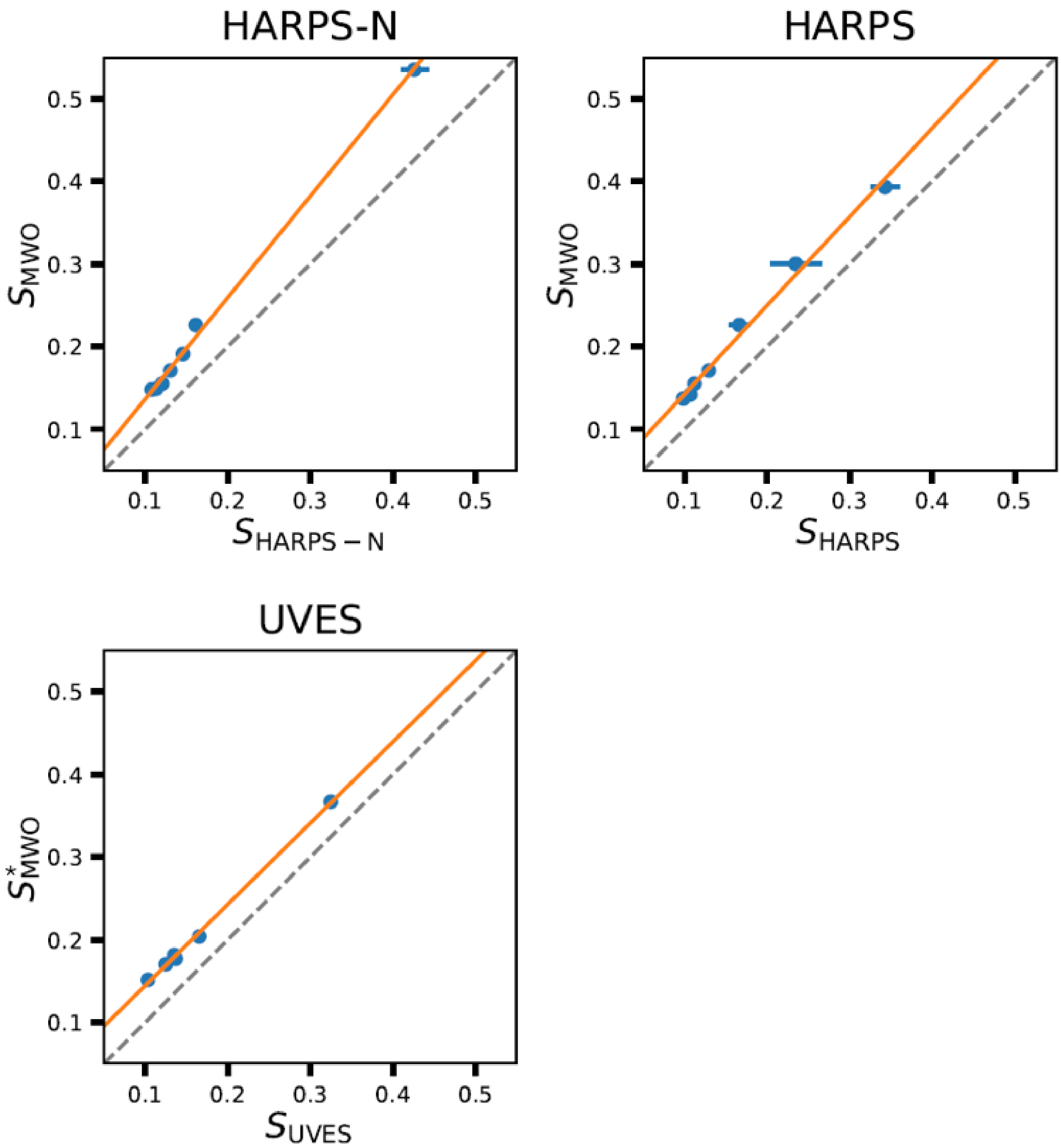

Figure 4.1: The upper left panel shows the visualisation of the calibration for the HARPS-N instrument. The equation for the orange linear fit can be found at equation 4.1. The x-axis describes the values calculated from the spectra in this work and the y-axis marks the original Mount Wilson S-index values from Baliunas et al. (1995). The upper right and the lower left show the same, but for HARPS and UVES respectively.

$$\begin{aligned} \text{HARPS-N:} \quad S_{\mathrm{MWO}} &= 0.0139 + 1.228 \cdot S_{\mathrm{HARPS-N}} \quad (4.1) \\ \text{HARPS:} \quad S_{\mathrm{MWO}} &= 0.0347 + 1.067 \cdot S_{\mathrm{HARPS}} \quad (4.2) \\ \text{UVES:} \quad S^{*}_{MWO} &= 0.0455 + 0.983 \cdot S_{\mathrm{UVES}} \quad (4.3) \end{aligned}$$

With the calibrations now available for each individual instrument, the S_{MWO} values for each star of the analysed sample can be determined. The resulting values can be found in Table A.4.

4.2 Temperature dependence of S_{MWO}

Looking at a comparison of the effective temperatures of the stars with their S_{MWO} values, the importance of taking the colour dependence into account becomes clear once again (see Chapter 3 for further information). This can be seen in Figure 4.2. Here it is well visible, that the S_{MWO} values follow a certain trend. Hotter stars, at approximately 7000 K to roughly 6000 K tend to have quite small values, which would indicate a lower activity level. However, cooler stars especially of late K- and M-type, show much higher values, which would indicate a quite high level of activity. Moreover, the S_{MWO} values of stars with a lower temperature are more spread out in a certain interval than those of the stars with higher temperatures. However, it should be noted that the peak of S_{MWO} is still within the spectral class K and decreases again for M-type stars. This is also consistent with the literature for example in Isaacson and Fischer (2010); Mittag et al. (2013); Loaiza-Tacuri et al. (2024), who compared S_{MWO} values to their respective colour-indices. As stated in Isaacson and Fischer (2010) the increase of S_{MWO} towards cooler stars is expected since the measured flux in the continuum bands decreases for redder stars. The temperature dependence makes it therefore rather unsuitable for comparing stars of different spectral types.

4.3 Solar-analogues

The S-index was analysed for 18 solar analogues as well. Their effective temperatures lie all in a range of 5710 to 6030 K and they all have around one solar mass. More information about this sample of stars can be found in Section 2.1.7. The S-index of these stars is not their Mount-Wilson S-index, since there was no calibration performed. However, as the stars were all observed with the same telescope, they can still be compared with each other, but a comparison with a different sample of stars is not possible. As the stars have very similar stellar parameters and differ only slightly in their effective temperatures, the temperature dependence of the S-index is not a problem when comparing the stars. The S-index, hereafter S_{SA}, was calculated with equation 3.2 and the results for each star can be found in Table A.3. In Figure 4.3 a comparison between S_{SA} and the effective temperatures can be seen. The values for the effective temperatures were taken from Salabert et al. (2016a). Their individual S_{SA} values lie within the interval of 0.111 to 0.227, which means the S_{SA} value of the most active star in this sample is approximately twice the S_{SA} value of the least active star. In order to interpret the size of this S_{SA} interval correctly, it is important to know how much the S-index of a star can change due to the stars variability. For this, Judge

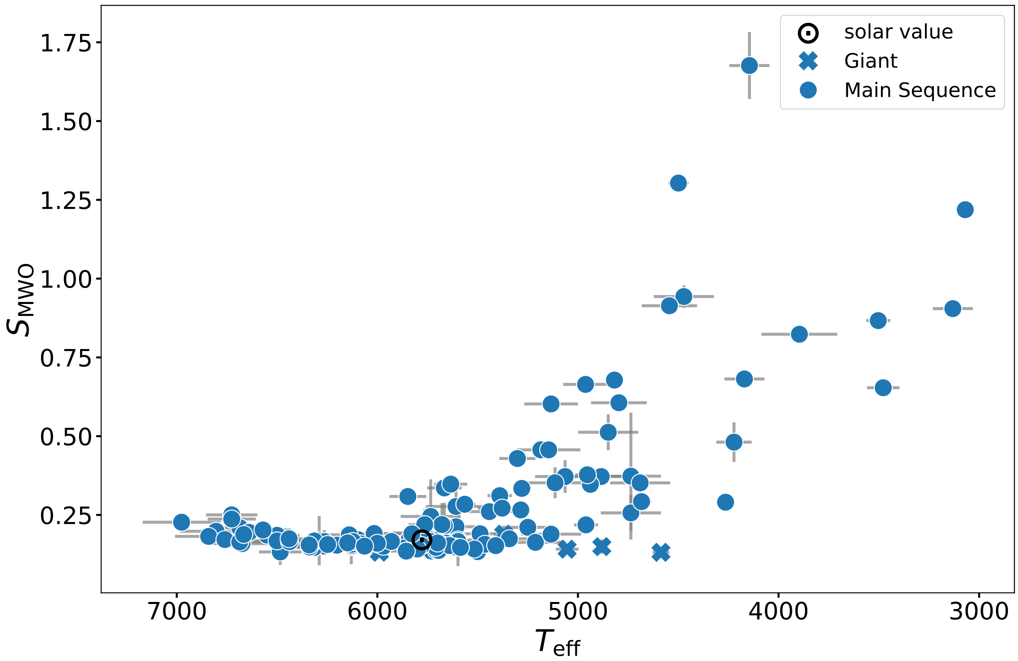

Figure 4.2: Effective temperature (x-axis) vs. S_{MWO} (y-axis). The solar S_{MWO} value of 0.171 was taken from Noyes et al. (1984) and is marked with a ⊙ symbol. Giants are marked with a cross. Here a correlation of the temperature and S_{MWO} can be seen. Hotter stars between 7000 K to roughly 6000 K only show small S_{MWO} values, whereas stars of 5000 K or below have a significant spread in S_{MWO} values. In general the cooler the star, the higher their S_{MWO}.

et al. (2017), made a time-series of the S-index over eight years for five individual G-stars. The biggest S-index change of one of their stars was approximately 0.025, which is way smaller than the covered range of the solar analogues. Especially for the sun, Egeland et al. (2017), determined S-index values of the solar cycles 15 to 24 and found an average change of approximately 0.0145. This change is indicated in Figure 4.3 as a blue shaded region. This means that the analysed solar analogues cover a much broader range regarding their S_{SA} values than the general variability would cause. It can therefore be re-confirmed, that stars with very similar stellar parameter do not necessarily need to show similar activity levels.

4.4 $\log R'_{\mathrm{HK}}$ values

In order to compensate for the disadvantage of the temperature or colour dependence of the Mount-Wilson S-index, another value called R'_{HK} was introduced by Noyes et al. (1984), the details of which are described in Chapter 3. Based on the S_{MWO} the $\log R'_{\mathrm{HK}}$ values were determined and the results are listed in Table A.4.

In Figure 4.4 a histogram of all $\log R'_{\mathrm{HK}}$ values obtained from the sample used in this work is shown. It depicts a Gaussian distribution between an activity level of about -5.4 and

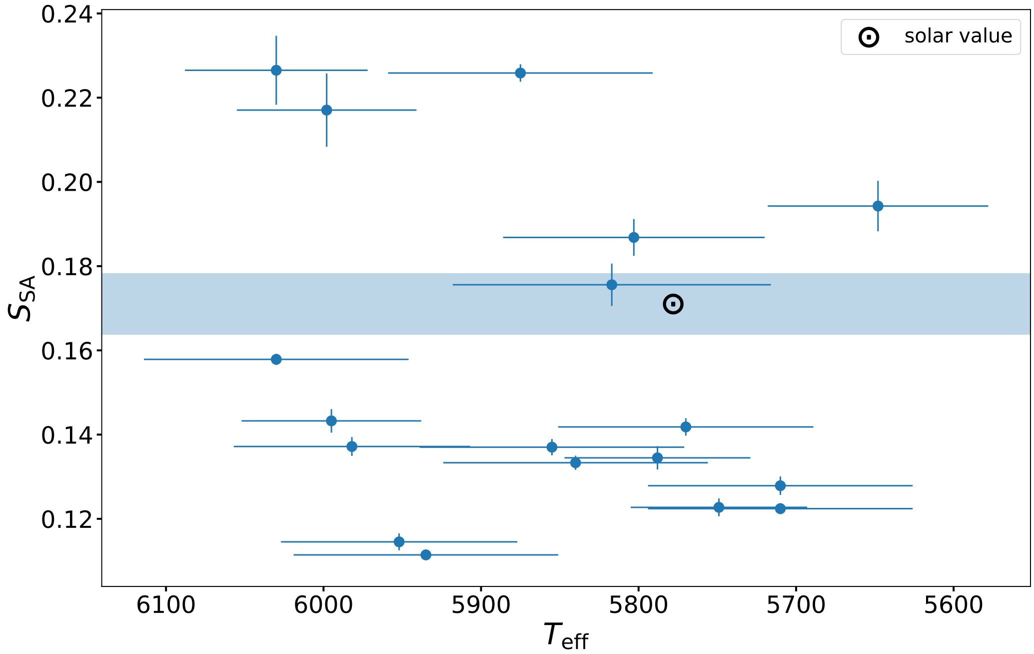

Figure 4.3: Effective temperature (x-axis) vs. S_{SA} values. The $S_{\rm MWO}$ value of the sun is indicated by a ⊙ symbol. The blue shaded region indicated the average change of the suns S-index over a solar cycle. The solar values were taken from Egeland et al. (2017).

-4.2. For comparison, the Sun has a $\log R'_{\rm HK}$ value of -4.937 (Noyes et al., 1984), which is very close to the histogram's peak. Therefore, it may be stated that the analysed sample has on average a solar-like chromospheric activity, although the spread is considerable. The distribution of the determined $\log R'_{\rm HK}$ values in this specific sample of stars is very well comparable to the main-sequence stars of Figure 14 by Gomes da Silva et al. (2021). Since the analysed sample of this work is significantly smaller, it is no surprise that the covered range is also a bit shorter. Nevertheless, the general distribution is very much comparable, with the peak being nearly on the same value.

In Figure 4.5 the distribution of the $\log R'_{\rm HK}$ values in the sample is now separated by spectral type. The left panel shows a histogram for F-type stars with a Gaussian distribution. The black dotted line indicates the solar value. The majority of the stars show a higher $\log R'_{\rm HK}$ than the sun. The distribution is similar to Figure 23 in Mittag et al. (2013). The middle panel shows the histogram for G-type stars. It is a bimodal distribution with the sun lying within the left peak (indicated by the black dotted line). This can be compared to Figure 17 in Gomes da Silva et al. (2021). They also find a bimodal distribution for G-dwarfs with the same peak values as this work. One possible explanation for the lack of stars between the two peaks could be the "Vaughan-Preston-gap", which describes a lack of intermediate active stars (Vaughan and Preston, 1980). It is not clear what causes this gap or if it is even a physical phenomena or just a statistical effect due to the small sample size (Noyes et al., 1984; Boro Saikia et al., 2018). Popular explanations are for example dynamo mechanisms or a difference in rotation (Durney et al., 1981; Böhm-Vitense, 2007). In the right panel of

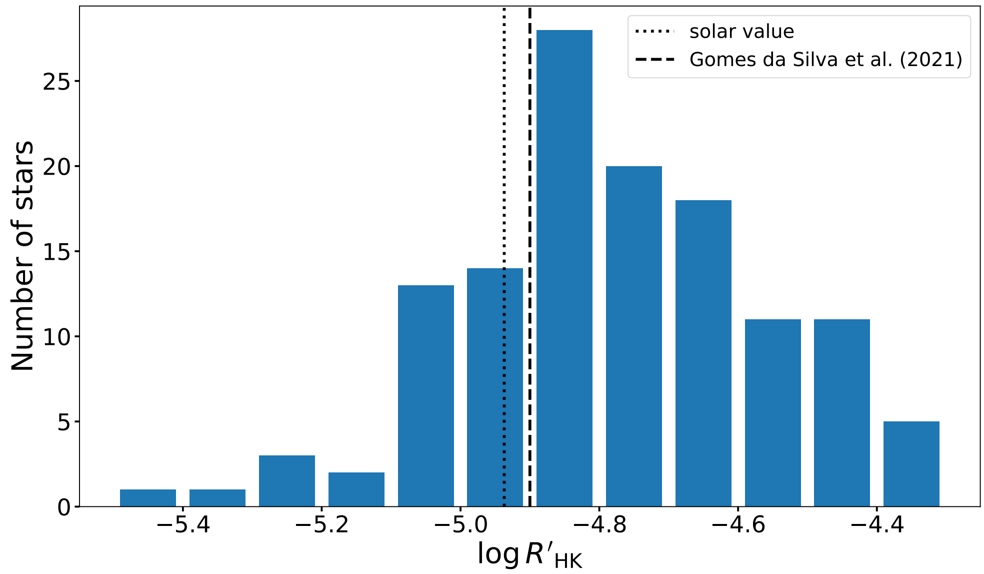

Figure 4.4: Distribution of the $\log R'_{\mathrm{HK}}$ values of the sample stars. The black dotted line indicates the solar value of $\log R'_{\mathrm{HK}}$, which was taken from Noyes et al. (1984). The black dashed line marks the peak from Figure 14 by Gomes da Silva et al. (2021).

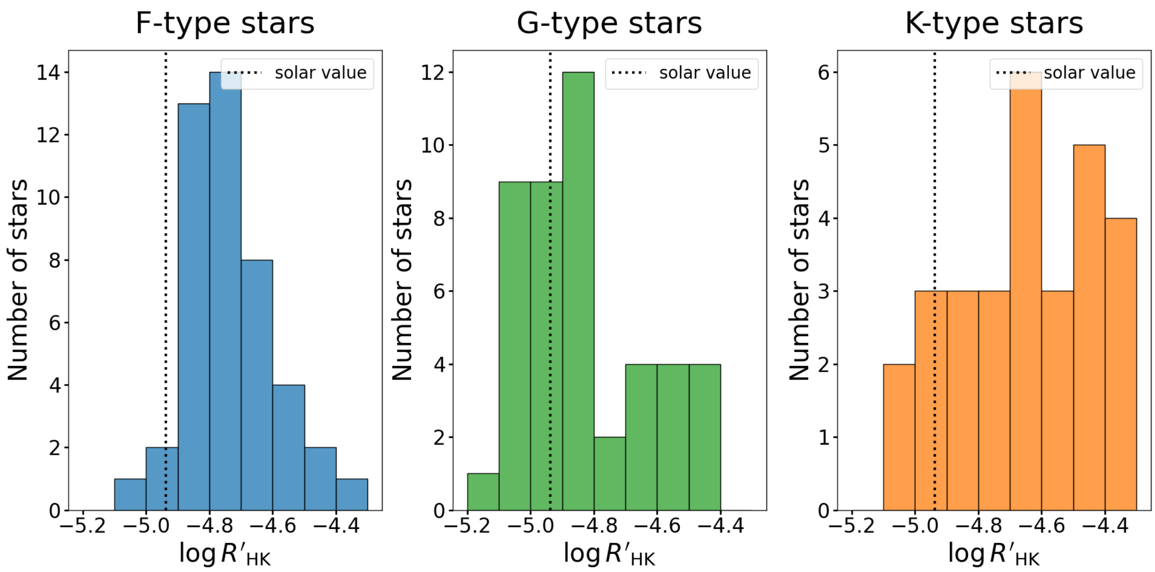

Figure 4.5: Left to right: distribution of $\log R'_{\mathrm{HK}}$ for F, G and K stars.

Figure 4.5 the distribution of the $\log R'_{\mathrm{HK}}$ values within the K-type stars of the sample can be seen. The K-dwarfs are more evenly distributed, but they still show two possible peaks. In the literature (Brown et al., 2022; Loaiza-Tacuri et al., 2024) K-dwarfs usually show a triple peaked distribution with the lowest peak at a $\log R'_{\mathrm{HK}}$ value of -5 to -4.9. This peak is not present in the analysed sample. This could be due to the small sample size of K-type stars in this work.

4.5 Temperature and $\log R'_{\mathrm{HK}}$

Since the purpose of the $\log R'_{\mathrm{HK}}$ value is to get rid of a colour dependence and therefore a temperature dependence, it is no surprise that a comparison between $\log R'_{\mathrm{HK}}$ and the effective temperatures of the stars shows no significant correlation, unlike Figure 4.2. This is visualised in Figure 4.6. One thing that can be said about it, is that the hotter stars in this sample in the range of 6700 K to 7000 K all show rather high $\log R'_{\mathrm{HK}}$ values of approximately -4.4 to -4.7, although high $\log R'_{\mathrm{HK}}$ values are also found in cooler stars. The majority of stars in this sample are solar-like stars within the temperature interval of 5500 to 6300 K. They show a higher concentration between an activity level of -4.8 to -5.0. The few M-type stars in this sample belong to the least active stars, however due to the small number of those stars, no real statement about the general activity level of this spectral type can be made. Studies with a bigger sample size of M-dwarfs usually show a broad distribution in $\log R'_{\mathrm{HK}}$ values ranging from approximately -4.0 to -6.0 (Astudillo-Defru et al., 2017; Sreejith et al., 2020; Boudreaux et al., 2022). In general the distribution of the $\log R'_{\mathrm{HK}}$ values compared to the effective temperature agrees with the literature. Boro Saikia et al. (2018) also shows a concentration of stars near the solar value and an increase of the $\log R'_{\mathrm{HK}}$ value with higher temperature (see their Figure 3). However, Mittag et al. (2013) and Suárez Mascareño et al. (2016) do not find a variability in $\log R'_{\mathrm{HK}}$ with increasing temperature. Their activity levels are evenly distributed over different temperatures. But they all have in common the increase in $\log R'_{\mathrm{HK}}$ at approximately 4500 K with a following decrease at 4000 K resulting in low activity levels of M-dwarfs compared to other spectral classes. This dent is also slightly visible in Figure 4.6, considering the small sample size.

4.6 Metallicity and $\log R'_{\mathrm{HK}}$

Figure 4.7 shows a comparison between the metallicity $[Fe/H]$ of the stars and their activity level $\log R'_{\mathrm{HK}}$. The sample covers a metallicity range of about -0.5 to +0.5, which can be considered broadly solar-like. The data points are randomly distributed over the whole range, without any clusters or correlation. Therefore, the metallicity with the range of the sample used in this work does not significantly influence the activity level of a star. The metallicity values were provided by the Ariel science consortium via private communication.

4.7 Visible Ca II HK emission and $\log R'_{\mathrm{HK}}$

To investigate why the $\log R'_{\mathrm{HK}}$ values of the F-type stars in this sample are relatively high, the emission line cores were examined more closely. All spectra were inspected manually to

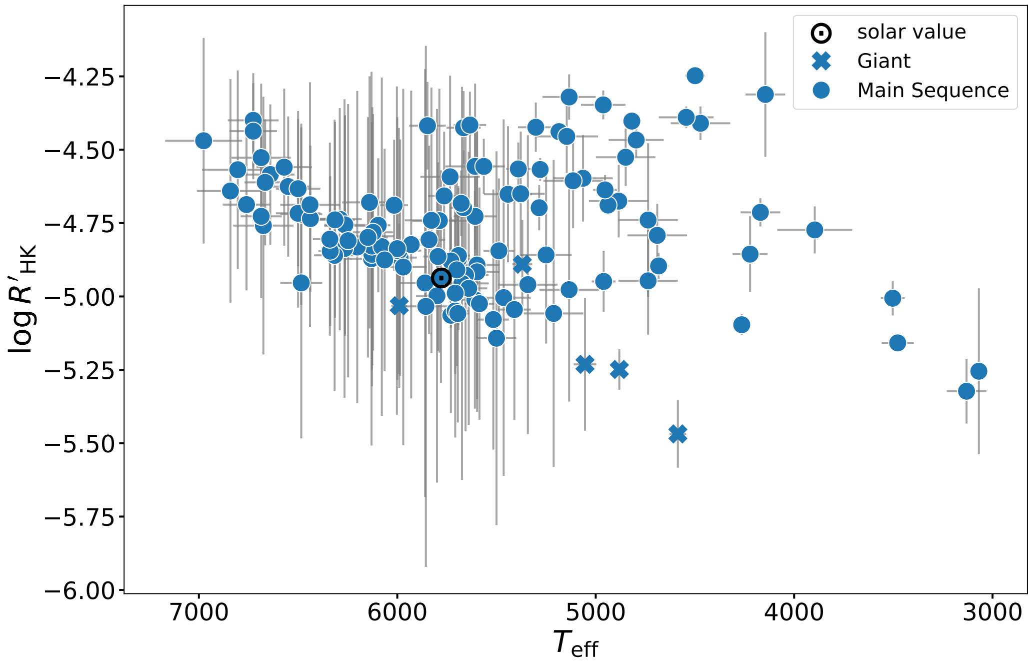

Figure 4.6: Effective temperature (x-axis) vs. $\log R'_{\mathrm{HK}}$ values (y-axis). Giant stars are marked with a cross. The ⊙ symbol indicates the solar $\log R'_{\mathrm{HK}}$ value of -4.937 which was taken from Noyes et al. (1984).

check if any visible emission is present in the Calcium II H and K lines, sorting them into two groups. The first group includes the spectra that show a spectral emission feature and the second group consists of all spectra where no spectral emission feature is visible, here only the broad photospheric absorption wings are present (see Figure 2.2 for an example). The upper panel shows a spectrum with a clearly visible emission in the Ca II H and K lines, whereas in the spectrum of the lower panel only the photospheric absorption is visible.

Figure 4.8 shows the distribution of the activity levels of the stars in these two emission categories grouped by their main spectral type. The y-axis shows their determined $\log R'_{\mathrm{HK}}$ values and the x-axis shows their spectral type. The different forms are estimated using a kernel density estimation of the underlying probability density distribution, which represents a Gaussian distribution[1]. All M and K-type stars show an chromospheric emission feature in the Ca II H and K lines. The K-dwarfs cover a broad range in their $\log R'_{\mathrm{HK}}$ values, whereas the M-stars are at rather low $\log R'_{\mathrm{HK}}$ values. The low activity levels of M-dwarfs were expected since other studies (Boro Saikia et al., 2018; Astudillo-Defru et al., 2017; Mittag et al., 2013) also show a decrease in $\log R'_{\mathrm{HK}}$ for later spectral types. The majority of F-stars show no emission feature, only the photospheric absorption wings. There are only a handful of F-stars, for which an emission is visible in the spectrum. To be precise only six out of the 46 F-type stars show an emission line. Most G-type stars are also part of the no emission group, but there is still a noticeable number of G-dwarfs with an visible emission

[1] see also the Seaborn documentation: `https://seaborn.pydata.org/generated/seaborn.violinplot.html`

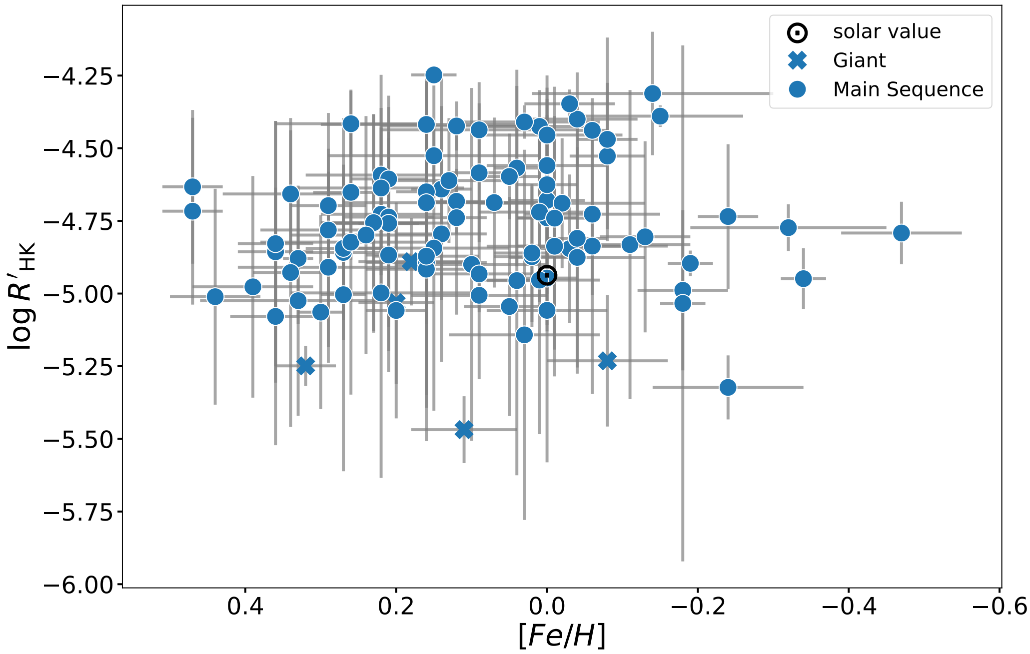

Figure 4.7: Metallicity (x-axis) vs. $\log R'_{\rm HK}$ (y-axis). Giant stars are marked with a cross. There is no correlation between the metallicity of stars and their chromospheric activity level.

feature. Out of 42 analysed G-type stars, 12 show a visible chromospheric emission feature in their Ca II H and K lines. At this point it has to be said, that some spectra were too noisy to clearly determine whether an emission is present or not. Therefore, a observational bias cannot be excluded.

A more detailed distribution of these two visual emission categories across stellar effective temperatures is shown in Figure 4.9. Again the $\log R'_{\rm HK}$ value is on the y-axis and the effective temperature is on the x-axis, with the colour of the markers denoting the emission category. Blue indicates that there is no visible emission and orange indicates a visible emission feature in the spectra. It is again clear to see that most F and G-type stars belong to the no emission group. The hotter stars are also closer together in their activity levels, with a slight decrease in $\log R'_{\rm HK}$ as the temperature decreases. The cooler stars in the sample, beginning at approximately 5500 K, cover a broader range of their $\log R'_{\rm HK}$ values. The simple appearance or non-appearance of an emission feature in a spectrum doesn't necessarily indicate a certain $\log R'_{\rm HK}$ value.

4.7.1 Rotation

Even though most F stars don't show an emission feature, their $\log R'_{\rm HK}$ are still among the highest values. Since their spectra indicate quite inactive stars, the $\log R'_{\rm HK}$ values would be expected to be rather low. A possible explanation for this phenomena is the rotation of the stars. It is well known that the magnetic activity of a star is related to its rotation

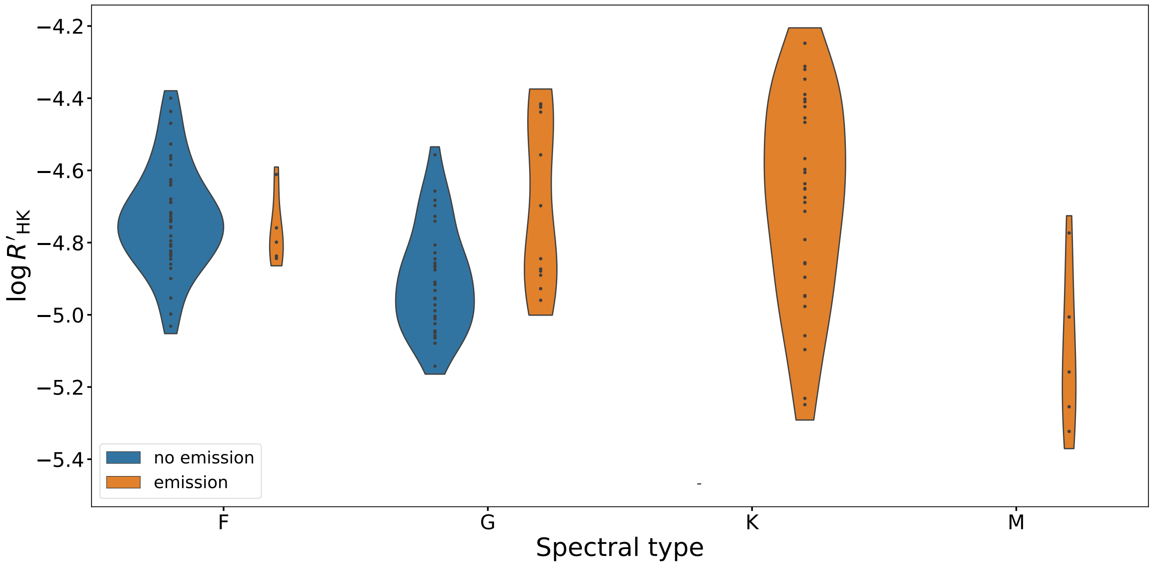

Figure 4.8: Distribution of stars with and without emission in the Ca II H and K lines. The x-axis shows the spectral type and the y-axis the activity level in log R'_{HK} values.

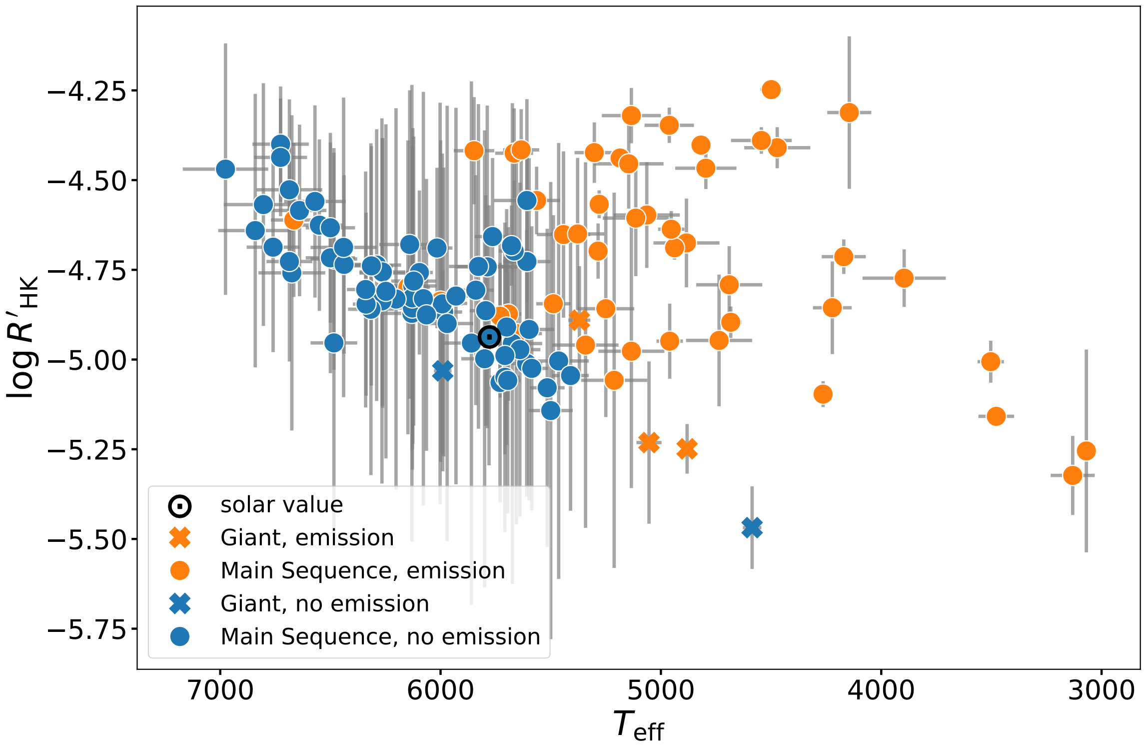

Figure 4.9: Comparison between effective temperature (x-axis) and log R'_{HK} values (y-axis). Giants are marked with a cross. Stars where no emission feature in the Ca II H and K lines is visible in the spectrum are marked in blue. Stars with a visible emission line are marked in orange. The suns position is indicated with a $\odot$ symbol.

(Schrijver and Zwaan, 2000). With a decreasing rotation, a decrease in activity can also be observed (Fritzewski et al., 2021). However, rotation also influences the spectral lines of a star. An example of the effect of different rotational velocities on spectral lines can be found in Figure 18.6 in Gray (2008). Here it can be seen that spectral lines get more shallow with a higher rotational velocity (Gray, 2008).

As discussed in Schröder et al. (2009), for fast rotating stars the absorption features of the Ca II H and K lines fill up and essentially mimic an emission flux. Furthermore, the rotational line broadening results in a loss of emission flux. For active stars these two effects cancel each other out, but for inactive stars e.g. stars without a spectral emission feature in the Ca II H and K lines cannot undergo a loss in emission, but the line filling effect in the absorption features remains. This causes high $\log R'_{\mathrm{HK}}$ values for fast rotating, inactive stars (Schröder et al., 2009).

In Figure 4.10 the rotation periods for the stars is shown. On the x-axis is the effective temperature and on the y-axis are the $\log R'_{\mathrm{HK}}$ values of the stars. The colour indicates the rotational periods in days, but because of the very broad range of the rotational periods from 1.5 days to over 200 days a logarithmic scale was applied. Bright colours indicate a fast rotation period and darker colours indicate slower rotation period. The rotation period was calculated from the rotational velocities (vsini) of the stars, which were taken from the literature. By assuming an inclination of 60° for all of the stars, like in Brown et al. (2022), the rotation periods were determined using basic trigonometry. Therefore, it is important to mention that those rotational period values are no absolute values, since the real inclination of the individual stars is not known. It is only a comparison of the stars within this specific sample. Nevertheless, it can be seen that the F-stars in this sample are indeed the faster rotating ones. This is also consistent with the literature, since fast rotators are usually found within A- and F-type stars (Schröder et al., 2009). The M-stars are the slowest rotators in this sample and they show a quite low $\log R'_{\mathrm{HK}}$ value. This can be compared to Suárez Mascareño et al. (2016), who determined rotation periods and magnetic cycles of late-type stars. They also have many slow rotating M-dwarfs with very low activity levels.

4.7.2 Age

In 1972, Skumanich stated that the rotation, as well as the Ca II emission, decrease with the inverse square root of age. The decrease in rotation is due to magnetized stellar winds causing a loss of angular momentum (Schrijver and Zwaan, 2000). The activity of sun-like stars is therefore the highest when they are young and they have not yet experience a rotational spin-down (Reiners and Basri, 2008). In Figure 4.11 the x-axis is again the effective temperature and on the y-axis are the $\log R'_{\mathrm{HK}}$ values. But now the colour indicates the age of the stars in gigayears. The values were taken from the literature (Bento et al., 2018; Hellier et al., 2017; Lendl et al., 2019; Brahm et al., 2016, 2018). To get a better visualisation with the colours a logarithmic scale was chosen. Brighter colours indicate younger stars and darker colours indicate older stars. It can be seen that the age tends to increase with decreasing effective temperature in this sample of stars used here. This means the faster rotating, hotter stars are also the younger ones in the sample. This is no surprise, since it is well known, that F-type stars are more massive compared to M-type stars and are therefore not as long on the main-sequence as less massive stars (Hanslmeier, 2020).

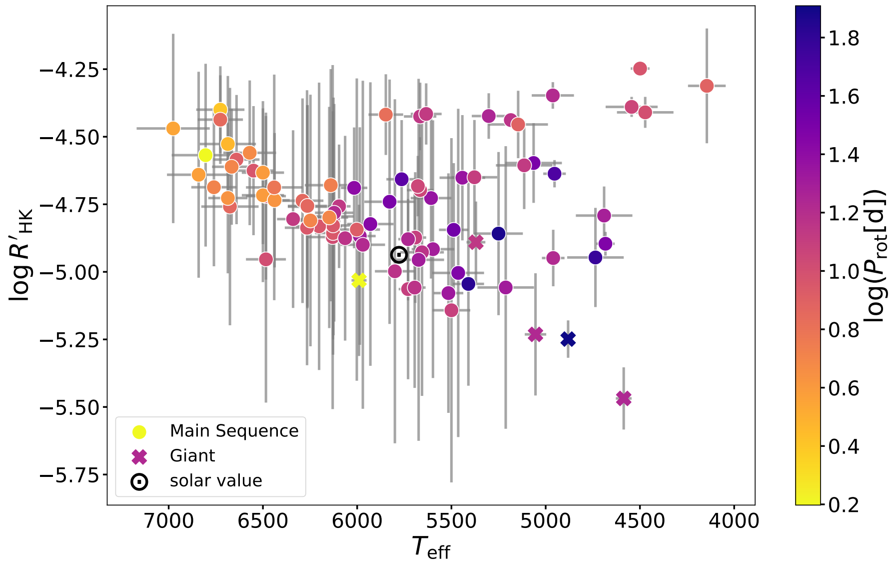

Figure 4.10: Effective temperature (x-axis) vs. $\log R'_{\mathrm{HK}}$ (y-axis). The solar values are marked with an ⊙ symbol and the giants are marked with a cross. The colour visualises the rotational periods in days, but in a logarithmic scale. Brighter colours indicate a faster rotational period, whereas darker colour indicate a slower rotational period. The rotational periods were calculated from the rotational velocities taken from literature with an assumed inclination of 60 ° taken from Brown et al. (2022).

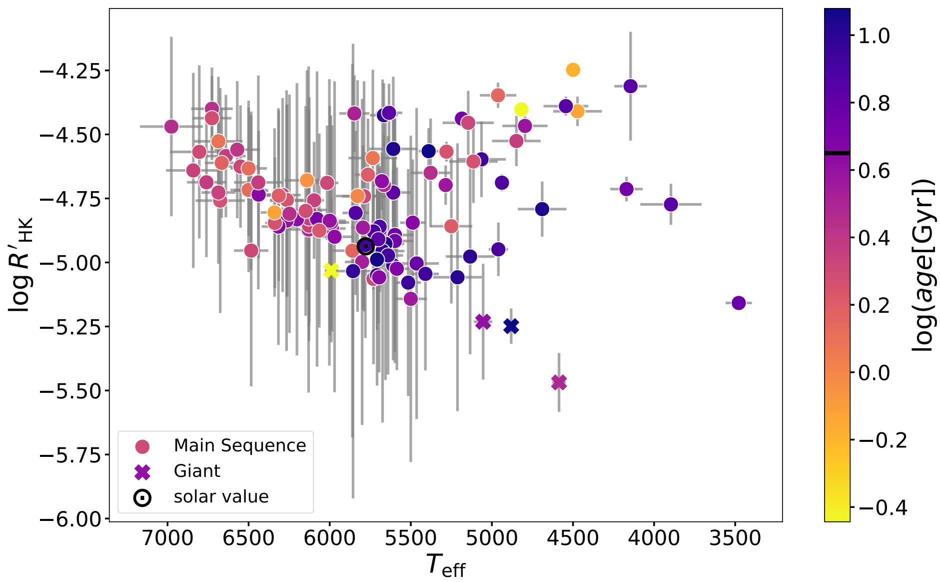

Figure 4.11: Effective temperature (x-axis) vs. $\log R'_{\mathrm{HK}}$ values (y-axis). The solar values are shown with a black ⊙ symbol and the giants are marked with a cross. The colour visualise the ages of the stars in gigayears. The darker the colour the older the star. For this a logarithmic scale was chosen. The black line on the colour-bar marks the suns age.

4.8 Most active star

Noticeably, when looking at the $\log R'_{\mathrm{HK}}$ values the five most active stars of the sample are all K-type stars as well as the least active one. Here only values with an uncertainty smaller than one are considerer. Since the range of $\log R'_{\mathrm{HK}}$ goes from approximately -4.2 to -5.5 and uncertainty of one or even more covers nearly the whole range. Such a large uncertainty prevents a reasonable statement about the activity of the star. The most active star of the analysed sample is the K5.5V-type star K2-136 with a $\log R'_{\mathrm{HK}}$ value of -4.248.

4.9 Hα-index

Another often used activity index is the Hα-index. The determination of it is explained in Chapter 3. Since the calculation of the Hα-values is not standardised, the absolute values differ for every study, which makes a comparison to literature values complicated. In Figure 4.12 the Hα-values compared to the S_{MWO} values can be seen. The x-axis represents the Hα-index and the y-axis the S_{MWO} values of the stars. A correlation between those values can be seen, as the Hα values increase with increasing S_{MWO} though there is a large scatter at high values. Most stars cluster at low values in both indices. In the literature there is no agreement if a correlation between these two activity proxies exist or if so in what way. But evidence exists that for some stars there is indeed a positive correlation, but also a negative correlation for other stars (Meunier et al., 2022; Cincunegui et al., 2007; Gomes da Silva et al., 2011b). That there is not always a clear correlation can also be seen in Figure 4.13. Here the Hα-values from the solar analogue sample were compared to their respective S_{SA}-values. The x-axis denotes S_{SA} and the y-axis Hα. The specific values together with their uncertainties can be found in Table A.3. The comparison of these values show that there indeed doesn't always have to be a clear correlation. Especially Gomes da Silva et al. (2011a) states that a correlation of these two indices also depends on the chosen bandwidth of the Hα-index.

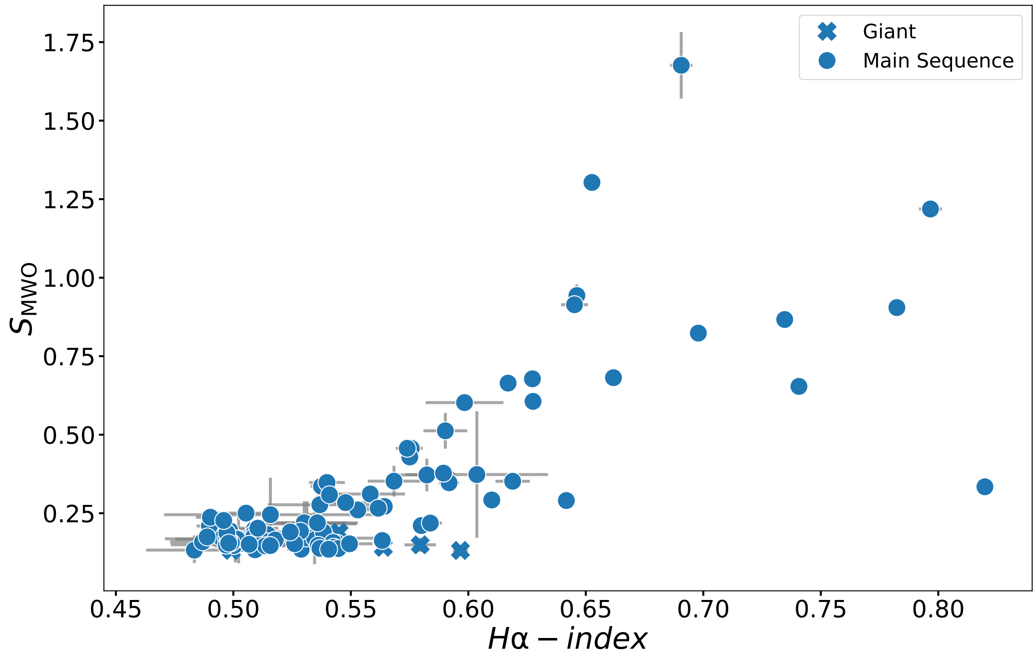

Figure 4.12: Hα-index (x-axis) vs. S_{MWO} of the Ariel sample (y-axis)

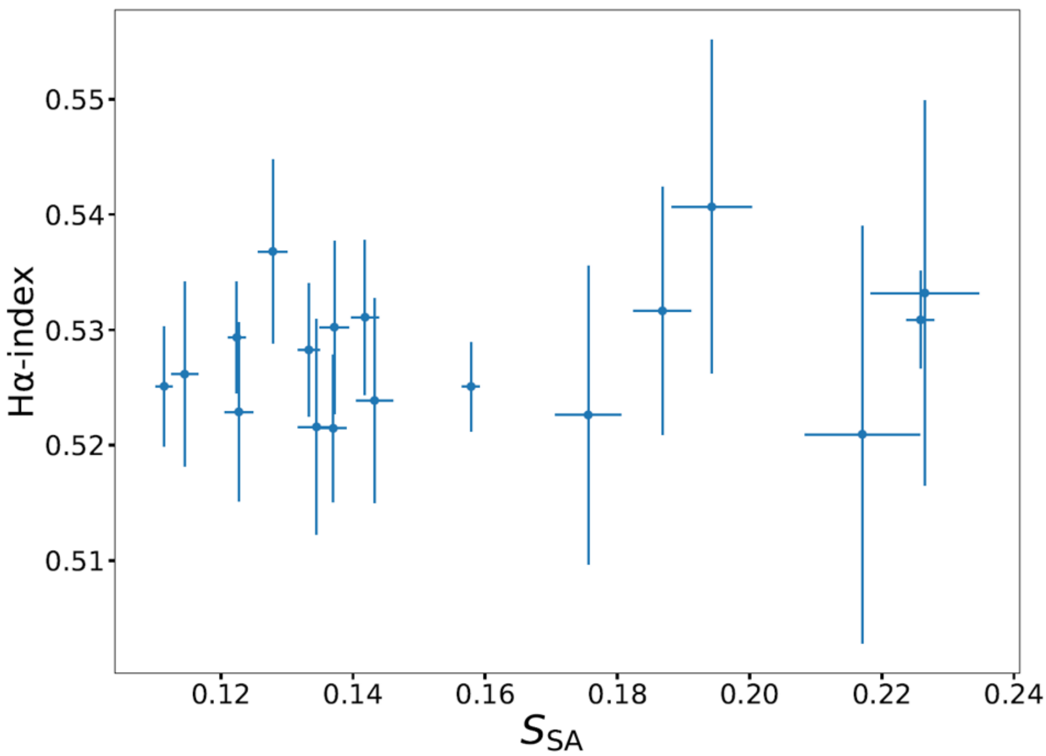

Figure 4.13: A comparison between S_{SA} and the Hα-index of the solar analogues can be seen.

Chapter 5

Conclusion

In this work the chromospheric activity of two star samples was characterised. The first sample contained 127 stars of spectral types F-G-K-M and are part of the ARIEL target catalogue. Therefore their activity levels are important parameters. Stellar activity is one of the most significant noise sources in the precise measurements required for atmospheric analysis of exoplanets. The second sample contained 18 solar analogues and are from an observing program by Beck et al. (2016, 2017) and Salabert et al. (2016a,b).

The chromospheric activity is triggered by the magnetic field and characterised by a spectral emission feature in the absorption wings of the Calcium II H and K lines. For the determination of the activity levels the Mount-Wilson S-index was chosen. This is a widely used tool to determine the chromospheric activity of main-sequence stars. It represents a ratio of the fluxes in the Calcium H and K lines to the fluxes of two nearby continuum bands on the left and right side of the lines. Since the Mount-Wilson S-index is colour and therefore temperature dependent it needs to be converted into another value, the $\log R'_{\mathrm{HK}}$, which is comparable over different spectral types.

Analysis of the $\log R'_{\mathrm{HK}}$ values revealed nuanced relationships between stellar parameters and activity. Cooler stars, particularly late K-type and early M-type stars, displayed a broader spread of activity levels, than the hotter stars in the sample. The distribution of $\log R'_{\mathrm{HK}}$ values within each analysed spectral type is also different. Where F-type stars show only one peak in their distribution, G-type stars show two peaks with a gap at the intermediate active region.

For a further characterisation, the spectral emission feature in the Calcium II H and K lines was examined more closely. The stars were put into two groups, whether a spectral emission feature is visible in the spectrum or not. This revealed that the F-type stars in this sample do not show a visible emission feature in their spectra, even tough their $\log R'_{\mathrm{HK}}$ values are among the highest compared to the other stars in the sample. This is most likely due to their faster rotation causing rotational line broadening and resulting in a higher $\log R'_{\mathrm{HK}}$.

For future work time-series observations would be particularly valuable for capturing variability and understanding long-term magnetic cycles. The Mount-Wilson S-index and therefore also $\log R'_{\mathrm{HK}}$ are only capable of calculating the activity levels of one specific observation and can at most achieve a mean value if different observations per star are available. However, stars are variable and their stellar activity also varies over time. With time-series calculations even more insight in the stellar activity can be achieved. Another promising tool for future work could be machine learning, to recognise stellar activity variations over time or to make a better analysis of emission features of the spectra in relation to the measured values. Such tools could further refine the separation of stellar and planetary signals, enhancing the precision of exoplanetary atmosphere characterisation.

Acknowledgements

This work made use of data obtained from the ESO Science Archive Facility with DOI(s): https://doi.eso.org/10.18727/archive/50 and https://doi.org/10.18727/archive/33. This work has also made use of data from the European Space Agency (ESA) mission *Gaia* (https://www.cosmos.esa.int/gaia), processed by the *Gaia* Data Processing and Analysis Consortium (DPAC, https://www.cosmos.esa.int/web/gaia/dpac/consortium). Funding for the DPAC has been provided by national institutions, in particular the institutions participating in the *Gaia* Multilateral Agreement (Gaia Collaboration et al., 2023b, 2016b; Babusiaux et al., 2023b). This work made use of Astropy:[1] a community-developed core Python package and an ecosystem of tools and resources for astronomy (Astropy Collaboration et al., 2022, 2013, 2018). This work also made use of the python packages Matplotlib (Hunter, 2007), Numpy (Harris et al., 2020) and Seaborn (Waskom, 2021). This research has made use of the SIMBAD database, operated at CDS, Strasbourg, France (Wenger et al., 2000).

[1] http://www.astropy.org

Appendix A

Tables

Table A.1: The table lists the orbital parameters of the stars, where z_{max} describes the maximum vertical distance from the galactic plane.

Star	Pericenter [kpc]	Apocenter [kpc]	z_{max}[kpc]	Eccentricity
CoRoT-11	7.46 ± 0.03	8.85 ± 0.31	0.088 ± 0.003	0.087 ± 0.021
CoRoT-11	7.43 ± 0.04	8.72 ± 0.28	0.093 ± 0.007	0.081 ± 0.019
CoRoT-28	4.23 ± 0.06	7.81 ± 0.02	0.118 ± 0.002	0.297 ± 0.007
CoRoT-3	5.69 ± 0.17	8.27 ± 0.03	0.098 ± 0.005	0.186 ± 0.015
CoRoT-3	2.16 ± 1.19	7.97 ± 0.25	0.824 ± 0.249	0.517 ± 0.119
CoRoT-7	7.74 ± 0.03	8.37 ± 0.01	0.201 ± 0.001	0.039 ± 0.002
GJ1214	7.02 ± 0.01	10.66 ± 0.05	0.701 ± 0.006	0.206 ± 0.002
GJ143	5.01 ± 0.0	8.22 ± 0.0	0.142 ± 0.001	0.243 ± 0.0
GJ436	6.64 ± 0.0	9.95 ± 0.0	0.414 ± 0.004	0.199 ± 0.0
GJ9827	7.73 ± 0.0	12.04 ± 0.02	0.38 ± 0.006	0.218 ± 0.001
HAT-P-1	8.03 ± 0.02	8.22 ± 0.01	0.454 ± 0.004	0.012 ± 0.001
HAT-P-15	7.98 ± 0.01	9.54 ± 0.03	0.108 ± 0.001	0.089 ± 0.002
HAT-P-16	7.69 ± 0.01	9.95 ± 0.02	0.16 ± 0.002	0.128 ± 0.0
HAT-P-21	8.06 ± 0.0	11.23 ± 0.02	0.982 ± 0.013	0.164 ± 0.001
HAT-P-29	14.61 ± 1.15	$nan \pm nan$	$nan \pm nan$	$nan \pm nan$
HAT-P-29	7.86 ± 0.02	9.92 ± 0.02	0.136 ± 0.002	0.116 ± 0.001
HAT-P-3	7.12 ± 0.01	8.25 ± 0.0	0.161 ± 0.002	0.074 ± 0.001
HAT-P-32	7.78 ± 0.06	9.81 ± 0.05	0.22 ± 0.008	0.114 ± 0.002
HAT-P-33	8.44 ± 0.01	9.29 ± 0.01	0.305 ± 0.004	0.048 ± 0.001
HAT-P-36	8.18 ± 0.0	9.2 ± 0.01	0.379 ± 0.005	0.059 ± 0.001
HAT-P-37	7.48 ± 0.13	8.08 ± 0.01	0.173 ± 0.008	0.033 ± 0.008
HAT-P-57	7.36 ± 0.12	8.0 ± 0.19	0.084 ± 0.009	0.054 ± 0.004
HAT-P-67	7.54 ± 0.01	9.91 ± 0.04	0.281 ± 0.002	0.136 ± 0.001
HATS-10	7.31 ± 0.06	8.25 ± 0.03	0.169 ± 0.002	0.061 ± 0.006
HATS-17	5.69 ± 0.04	8.02 ± 0.01	0.271 ± 0.003	0.17 ± 0.003
HATS-22	7.56 ± 0.02	11.02 ± 0.09	0.163 ± 0.002	0.186 ± 0.003

HATS-22	7.59 ± 0.02	11.11 ± 0.09	0.16 ± 0.004	0.188 ± 0.002
HATS-24	6.69 ± 0.04	7.71 ± 0.01	0.186 ± 0.005	0.072 ± 0.002
HATS-24	6.68 ± 0.03	7.71 ± 0.01	0.189 ± 0.003	0.072 ± 0.002
HATS-25	5.02 ± 0.06	7.88 ± 0.01	0.332 ± 0.015	0.221 ± 0.006
HATS-25	5.04 ± 0.08	7.88 ± 0.01	0.332 ± 0.016	0.22 ± 0.008
HATS-26	7.75 ± 0.02	10.66 ± 0.1	0.353 ± 0.008	0.158 ± 0.004
HATS-27	7.02 ± 0.08	7.85 ± 0.04	0.271 ± 0.004	0.058 ± 0.004
HATS-29	5.66 ± 0.02	8.03 ± 0.02	0.118 ± 0.004	0.174 ± 0.001
HATS-29	5.66 ± 0.02	8.0 ± 0.02	0.119 ± 0.003	0.174 ± 0.002
HATS-31	7.55 ± 0.05	9.12 ± 0.1	0.539 ± 0.009	0.097 ± 0.003
HATS-33	6.0 ± 0.02	7.92 ± 0.0	0.143 ± 0.004	0.138 ± 0.001
HATS-35	4.4 ± 0.57	9.51 ± 3.29	2.498 ± 1.861	0.326 ± 0.136
HATS-35	7.2 ± 0.01	8.69 ± 0.04	0.487 ± 0.008	0.094 ± 0.002
HATS-39	3.05 ± 0.81	14.93 ± 3.15	0.33 ± 0.387	0.762 ± 0.126
HATS-39	7.25 ± 0.06	9.92 ± 0.11	0.076 ± 0.003	0.152 ± 0.006
HATS-40	8.87 ± 0.02	12.39 ± 0.35	0.391 ± 0.007	0.167 ± 0.013
HATS-40	8.85 ± 0.01	12.52 ± 0.27	0.383 ± 0.009	0.175 ± 0.01
HATS-41	6.7 ± 0.05	8.64 ± 0.02	0.145 ± 0.002	0.127 ± 0.004
HATS-41	6.67 ± 0.06	8.64 ± 0.02	0.148 ± 0.003	0.129 ± 0.003
HATS-42	3.95 ± 0.85	16.36 ± 2.57	0.774 ± 0.536	0.68 ± 0.124
HATS-42	7.59 ± 0.08	9.48 ± 0.24	0.13 ± 0.007	0.117 ± 0.008
HATS-43	8.0 ± 0.08	8.31 ± 0.01	0.221 ± 0.011	0.019 ± 0.005
HATS-45	8.6 ± 0.01	9.62 ± 0.11	0.125 ± 0.001	0.057 ± 0.006
HATS-52	7.66 ± 0.06	11.0 ± 0.13	0.227 ± 0.004	0.18 ± 0.005
HATS-52	7.09 ± 0.04	22.29 ± 2.25	0.513 ± 0.06	0.523 ± 0.029
HATS-6	7.59 ± 0.08	8.45 ± 0.01	0.087 ± 0.007	0.053 ± 0.005
HATS-60	7.91 ± 0.0	9.54 ± 0.06	0.569 ± 0.018	0.093 ± 0.003
HATS-60	7.91 ± 0.0	9.59 ± 0.05	0.587 ± 0.017	0.096 ± 0.003
HATS-64	7.7 ± 0.04	9.42 ± 0.12	0.339 ± 0.008	0.103 ± 0.004
HATS-65	7.68 ± 0.01	8.24 ± 0.06	0.313 ± 0.019	0.037 ± 0.003
HATS-65	7.68 ± 0.01	8.24 ± 0.06	0.335 ± 0.016	0.037 ± 0.003
HATS-68	6.72 ± 0.03	8.75 ± 0.02	0.495 ± 0.007	0.133 ± 0.002
HATS-9	7.36 ± 0.08	7.68 ± 0.03	0.349 ± 0.012	0.021 ± 0.007
HD106315	8.07 ± 0.0	9.8 ± 0.01	0.168 ± 0.003	0.097 ± 0.001
HD1397	7.08 ± 0.01	8.11 ± 0.0	0.253 ± 0.002	0.068 ± 0.0
HD149026	7.35 ± 0.01	8.44 ± 0.0	0.247 ± 0.002	0.069 ± 0.0
HD149026	7.36 ± 0.01	8.44 ± 0.0	0.249 ± 0.002	0.068 ± 0.0
HD219666	4.81 ± 0.0	10.79 ± 0.01	0.298 ± 0.003	0.383 ± 0.001
HD221416	7.84 ± 0.0	14.49 ± 0.02	0.086 ± 0.0	0.298 ± 0.001
HD23472	7.39 ± 0.0	9.08 ± 0.0	0.386 ± 0.002	0.103 ± 0.0
HD3167	7.05 ± 0.01	8.15 ± 0.0	0.477 ± 0.004	0.073 ± 0.001
HD39091	5.42 ± 0.0	9.26 ± 0.0	0.088 ± 0.001	0.262 ± 0.0
HD80606	7.98 ± 0.0	10.05 ± 0.0	0.369 ± 0.003	0.115 ± 0.0
HD89345	7.16 ± 0.0	8.66 ± 0.0	0.127 ± 0.001	0.095 ± 0.0
K2-105	7.75 ± 0.0	11.25 ± 0.02	0.124 ± 0.001	0.184 ± 0.001

K2-107	6.92 ± 0.03	7.5 ± 0.04	0.315 ± 0.007	0.042 ± 0.002
K2-107	1.21 ± 0.65	2.89 ± 0.96	1.213 ± 0.453	0.431 ± 0.056
K2-110	7.2 ± 0.02	9.47 ± 0.01	0.938 ± 0.014	0.136 ± 0.001
K2-115	6.37 ± 0.03	9.53 ± 0.12	0.25 ± 0.013	0.2 ± 0.005
K2-132	5.26 ± 0.04	8.34 ± 0.01	0.496 ± 0.01	0.226 ± 0.004
K2-136	7.29 ± 0.01	8.86 ± 0.02	0.092 ± 0.002	0.097 ± 0.002
K2-138	7.86 ± 0.0	8.84 ± 0.02	0.174 ± 0.003	0.059 ± 0.001
K2-139	7.56 ± 0.01	8.92 ± 0.0	0.163 ± 0.002	0.082 ± 0.001
K2-140	8.03 ± 0.0	9.29 ± 0.03	0.385 ± 0.007	0.073 ± 0.002
K2-141	7.75 ± 0.0	8.98 ± 0.01	0.048 ± 0.002	0.073 ± 0.0
K2-172	6.86 ± 0.01	11.69 ± 0.04	0.338 ± 0.009	0.26 ± 0.002
K2-179	8.09 ± 0.01	10.36 ± 0.0	0.178 ± 0.004	0.123 ± 0.001
K2-18	7.25 ± 0.01	8.23 ± 0.0	0.081 ± 0.005	0.063 ± 0.001
K2-21	6.97 ± 0.02	8.29 ± 0.01	0.102 ± 0.009	0.087 ± 0.001
K2-222	7.98 ± 0.0	10.3 ± 0.03	0.488 ± 0.009	0.127 ± 0.001
K2-229	7.0 ± 0.02	8.26 ± 0.0	0.388 ± 0.007	0.083 ± 0.001
K2-232	6.06 ± 0.01	8.28 ± 0.0	0.197 ± 0.001	0.155 ± 0.001
K2-233	8.04 ± 0.0	8.47 ± 0.0	0.055 ± 0.0	0.026 ± 0.0
K2-237	7.67 ± 0.03	8.13 ± 0.05	0.141 ± 0.003	0.029 ± 0.005
K2-237	0.25 ± 0.75	1.84 ± 3.33	0.385 ± 1.708	0.805 ± 0.225
K2-261	6.29 ± 0.02	8.26 ± 0.0	0.338 ± 0.004	0.136 ± 0.001
K2-266	6.97 ± 0.01	9.08 ± 0.02	0.229 ± 0.007	0.132 ± 0.0
K2-280	7.33 ± 0.01	7.87 ± 0.02	0.128 ± 0.003	0.035 ± 0.001
K2-287	6.84 ± 0.01	9.01 ± 0.01	0.247 ± 0.002	0.137 ± 0.001
K2-290	7.2 ± 0.01	10.37 ± 0.01	0.307 ± 0.004	0.18 ± 0.001
K2-3	7.05 ± 0.01	8.96 ± 0.01	0.498 ± 0.013	0.12 ± 0.0
K2-36	8.13 ± 0.0	9.35 ± 0.04	0.348 ± 0.013	0.069 ± 0.002
K2-39	6.03 ± 0.01	10.8 ± 0.01	0.23 ± 0.001	0.284 ± 0.001
K2-58	7.89 ± 0.0	8.85 ± 0.02	0.128 ± 0.002	0.058 ± 0.001
K2-98	5.7 ± 0.02	9.25 ± 0.01	0.224 ± 0.001	0.237 ± 0.002
K2-99	7.68 ± 0.01	8.96 ± 0.01	0.46 ± 0.005	0.077 ± 0.0
KELT-1	7.76 ± 0.03	9.21 ± 0.04	0.126 ± 0.004	0.086 ± 0.0
KELT-11	5.34 ± 0.01	8.14 ± 0.0	0.117 ± 0.001	0.207 ± 0.001
KELT-18	7.5 ± 0.02	8.44 ± 0.01	0.278 ± 0.003	0.06 ± 0.001
KELT-18	7.54 ± 0.02	8.42 ± 0.01	0.27 ± 0.004	0.056 ± 0.002
KELT-3	7.11 ± 0.01	8.58 ± 0.0	0.271 ± 0.003	0.094 ± 0.001
KELT-3	7.02 ± 0.04	8.59 ± 0.01	0.269 ± 0.004	0.101 ± 0.003
KELT-4A	7.57 ± 0.0	10.07 ± 0.02	0.226 ± 0.002	0.142 ± 0.001
KELT-7	7.12 ± 0.01	8.8 ± 0.01	0.105 ± 0.001	0.106 ± 0.001
Kepler1514	7.25 ± 0.03	8.43 ± 0.01	0.09 ± 0.001	0.076 ± 0.001
Kepler1515	1.58 ± 0.7	15.44 ± 15.65	2.079 ± 15.851	0.924 ± 0.119
Kepler1515	6.4 ± 0.1	8.31 ± 0.02	0.256 ± 0.007	0.13 ± 0.008
Kepler25	8.04 ± 0.0	8.66 ± 0.03	0.148 ± 0.001	0.037 ± 0.002
Kepler91	4.91 ± 0.02	8.42 ± 0.01	0.33 ± 0.004	0.265 ± 0.002
LHS1140	5.8 ± 0.01	8.2 ± 0.0	0.148 ± 0.008	0.171 ± 0.0

NGTS-2	7.37 ± 0.01	8.74 ± 0.04	0.208 ± 0.003	0.083 ± 0.002
PH2	7.47 ± 0.09	8.62 ± 0.1	0.149 ± 0.009	0.077 ± 0.003
Qatar8	6.98 ± 0.01	9.35 ± 0.02	0.303 ± 0.005	0.145 ± 0.001
TRES1	5.14 ± 0.47	$nan \pm nan$	$nan \pm nan$	$nan \pm nan$
TRES1	6.79 ± 0.02	8.31 ± 0.01	0.266 ± 0.002	0.101 ± 0.001
TRES2	8.08 ± 0.0	9.42 ± 0.14	0.104 ± 0.005	0.077 ± 0.007
WASP-11	7.93 ± 0.02	8.38 ± 0.01	0.203 ± 0.004	0.027 ± 0.001
WASP-118	7.69 ± 0.02	8.54 ± 0.0	0.347 ± 0.004	0.053 ± 0.001
WASP-121	7.13 ± 0.01	8.54 ± 0.0	0.113 ± 0.001	0.09 ± 0.001
WASP-124	6.62 ± 0.02	8.0 ± 0.01	0.381 ± 0.007	0.096 ± 0.001
WASP-127	8.03 ± 0.0	11.31 ± 0.01	0.29 ± 0.002	0.17 ± 0.001
WASP-133	6.77 ± 0.03	8.15 ± 0.02	0.322 ± 0.004	0.092 ± 0.002
WASP-135	6.01 ± 0.05	7.98 ± 0.0	0.2 ± 0.006	0.14 ± 0.004
WASP-14	7.83 ± 0.0	10.46 ± 0.01	0.202 ± 0.002	0.144 ± 0.0
WASP-140	8.16 ± 0.0	10.59 ± 0.02	0.074 ± 0.002	0.129 ± 0.001
WASP-141	7.33 ± 0.04	8.48 ± 0.0	0.256 ± 0.002	0.073 ± 0.003
WASP-142	6.98 ± 0.05	9.79 ± 0.05	0.373 ± 0.006	0.168 ± 0.003
WASP-147	7.6 ± 0.01	9.16 ± 0.01	0.459 ± 0.007	0.094 ± 0.001
WASP-157	6.64 ± 0.03	8.3 ± 0.01	0.32 ± 0.006	0.111 ± 0.002
WASP-158	8.14 ± 0.0	9.64 ± 0.04	0.63 ± 0.015	0.084 ± 0.002
WASP-159	8.37 ± 0.03	8.57 ± 0.05	0.592 ± 0.011	0.014 ± 0.002
WASP-160B	6.07 ± 0.03	9.49 ± 0.04	0.447 ± 0.01	0.22 ± 0.001
WASP-165	6.22 ± 0.05	9.09 ± 0.02	0.827 ± 0.022	0.188 ± 0.004
WASP-167	7.5 ± 0.03	8.05 ± 0.02	0.256 ± 0.004	0.036 ± 0.002
WASP-168	6.43 ± 0.06	8.31 ± 0.16	0.101 ± 0.025	0.129 ± 0.005
WASP-168	6.47 ± 0.05	8.34 ± 0.0	0.105 ± 0.003	0.127 ± 0.004
WASP-173A	5.35 ± 0.02	9.25 ± 0.01	0.223 ± 0.005	0.267 ± 0.002
WASP-46	6.96 ± 0.02	7.89 ± 0.02	0.217 ± 0.002	0.062 ± 0.001
WASP-53	8.11 ± 0.0	10.56 ± 0.02	0.231 ± 0.011	0.132 ± 0.001
WASP-59	6.3 ± 0.02	8.54 ± 0.0	0.771 ± 0.005	0.151 ± 0.001
WASP-60	5.6 ± 0.04	8.57 ± 0.01	0.178 ± 0.003	0.209 ± 0.003
WASP-80	7.34 ± 0.0	9.6 ± 0.02	0.4 ± 0.002	0.133 ± 0.001
WASP-84	7.91 ± 0.0	9.43 ± 0.01	0.196 ± 0.002	0.088 ± 0.001
WASP-85	7.09 ± 0.01	8.89 ± 0.01	0.196 ± 0.005	0.113 ± 0.001
WASP-85	7.07 ± 0.01	8.9 ± 0.01	0.195 ± 0.005	0.114 ± 0.001
WASP-89	4.63 ± 0.04	8.11 ± 0.02	0.707 ± 0.025	0.274 ± 0.003
Wolf503	3.4 ± 0.0	8.12 ± 0.0	1.67 ± 0.004	0.41 ± 0.001
XO1	8.04 ± 0.0	9.17 ± 0.01	0.348 ± 0.005	0.066 ± 0.001
XO3	8.06 ± 0.01	9.68 ± 0.01	0.121 ± 0.001	0.092 ± 0.0
XO5	7.79 ± 0.01	8.4 ± 0.01	0.464 ± 0.01	0.038 ± 0.001

Table A.2: Calibration values separated by instrument. $S_{\mathrm{HARPS-N}}$, S_{HARPS} and S_{UVES} are the calculated average values from the spectra before the calibration was applied and S_{err} are their respective uncertainties. For the calculation, a number of N_{obs} spectra were used. S_{MWO} indicates the original Mount Wilson S-index value from Baliunas et al. (1995). The difference between the calibrated and the original values is described by $\Delta S = calib(S) - S_{\mathrm{MWO}}$. Since for the UVES calibration, HARPS stars were needed, the S_{HARPS} value for each star is also given in the bottom table.

HARPS-N

Star	Spectral type	S_{HARPN}	S_{err}	S_{MWO}	ΔS	N_{obs}
HD10700	G8V[1]	0.1303	0.0014	0.1710	0.0029	91
HD16160	K3V[1]	0.1610	0.0078	0.2260	-0.0145	11
HD115404	K2V[2]	0.4258	0.0166	0.5350	0.0017	12
HD120136	F7IV-V[3]	0.1455	0.0056	0.1910	0.0016	133
HD141004	G0V[1]	0.1203	0.0019	0.1550	0.0066	8
HD182572	G7IV[1]	0.1075	0.0007	0.1480	-0.0021	2
HD217014	G2IV[1]	0.1131	0.0009	0.1490	0.0038	10

HARPS

Star	Spectral type	S_{HARPS}	S_{err}	S_{MWO}	ΔS	N_{obs}
HD10700	G8V[1]	0.1295	0.0015	0.1710	0.0027	20
HD16160	K3V[1]	0.1673	0.0127	0.2260	-0.0195	23
HD23249	K0IV[1]	0.0992	0.0035	0.1370	0.3522	22
HD152391	G8.5V[4]	0.3434	0.0170	0.3930	-0.2030	24
HD160346	K3V[1]	0.2401	0.0307	0.3000	-0.1369	28
HD216385	F6V[5]	0.1084	0.0065	0.1420	0.0074	22
HD219834	G8.5IV[4]	0.1125	0.0077	0.1550	0.0004	20

UVES

Star	Spectral type	S_{HARPS}	S_{UVES}	S_{err}	S_{MWO}	ΔS	N_{obs}
HD39194	K0V[4]	0.1349	0.1364	0.0009	0.1803	-0.0007	4
HD46375	G9V[6]	0.1367	0.1325	0.0007	0.1761	0.0057	12
HD73256	G8IV-V[4]	0.3242	0.3099	0.0068	0.3655	0.0464	20
HD75289	F9V[4]	0.1031	0.1083	0.0002	0.1503	-0.0098	4
HD140538	G2.5V[1]	0.1653	0.1580	0.0010	0.2033	0.0135	6
HD193901	F7V[7]	0.1247	0.1262	0.0087	0.1694	-0.0023	1

References for spectral types:
1. Keenan and McNeil (1989)
2. White et al. (2007)
3. Gray et al. (2001)
4. Gray et al. (2006)
5. Gray et al. (2003)
6. Grieves et al. (2018)
7. Houk and Smith-Moore (1988)

Table A.3: Here the values of the Hα-index and S_{SA} are listed.

Star	Hα-index	S_{SA}
KIC3241581	0.531 ± 0.007	0.142 ± 0.002
KIC3656476	0.537 ± 0.008	0.128 ± 0.002
KIC4914923	0.529 ± 0.005	0.122 ± 0.001
KIC5084157	0.532 ± 0.011	0.187 ± 0.004
KIC5774694	0.531 ± 0.004	0.226 ± 0.002
KIC6116048	0.525 ± 0.005	0.111 ± 0.001
KIC6593461	0.523 ± 0.013	0.176 ± 0.005
KIC7296438	0.523 ± 0.008	0.123 ± 0.002
KIC7680114	0.521 ± 0.006	0.137 ± 0.002
KIC7700968	0.530 ± 0.007	0.137 ± 0.002
KIC9049593	0.522 ± 0.009	0.134 ± 0.003
KIC9098294	0.528 ± 0.006	0.133 ± 0.002
KIC10130724	0.541 ± 0.014	0.194 ± 0.006
KIC10215584	0.524 ± 0.009	0.143 ± 0.003
KIC10644253	0.525 ± 0.004	0.158 ± 0.001
KIC10971974	0.533 ± 0.017	0.227 ± 0.008
KIC11127479	0.521 ± 0.018	0.217 ± 0.009
KIC11971746	0.526 ± 0.008	0.115 ± 0.002

Table A.4: The calibrated S_{MWO} values and the $\log R'_{\mathrm{HK}}$ values for each star are listed here. The column "Emission" describes if a visual emission feature in the spectra can be seen ("yes") or not ("no"). If a spectrum was too noisy to determine whether an emission is present or not, it is indicated by NaN.

Star	Spec. type	S_{MWO}	$\log R'_{\mathrm{HK}}$	Emission	Instrument
CoRoT-11	F6V	0.198 ± 0.003	-4.568 ± 0.338	no	HARPS
CoRoT-28	G8/9IV	0.311 ± 0.016	-4.565 ± 0.09	NaN	HARPS
CoRoT-3	F3V	0.182 ± 0.003	-4.641 ± 0.381	no	HARPS
CoRoT-7	K0V	0.334 ± 0.001	-4.567 ± 0.039	yes	HARPS
GJ1214	M4.5V	1.219 ± 0.022	-5.255 ± 0.283	yes	HARPS
GJ143	K4.5V	0.606 ± 0.001	-4.467 ± 0.058	yes	HARPS
GJ436	M3V	0.654 ± 0.003	-5.158 ± 0.019	yes	HARPS-N
GJ9827	K6V	0.682 ± 0.021	-4.713 ± 0.048	yes	HARPS
HAT-P-1	G0V	0.155 ± 0.001	-4.868 ± 0.402	no	HARPS-N
HAT-P-15	G5	0.212 ± 0.002	-4.727 ± 0.298	no	HARPS-N
HAT-P-16	F8	0.163 ± 0.002	-4.795 ± 0.44	no	HARPS-N
HAT-P-21	G3	0.336 ± 0.003	-4.425 ± 0.125	yes	HARPS-N
HAT-P-29	F8	0.171 ± 0.002	-4.758 ± 0.228	no	HARPS-N
HAT-P-3	K1V	0.211 ± 0.002	-4.858 ± 0.302	yes	HARPS-N
HAT-P-32	F	0.25 ± 0.007	-4.4 ± 0.161	no	HARPS-N
HAT-P-33	F4	0.172 ± 0.002	-4.687 ± 0.292	no	HARPS-N

HAT-P-36	G5V	0.348 ± 0.006	-4.416 ± 0.113	yes	HARPS-N
HAT-P-37	G	0.134 ± 0.002	-5.142 ± 0.637	no	HARPS-N
HAT-P-57	A8V	0.276 ± 0.004	-4.437 ± 2.136	no	HARPS-N
HAT-P-67	F5IV	0.209 ± 0.002	-4.527 ± 0.252	no	HARPS-N
HATS-10	F-G	0.159 ± 0.011	-4.844 ± 0.559	yes	UVES
HATS-17	G	0.135 ± 0.012	-5.064 ± 0.333	no	HARPS
HATS-22	KV	0.373 ± 0.201	-4.74 ± 0.262	NaN	HARPS
HATS-22	K	0.257 ± 0.056	-4.947 ± 0.184	yes	UVES
HATS-24	FV	0.187 ± 0.014	-4.679 ± 0.43	no	UVES
HATS-25	G	0.169 ± 0.009	-4.873 ± 0.242	yes	UVES
HATS-25	G	0.171 ± 0.043	-4.861 ± 0.237	NaN	HARPS
HATS-27	F	0.195 ± 0.026	-4.585 ± 0.239	no	HARPS
HATS-29	F	0.171 ± 0.083	-4.893 ± 0.456	NaN	HARPS
HATS-29	G	0.166 ± 0.011	-4.916 ± 0.477	no	UVES
HATS-33	G	0.216 ± 0.072	-4.697 ± 0.196	no	HARPS
HATS-35	F	0.168 ± 0.078	-4.737 ± 0.379	no	HARPS
HATS-39	F	0.186 ± 0.023	-4.625 ± 0.239	no	HARPS
HATS-40	F	0.167 ± 0.005	-4.72 ± 0.309	no	UVES
HATS-40	F	0.133 ± 0.041	-4.954 ± 0.53	no	HARPS
HATS-41	F	0.185 ± 0.006	-4.633 ± 0.264	no	UVES
HATS-41	F	0.168 ± 0.041	-4.717 ± 0.321	no	HARPS
HATS-43	K	0.372 ± 0.052	-4.597 ± 0.148	yes	HARPS
HATS-45	F	0.109 ± 0.54	-5.249 ± 1.729	no	HARPS
HATS-52	G	0.245 ± 0.118	-4.592 ± 0.345	NaN	HARPS
HATS-60	G	0.165 ± 0.01	-4.879 ± 0.227	yes	UVES
HATS-64	F	0.159 ± 0.027	-4.758 ± 0.439	no	HARPS
HATS-65	F	0.165 ± 0.007	-4.759 ± 0.375	yes	UVES
HATS-65	F	0.166 ± 0.036	-4.756 ± 0.373	no	HARPS
HATS-68	F-G	0.15 ± 0.056	-4.871 ± 0.637	no	HARPS
HATS-9	G	0.16 ± 0.017	-4.928 ± 0.531	yes	UVES
HD106315	F5V	0.165 ± 0.001	-4.735 ± 0.249	no	HARPS
HD1397	G5III/IV	0.19 ± 0.001	-4.845 ± 0.247	yes	HARPS
HD149026	G0IV	0.152 ± 0.002	-4.856 ± 0.45	no	HARPS-N
HD149026	G0IV	0.157 ± 0.002	-4.828 ± 0.422	no	HARPS-N
HD219666	G5V	0.154 ± 0.001	-4.955 ± 0.67	no	HARPS
HD221416	K0IV/V	0.141 ± 0.0	-5.231 ± 0.226	yes	HARPS
HD23472	K3.5V	0.292 ± 0.001	-4.896 ± 0.044	yes	HARPS
HD3167	K0V	0.163 ± 0.003	-5.058 ± 0.523	yes	HARPS
HD39091	G0V	0.159 ± 0.0	-4.845 ± 0.419	no	HARPS
HD80606	G8V	0.157 ± 0.001	-5.004 ± 0.607	no	HARPS-N
HD89345	G5	0.148 ± 0.005	-5.011 ± 0.371	no	HARPS
HIP41378	F6	0.154 ± 0.001	-4.832 ± 0.532	no	HARPS
K2-105	K1	0.261 ± 0.003	-4.652 ± 0.232	yes	HARPS-N
K2-107	F9IV	0.15 ± 0.009	-4.9 ± 0.607	no	UVES
K2-110	K2V	0.219 ± 0.003	-4.949 ± 0.105	yes	HARPS-N

K2-115	G4	0.277 ± 0.07	-4.557 ± 0.282	no	HARPS
K2-136	K5.5V	1.303 ± 0.006	-4.248 ± 0.011	yes	HARPS-N
K2-138	K1V	0.272 ± 0.001	-4.65 ± 0.212	yes	HARPS
K2-139	K0V	0.352 ± 0.049	-4.606 ± 0.162	yes	HARPS
K2-140	G5	0.22 ± 0.068	-4.683 ± 0.112	no	HARPS
K2-141	K7V	0.943 ± 0.035	-4.41 ± 0.057	yes	HARPS
K2-172	G-K	0.174 ± 0.008	-4.96 ± 0.509	yes	UVES
K2-179	K3	0.602 ± 0.024	-4.32 ± 0.077	yes	HARPS-N
K2-18	M2.5	0.867 ± 0.011	-5.006 ± 0.059	yes	HARPS
K2-21	K7V	0.481 ± 0.063	-4.856 ± 0.129	yes	UVES
K2-222	G0	0.174 ± 0.001	-4.807 ± 0.32	no	HARPS-N
K2-229	G9	0.457 ± 0.005	-4.438 ± 0.026	yes	HARPS-N
K2-232	G0	0.146 ± 0.019	-4.954 ± 0.729	no	HARPS
K2-233	K3	0.678 ± 0.009	-4.402 ± 0.013	yes	HARPS
K2-237	F6V	0.202 ± 0.023	-4.559 ± 0.268	no	HARPS
K2-261	G7IV-V	0.142 ± 0.009	-5.079 ± 0.443	no	HARPS
K2-266	K5V	0.29 ± 0.013	-5.096 ± 0.036	yes	HARPS
K2-280	G	0.138 ± 0.014	-5.049 ± 0.431	no	HARPS
K2-287	G	0.137 ± 0.012	-5.058 ± 0.371	no	HARPS
K2-290	FIV	0.151 ± 0.002	-4.837 ± 0.509	no	HARPS-N
K2-3	M1V	0.823 ± 0.027	-4.773 ± 0.08	yes	HARPS
K2-36	K3	0.664 ± 0.005	-4.347 ± 0.049	yes	HARPS-N
K2-39	K	0.149 ± 0.023	-5.249 ± 0.069	yes	HARPS
K2-58	K	0.372 ± 0.028	-4.675 ± 0.124	yes	UVES
K2-98	F7	0.158 ± 0.004	-4.83 ± 0.576	no	HARPS-N
K2-99	F7	0.132 ± 0.001	-5.032 ± 0.28	no	HARPS-N
KELT-1	F5	0.208 ± 0.003	-4.606 ± 1.185	no	HARPS-N
KELT-11	G8-K0IV	0.189 ± 0.001	-4.89 ± 0.151	yes	HARPS
KELT-18	F4V	0.237 ± 0.003	-4.437 ± 0.164	no	HARPS-N
KELT-4A	F	0.147 ± 0.003	-4.86 ± 0.462	no	HARPS-N
KELT-7	F2	0.216 ± 0.0	-4.559 ± 1.034	no	HARPS-N
Kepler-1	G	0.165 ± 0.002	-4.864 ± 0.321	no	HARPS-N
Kepler-1514	F7V	0.167 ± 0.002	-4.739 ± 0.333	no	HARPS-N
Kepler-1515	F6V	0.148 ± 0.001	-4.846 ± 0.255	no	HARPS-N
Kepler-25	F6	0.156 ± 0.001	-4.81 ± 0.466	no	HARPS-N
Kepler-91	K1IV	0.131 ± 0.001	-5.468 ± 0.115	no	HARPS-N
LHS1140	M4.5V	0.905 ± 0.01	-5.323 ± 0.11	yes	HARPS
NGTS-2	F5V	0.164 ± 0.006	-4.727 ± 0.279	no	HARPS
PH2	F9	0.193 ± 0.003	-4.742 ± 0.449	no	HARPS-N
Qatar8	G0V	0.153 ± 0.002	-4.972 ± 0.465	no	HARPS-N
TOI-1236	G-K	0.266 ± 0.004	-4.698 ± 0.077	yes	HARPS-N
WASP-11	K3V	0.347 ± 0.004	-4.689 ± 0.033	yes	HARPS-N
WASP-118	F6	0.175 ± 0.003	-4.688 ± 0.417	no	HARPS-N
WASP-121	F6V	0.188 ± 0.004	-4.611 ± 0.215	yes	HARPS
WASP-124	F9	0.191 ± 0.011	-4.689 ± 0.224	no	UVES

WASP-127	G5	0.147 ± 0.003	-4.989 ± 0.276	no	HARPS
WASP-133	G4	0.161 ± 0.01	-4.909 ± 0.329	no	UVES
WASP-14	F5V	0.155 ± 0.001	-4.805 ± 0.329	no	HARPS-N
WASP-140	K0	0.429 ± 0.014	-4.423 ± 0.084	yes	HARPS
WASP-141	F9	0.166 ± 0.007	-4.781 ± 0.403	no	UVES
WASP-142	F8	0.166 ± 0.01	-4.823 ± 0.525	no	UVES
WASP-147	G4	0.153 ± 0.005	-4.933 ± 0.362	no	UVES
WASP-157	G2V	0.219 ± 0.05	-4.657 ± 0.219	no	HARPS
WASP-158	F6V	0.161 ± 0.006	-4.799 ± 0.409	yes	UVES
WASP-159	F9	0.142 ± 0.004	-4.998 ± 0.637	no	UVES
WASP-160B	K0V	0.189 ± 0.013	-4.977 ± 0.381	yes	UVES
WASP-165	G6	0.147 ± 0.006	-5.025 ± 0.396	no	UVES
WASP-168	F9V	0.16 ± 0.005	-4.837 ± 0.448	yes	UVES
WASP-173A	G2	0.309 ± 0.004	-4.418 ± 0.149	yes	HARPS
WASP-46	G6	0.135 ± 0.004	-5.034 ± 0.888	NaN	HARPS
WASP-53	K3	0.378 ± 0.005	-4.637 ± 0.051	yes	HARPS
WASP-59	K5V	0.914 ± 0.018	-4.39 ± 0.037	yes	HARPS-N
WASP-60	G1V	0.151 ± 0.002	-4.876 ± 0.379	no	HARPS-N
WASP-80	K7V-M0V	1.676 ± 0.106	-4.312 ± 0.212	yes	HARPS
WASP-84	K1	0.457 ± 0.027	-4.455 ± 0.125	yes	HARPS
WASP-85	G5	0.284 ± 0.029	-4.557 ± 0.094	yes	HARPS
WASP-89	K3	0.512 ± 0.057	-4.526 ± 0.098	NaN	HARPS
Wolf503	K3.5V	0.352 ± 0.008	-4.792 ± 0.108	yes	HARPS-N
XO-1	G1V	0.19 ± 0.003	-4.741 ± 0.452	no	HARPS-N
XO-3	F5V	0.227 ± 0.001	-4.469 ± 0.35	no	HARPS-N
XO-5	G7	0.153 ± 0.004	-5.045 ± 0.377	no	HARPS-N

Bibliography

Melike Afşar, Zeynep Bozkurt, Gamze Böcek Topcu, Sergen Özdemir, Christopher Sneden, Gregory N. Mace, Daniel T. Jaffe, and Ricardo López-Valdivia. Effective Temperature Estimations from Line Depth Ratios in the H- and K-band Spectra of IGRINS. ApJ, 949 (2):86, June 2023. doi: 10.3847/1538-4357/acc946.

Astropy Collaboration, Thomas P. Robitaille, Erik J. Tollerud, Perry Greenfield, Michael Droettboom, Erik Bray, Tom Aldcroft, Matt Davis, Adam Ginsburg, Adrian M. Price-Whelan, Wolfgang E. Kerzendorf, Alexander Conley, Neil Crighton, Kyle Barbary, Demitri Muna, Henry Ferguson, Frédéric Grollier, Madhura M. Parikh, Prasanth H. Nair, Hans M. Unther, Christoph Deil, Julien Woillez, Simon Conseil, Roban Kramer, James E. H. Turner, Leo Singer, Ryan Fox, Benjamin A. Weaver, Victor Zabalza, Zachary I. Edwards, K. Azalee Bostroem, D. J. Burke, Andrew R. Casey, Steven M. Crawford, Nadia Dencheva, Justin Ely, Tim Jenness, Kathleen Labrie, Pey Lian Lim, Francesco Pierfederici, Andrew Pontzen, Andy Ptak, Brian Refsdal, Mathieu Servillat, and Ole Streicher. Astropy: A community Python package for astronomy. A&A, 558:A33, October 2013. doi: 10.1051/0004-6361/201322068.

Astropy Collaboration, A. M. Price-Whelan, B. M. Sipőcz, H. M. Günther, P. L. Lim, S. M. Crawford, S. Conseil, D. L. Shupe, M. W. Craig, N. Dencheva, A. Ginsburg, J. T. VanderPlas, L. D. Bradley, D. Pérez-Suárez, M. de Val-Borro, T. L. Aldcroft, K. L. Cruz, T. P. Robitaille, E. J. Tollerud, C. Ardelean, T. Babej, Y. P. Bach, M. Bachetti, A. V. Bakanov, S. P. Bamford, G. Barentsen, P. Barmby, A. Baumbach, K. L. Berry, F. Biscani, M. Boquien, K. A. Bostroem, L. G. Bouma, G. B. Brammer, E. M. Bray, H. Breytenbach, H. Buddelmeijer, D. J. Burke, G. Calderone, J. L. Cano Rodríguez, M. Cara, J. V. M. Cardoso, S. Cheedella, Y. Copin, L. Corrales, D. Crichton, D. D'Avella, C. Deil, É. Depagne, J. P. Dietrich, A. Donath, M. Droettboom, N. Earl, T. Erben, S. Fabbro, L. A. Ferreira, T. Finethy, R. T. Fox, L. H. Garrison, S. L. J. Gibbons, D. A. Goldstein, R. Gommers, J. P. Greco, P. Greenfield, A. M. Groener, F. Grollier, A. Hagen, P. Hirst, D. Homeier, A. J. Horton, G. Hosseinzadeh, L. Hu, J. S. Hunkeler, Ž. Ivezić, A. Jain, T. Jenness, G. Kanarek, S. Kendrew, N. S. Kern, W. E. Kerzendorf, A. Khvalko, J. King, D. Kirkby, A. M. Kulkarni, A. Kumar, A. Lee, D. Lenz, S. P. Littlefair, Z. Ma, D. M. Macleod, M. Mastropietro, C. McCully, S. Montagnac, B. M. Morris, M. Mueller, S. J. Mumford, D. Muna, N. A. Murphy, S. Nelson, G. H. Nguyen, J. P. Ninan, M. Nöthe, S. Ogaz, S. Oh, J. K. Parejko, N. Parley, S. Pascual, R. Patil, A. A. Patil, A. L. Plunkett, J. X. Prochaska, T. Rastogi, V. Reddy Janga, J. Sabater, P. Sakurikar, M. Seifert, L. E. Sherbert, H. Sherwood-Taylor, A. Y. Shih, J. Sick, M. T. Silbiger, S. Singanamalla, L. P.

Singer, P. H. Sladen, K. A. Sooley, S. Sornarajah, O. Streicher, P. Teuben, S. W. Thomas, G. R. Tremblay, J. E. H. Turner, V. Terrón, M. H. van Kerkwijk, A. de la Vega, L. L. Watkins, B. A. Weaver, J. B. Whitmore, J. Woillez, V. Zabalza, and Astropy Contributors. The Astropy Project: Building an Open-science Project and Status of the v2.0 Core Package. AJ, 156(3):123, September 2018. doi: 10.3847/1538-3881/aabc4f.

Astropy Collaboration, Adrian M. Price-Whelan, Pey Lian Lim, Nicholas Earl, Nathaniel Starkman, Larry Bradley, David L. Shupe, Aarya A. Patil, Lia Corrales, C. E. Brasseur, Maximilian Nöthe, Axel Donath, Erik Tollerud, Brett M. Morris, Adam Ginsburg, Eero Vaher, Benjamin A. Weaver, James Tocknell, William Jamieson, Marten H. van Kerkwijk, Thomas P. Robitaille, Bruce Merry, Matteo Bachetti, H. Moritz Günther, Thomas L. Aldcroft, Jaime A. Alvarado-Montes, Anne M. Archibald, Attila Bódi, Shreyas Bapat, Geert Barentsen, Juanjo Bazán, Manish Biswas, Médéric Boquien, D. J. Burke, Daria Cara, Mihai Cara, Kyle E. Conroy, Simon Conseil, Matthew W. Craig, Robert M. Cross, Kelle L. Cruz, Francesco D'Eugenio, Nadia Dencheva, Hadrien A. R. Devillepoix, Jörg P. Dietrich, Arthur Davis Eigenbrot, Thomas Erben, Leonardo Ferreira, Daniel Foreman-Mackey, Ryan Fox, Nabil Freij, Suyog Garg, Robel Geda, Lauren Glattly, Yash Gondhalekar, Karl D. Gordon, David Grant, Perry Greenfield, Austen M. Groener, Steve Guest, Sebastian Gurovich, Rasmus Handberg, Akeem Hart, Zac Hatfield-Dodds, Derek Homeier, Griffin Hosseinzadeh, Tim Jenness, Craig K. Jones, Prajwel Joseph, J. Bryce Kalmbach, Emir Karamehmetoglu, Mikołaj Kałuszyński, Michael S. P. Kelley, Nicholas Kern, Wolfgang E. Kerzendorf, Eric W. Koch, Shankar Kulumani, Antony Lee, Chun Ly, Zhiyuan Ma, Conor MacBride, Jakob M. Maljaars, Demitri Muna, N. A. Murphy, Henrik Norman, Richard O'Steen, Kyle A. Oman, Camilla Pacifici, Sergio Pascual, J. Pascual-Granado, Rohit R. Patil, Gabriel I. Perren, Timothy E. Pickering, Tanuj Rastogi, Benjamin R. Roulston, Daniel F. Ryan, Eli S. Rykoff, Jose Sabater, Parikshit Sakurikar, Jesús Salgado, Aniket Sanghi, Nicholas Saunders, Volodymyr Savchenko, Ludwig Schwardt, Michael Seifert-Eckert, Albert Y. Shih, Anany Shrey Jain, Gyanendra Shukla, Jonathan Sick, Chris Simpson, Sudheesh Singanamalla, Leo P. Singer, Jaladh Singhal, Manodeep Sinha, Brigitta M. Sipőcz, Lee R. Spitler, David Stansby, Ole Streicher, Jani Šumak, John D. Swinbank, Dan S. Taranu, Nikita Tewary, Grant R. Tremblay, Miguel de Val-Borro, Samuel J. Van Kooten, Zlatan Vasović, Shresth Verma, José Vinícius de Miranda Cardoso, Peter K. G. Williams, Tom J. Wilson, Benjamin Winkel, W. M. Wood-Vasey, Rui Xue, Peter Yoachim, Chen Zhang, Andrea Zonca, and Astropy Project Contributors. The Astropy Project: Sustaining and Growing a Community-oriented Open-source Project and the Latest Major Release (v5.0) of the Core Package. ApJ, 935(2):167, August 2022. doi: 10.3847/1538-4357/ac7c74.

N. Astudillo-Defru, X. Delfosse, X. Bonfils, T. Forveille, C. Lovis, and J. Rameau. Magnetic activity in the HARPS M dwarf sample. The rotation-activity relationship for very low-mass stars through R'$_{HK}$. A&A, 600:A13, April 2017. doi: 10.1051/0004-6361/201527078.

H. W. Babcock. The Topology of the Sun's Magnetic Field and the 22-Year Cycle. ApJ, 133:572, March 1961. doi: 10.1086/147060.

C. Babusiaux, C. Fabricius, S. Khanna, T. Muraveva, C. Reylé, F. Spoto, A. Vallenari, X. Luri, F. Arenou, M. A. Álvarez, F. Anders, T. Antoja, E. Balbinot, C. Barache,

N. Bauchet, D. Bossini, D. Busonero, T. Cantat-Gaudin, J. M. Carrasco, C. Dafonte, S. Diakité, F. Figueras, A. Garcia-Gutierrez, A. Garofalo, A. Helmi, Ó. Jiménez-Arranz, C. Jordi, P. Kervella, Z. Kostrzewa-Rutkowska, N. Leclerc, E. Licata, M. Manteiga, A. Masip, M. Monguió, P. Ramos, N. Robichon, A. C. Robin, M. Romero-Gómez, A. Sáez, R. Santoveña, L. Spina, G. Torralba Elipe, and M. Weiler. Gaia Data Release 3. Catalogue validation. A&A, 674:A32, June 2023a. doi: 10.1051/0004-6361/202243790.

C. Babusiaux, C. Fabricius, S. Khanna, T. Muraveva, C. Reylé, F. Spoto, A. Vallenari, X. Luri, F. Arenou, M. A. Álvarez, F. Anders, T. Antoja, E. Balbinot, C. Barache, N. Bauchet, D. Bossini, D. Busonero, T. Cantat-Gaudin, J. M. Carrasco, C. Dafonte, S. Diakité, F. Figueras, A. Garcia-Gutierrez, A. Garofalo, A. Helmi, Ó. Jiménez-Arranz, C. Jordi, P. Kervella, Z. Kostrzewa-Rutkowska, N. Leclerc, E. Licata, M. Manteiga, A. Masip, M. Monguió, P. Ramos, N. Robichon, A. C. Robin, M. Romero-Gómez, A. Sáez, R. Santoveña, L. Spina, G. Torralba Elipe, and M. Weiler. Gaia Data Release 3. Catalogue validation. A&A, 674:A32, June 2023b. doi: 10.1051/0004-6361/202243790.

C. A. L. Bailer-Jones, J. Rybizki, M. Fouesneau, M. Demleitner, and R. Andrae. Estimating Distances from Parallaxes. V. Geometric and Photogeometric Distances to 1.47 Billion Stars in Gaia Early Data Release 3. AJ, 161(3):147, March 2021. doi: 10.3847/1538-3881/abd806.

S. L. Baliunas, R. A. Donahue, W. H. Soon, J. H. Horne, J. Frazer, L. Woodard-Eklund, M. Bradford, L. M. Rao, O. C. Wilson, Q. Zhang, W. Bennett, J. Briggs, S. M. Carroll, D. K. Duncan, D. Figueroa, H. H. Lanning, T. Misch, J. Mueller, R. W. Noyes, D. Poppe, A. C. Porter, C. R. Robinson, J. Russell, J. C. Shelton, T. Soyumer, A. H. Vaughan, and J. H. Whitney. Chromospheric Variations in Main-Sequence Stars. II. ApJ, 438:269, January 1995. doi: 10.1086/175072.

J. J. Balmer. Notiz über die Spectrallinien des Wasserstoffs. *Annalen der Physik*, 261(5): 80–87, January 1885. doi: 10.1002/andp.18852610506.

Gibor Basri. *An Introduction to Stellar Magnetic Activity.* 2021. doi: 10.1088/2514-3433/ac2956.

P. G. Beck, C. Allende Prieto, T. Van Reeth, A. Tkachenko, G. Raskin, H. van Winckel, Jr. do Nascimento, J. D., D. Salabert, E. Corsaro, and R. A. García. The HERMES solar atlas and the spectroscopic analysis of the seismic solar analogue KIC 3241581. A&A, 589:A27, May 2016. doi: 10.1051/0004-6361/201425423.

P. G. Beck, Jr. do Nascimento, J. D., T. Duarte, D. Salabert, A. Tkachenko, S. Mathis, S. Mathur, R. A. García, M. Castro, P. L. Pallé, R. Egeland, D. Montes, O. Creevey, M. F. Andersen, D. Kamath, and H. van Winckel. Lithium abundance and rotation of seismic solar analogues. Solar and stellar connection from Kepler and Hermes observations. A&A, 602:A63, June 2017. doi: 10.1051/0004-6361/201629820.

S. Bellotti, D. Evensberget, A. A. Vidotto, A. Lavail, T. Lüftinger, G. A. J. Hussain, J. Morin, P. Petit, S. Boro Saikia, C. Danielski, and G. Micela. Spectropolarimetric characterisation of exoplanet host stars in preparation of the Ariel mission. Magnetic environment of HD 63433. A&A, 688:A63, August 2024. doi: 10.1051/0004-6361/202449581.

J. Bento, J. D. Hartman, G. Á. Bakos, W. Bhatti, Z. Csubry, K. Penev, D. Bayliss, M. de Val-Borro, G. Zhou, R. Brahm, N. Espinoza, M. Rabus, A. Jordán, V. Suc, S. Ciceri, P. Sarkis, T. Henning, L. Mancini, C. G. Tinney, D. J. Wright, S. Durkan, T. G. Tan, J. Lázár, I. Papp, and P. Sári. HATS-39b, HATS-40b, HATS-41b, and HATS-42b: three inflated hot Jupiters and a super-Jupiter transiting F stars. MNRAS, 477(3):3406–3423, July 2018. doi: 10.1093/mnras/sty726.

Arnold O. Benz and Manuel Güdel. Physical Processes in Magnetically Driven Flares on the Sun, Stars, and Young Stellar Objects. ARA&A, 48:241–287, September 2010. doi: 10.1146/annurev-astro-082708-101757.

Svetlana V. Berdyugina. Starspots: A Key to the Stellar Dynamo. *Living Reviews in Solar Physics*, 2(1):8, December 2005. doi: 10.12942/lrsp-2005-8.

Erika Böhm-Vitense. Chromospheric Activity in G and K Main-Sequence Stars, and What It Tells Us about Stellar Dynamos. ApJ, 657(1):486–493, March 2007. doi: 10.1086/510482.

S. Boro Saikia, C. J. Marvin, S. V. Jeffers, A. Reiners, R. Cameron, S. C. Marsden, P. Petit, J. Warnecke, and A. P. Yadav. Chromospheric activity catalogue of 4454 cool stars. Questioning the active branch of stellar activity cycles. A&A, 616:A108, August 2018. doi: 10.1051/0004-6361/201629518.

S. Boro Saikia, T. Lueftinger, V. S. Airapetian, T. Ayres, M. Bartel, M. Guedel, M. Jin, K. G. Kislyakova, and P. Testa. Nonthermal Motions and Atmospheric Heating of Cool Stars. ApJ, 950(2):124, June 2023. doi: 10.3847/1538-4357/acca14.

Emily M. Boudreaux, Elisabeth R. Newton, Nicholas Mondrik, David Charbonneau, and Jonathan Irwin. The Ca II H and K Rotation-Activity Relation in 53 Mid-to-late-type M Dwarfs. ApJ, 929(1):80, April 2022. doi: 10.3847/1538-4357/ac5cbf.

Jo Bovy. galpy: A python Library for Galactic Dynamics. ApJS, 216(2):29, February 2015. doi: 10.1088/0067-0049/216/2/29.

R. Brahm, A. Jordán, G. Á. Bakos, K. Penev, N. Espinoza, M. Rabus, J. D. Hartman, D. Bayliss, S. Ciceri, G. Zhou, L. Mancini, T. G. Tan, M. de Val-Borro, W. Bhatti, Z. Csubry, J. Bento, T. Henning, B. Schmidt, F. Rojas, V. Suc, J. Lázár, I. Papp, and P. Sári. HATS-17b: A Transiting Compact Warm Jupiter in a 16.3 Day Circular Orbit. AJ, 151(4):89, April 2016. doi: 10.3847/0004-6256/151/4/89.

R. Brahm, J. D. Hartman, A. Jordán, G. Á. Bakos, N. Espinoza, M. Rabus, W. Bhatti, K. Penev, P. Sarkis, V. Suc, Z. Csubry, D. Bayliss, J. Bento, G. Zhou, L. Mancini, T. Henning, S. Ciceri, M. de Val-Borro, S. Shectman, J. D. Crane, P. Arriagada, P. Butler, J. Teske, I. Thompson, D. Osip, M. Díaz, B. Schmidt, J. Lázár, I. Papp, and P. Sári. HATS-43b, HATS-44b, HATS-45b, and HATS-46b: Four Short-period Transiting Giant Planets in the Neptune-Jupiter Mass Range. AJ, 155(3):112, March 2018. doi: 10.3847/1538-3881/aaa898.

E. L. Brown, S. V. Jeffers, S. C. Marsden, J. Morin, S. Boro Saikia, P. Petit, M. M. Jardine, V. See, A. A. Vidotto, M. W. Mengel, M. N. Dahlkemper, and the BCool Collaboration.

Linking chromospheric activity and magnetic field properties for late-type dwarf stars. MNRAS, 514(3):4300–4319, August 2022. doi: 10.1093/mnras/stac1291.

Anna Brucalassi, Maria Tsantaki, Laura Magrini, Sergio Sousa, Camilla Danielski, Katia Biazzo, Giada Casali, Mathieu Van der Swaelmen, Monica Rainer, Vardan Adibekyan, Elisa Delgado-Mena, and Nicoletta Sanna. Determination of stellar parameters for Ariel targets: a comparison analysis between different spectroscopic methods. *Experimental Astronomy*, 53(2):511–532, April 2022. doi: 10.1007/s10686-020-09695-4.

Allan Sacha Brun and Matthew K. Browning. Magnetism, dynamo action and the solar-stellar connection. *Living Reviews in Solar Physics*, 14(1):4, December 2017. doi: 10.1007/s41116-017-0007-8.

Mats Carlsson, Bart De Pontieu, and Viggo H. Hansteen. New View of the Solar Chromosphere. ARA&A, 57:189–226, August 2019. doi: 10.1146/annurev-astro-081817-052044.

Paul Charbonneau. Dynamo Models of the Solar Cycle. *Living Reviews in Solar Physics*, 7 (1):3, December 2010. doi: 10.12942/lrsp-2010-3.

C. Cincunegui, R. F. Díaz, and P. J. D. Mauas. Hα and the Ca II H and K lines as activity proxies for late-type stars. A&A, 469(1):309–317, July 2007. doi: 10.1051/0004-6361:20066503.

Rosario Cosentino, Christophe Lovis, Francesco Pepe, Andrew Collier Cameron, David W. Latham, Emilio Molinari, Stephane Udry, Naidu Bezawada, Martin Black, Andy Born, Nicolas Buchschacher, Dave Charbonneau, Pedro Figueira, Michel Fleury, Alberto Galli, Angus Gallie, Xiaofeng Gao, Adriano Ghedina, Carlos Gonzalez, Manuel Gonzalez, Jose Guerra, David Henry, Keith Horne, Ian Hughes, Dennis Kelly, Marcello Lodi, David Lunney, Charles Maire, Michel Mayor, Giusi Micela, Mark P. Ordway, John Peacock, David Phillips, Giampaolo Piotto, Don Pollacco, Didier Queloz, Ken Rice, Carlos Riverol, Luis Riverol, Jose San Juan, Dimitar Sasselov, Damien Segransan, Alessandro Sozzetti, Danuta Sosnowska, Brian Stobie, Andrew Szentgyorgyi, Andy Vick, and Luc Weber. Harps-N: the new planet hunter at TNG. In Ian S. McLean, Suzanne K. Ramsay, and Hideki Takami, editors, *Ground-based and Airborne Instrumentation for Astronomy IV*, volume 8446 of *Society of Photo-Optical Instrumentation Engineers (SPIE) Conference Series*, page 84461V, September 2012. doi: 10.1117/12.925738.

Camilla Danielski, Anna Brucalassi, Serena Benatti, Tiago Campante, Elisa Delgado-Mena, Monica Rainer, Germano Sacco, Vardan Adibekyan, Katia Biazzo, Diego Bossini, Giovanni Bruno, Giada Casali, Petr Kabath, Laura Magrini, Giusi Micela, Giuseppe Morello, Pietro Palladino, Nicoletta Sanna, Subhajit Sarkar, Sérgio Sousa, Maria Tsantaki, Diego Turrini, and Mathieu Van der Swaelmen. The homogeneous characterisation of Ariel host stars. *Experimental Astronomy*, 53(2):473–510, April 2022. doi: 10.1007/s10686-021-09765-1.

Hans Dekker, Sandro D'Odorico, Andreas Kaufer, Bernard Delabre, and Heinz Kotzlowski. Design, construction, and performance of UVES, the echelle spectrograph for the UT2 Kueyen Telescope at the ESO Paranal Observatory. In Masanori Iye and Alan F. Moorwood, editors, *Optical and IR Telescope Instrumentation and Detectors*, volume 4008 of

Society of Photo-Optical Instrumentation Engineers (SPIE) Conference Series, pages 534–545, August 2000. doi: 10.1117/12.395512.

Sandro D'Odorico, Stefano Cristiani, Hans Dekker, Vanessa Hill, Andreas Kaufer, Taesun Kim, and Francesca Primas. Performance of UVES, the echelle spectrograph for the ESO VLT and highlights of the first observations of stars and quasars. In Jacqueline Bergeron, editor, *Discoveries and Research Prospects from 8- to 10-Meter-Class Telescopes*, volume 4005 of *Society of Photo-Optical Instrumentation Engineers (SPIE) Conference Series*, pages 121–130, June 2000. doi: 10.1117/12.390133.

Douglas K. Duncan, Arthur H. Vaughan, Olin C. Wilson, George W. Preston, James Frazer, Howard Lanning, Anthony Misch, Jean Mueller, David Soyumer, L. Woodard, Sallie L. Baliunas, Robert W. Noyes, Lee W. Hartmann, Alain Porter, Cornelis Zwaan, Frans Middelkoop, Rene G. M. Rutten, and Dimitri Mihalas. CA II H and K Measurements Made at Mount Wilson Observatory, 1966–1983. ApJS, 76:383, May 1991. doi: 10.1086/191572.

B. R. Durney, D. Mihalas, and R. D. Robinson. A preliminary interpretation of stellar chromospheric CA II emission variations within the framework of stellar dynamo theory. PASP, 93:537–543, October 1981. doi: 10.1086/130878.

G. Eberhard and K. Schwarzschild. On the reversal of the calcium lines H and K in stellar spectra. ApJ, 38:292–295, October 1913. doi: 10.1086/142037.

Ricky Egeland, Willie Soon, Sallie Baliunas, Jeffrey C. Hall, Alexei A. Pevtsov, and Luca Bertello. The Mount Wilson Observatory S-index of the Sun. ApJ, 835(1):25, January 2017. doi: 10.3847/1538-4357/835/1/25.

Oddbjørn Engvold, Jean-Claude Vial, and Andrew Skumanich. *The Sun as a Guide to Stellar Physics*. 2019. doi: 10.1016/C2017-0-01365-4.

Yuhong Fan. Magnetic Fields in the Solar Convection Zone. *Living Reviews in Solar Physics*, 6(1):4, December 2009. doi: 10.12942/lrsp-2009-4.

R. R. Ferreira, B. F. O. Gonçalves, J. D. do Nascimento, and M. Castro. A correlation between sunspot observations and solar Ca II H&K activity proxies. MNRAS, October 2024. doi: 10.1093/mnras/stae2381.

D. J. Fritzewski, S. A. Barnes, D. J. James, S. P. Järvinen, and K. G. Strassmeier. A detailed understanding of the rotation-activity relationship using the 300 Myr old open cluster NGC 3532. A&A, 656:A103, December 2021. doi: 10.1051/0004-6361/202140896.

Gaia Collaboration, T. Prusti, J. H. J. de Bruijne, A. G. A. Brown, A. Vallenari, C. Babusiaux, C. A. L. Bailer-Jones, U. Bastian, M. Biermann, D. W. Evans, L. Eyer, F. Jansen, C. Jordi, S. A. Klioner, U. Lammers, L. Lindegren, X. Luri, F. Mignard, D. J. Milligan, C. Panem, V. Poinsignon, D. Pourbaix, S. Randich, G. Sarri, P. Sartoretti, H. I. Siddiqui, C. Soubiran, V. Valette, F. van Leeuwen, N. A. Walton, C. Aerts, F. Arenou, M. Cropper, R. Drimmel, E. Høg, D. Katz, M. G. Lattanzi, W. O'Mullane, E. K. Grebel, A. D. Holland, C. Huc, X. Passot, L. Bramante, C. Cacciari, J. Castañeda, L. Chaoul, N. Cheek, F. De Angeli, C. Fabricius, R. Guerra, J. Hernández, A. Jean-Antoine-Piccolo, E. Masana, R. Messineo, N. Mowlavi, K. Nienartowicz, D. Ordóñez-Blanco, P. Panuzzo, J. Portell, P. J.

Richards, M. Riello, G. M. Seabroke, P. Tanga, F. Thévenin, J. Torra, S. G. Els, G. Gracia-Abril, G. Comoretto, M. Garcia-Reinaldos, T. Lock, E. Mercier, M. Altmann, R. Andrae, T. L. Astraatmadja, I. Bellas-Velidis, K. Benson, J. Berthier, R. Blomme, G. Busso, B. Carry, A. Cellino, G. Clementini, S. Cowell, O. Creevey, J. Cuypers, M. Davidson, J. De Ridder, A. de Torres, L. Delchambre, A. Dell'Oro, C. Ducourant, Y. Frémat, M. García-Torres, E. Gosset, J. L. Halbwachs, N. C. Hambly, D. L. Harrison, M. Hauser, D. Hestroffer, S. T. Hodgkin, H. E. Huckle, A. Hutton, G. Jasniewicz, S. Jordan, M. Kontizas, A. J. Korn, A. C. Lanzafame, M. Manteiga, A. Moitinho, K. Muinonen, J. Osinde, E. Pancino, T. Pauwels, J. M. Petit, A. Recio-Blanco, A. C. Robin, L. M. Sarro, C. Siopis, M. Smith, K. W. Smith, A. Sozzetti, W. Thuillot, W. van Reeven, Y. Viala, U. Abbas, A. Abreu Aramburu, S. Accart, J. J. Aguado, P. M. Allan, W. Allasia, G. Altavilla, M. A. Álvarez, J. Alves, R. I. Anderson, A. H. Andrei, E. Anglada Varela, E. Antiche, T. Antoja, S. Antón, B. Arcay, A. Atzei, L. Ayache, N. Bach, S. G. Baker, L. Balaguer-Núñez, C. Barache, C. Barata, A. Barbier, F. Barblan, M. Baroni, D. Barrado y Navascués, M. Barros, M. A. Barstow, U. Becciani, M. Bellazzini, G. Bellei, A. Bello García, V. Belokurov, P. Bendjoya, A. Berihuete, L. Bianchi, O. Bienaymé, F. Billebaud, N. Blagorodnova, S. Blanco-Cuaresma, T. Boch, A. Bombrun, R. Borrachero, S. Bouquillon, G. Bourda, H. Bouy, A. Bragaglia, M. A. Breddels, N. Brouillet, T. Brüsemeister, B. Bucciarelli, F. Budnik, P. Burgess, R. Burgon, A. Burlacu, D. Busonero, R. Buzzi, E. Caffau, J. Cambras, H. Campbell, R. Cancelliere, T. Cantat-Gaudin, T. Carlucci, J. M. Carrasco, M. Castellani, P. Charlot, J. Charnas, P. Charvet, F. Chassat, A. Chiavassa, M. Clotet, G. Cocozza, R. S. Collins, P. Collins, G. Costigan, F. Crifo, N. J. G. Cross, M. Crosta, C. Crowley, C. Dafonte, Y. Damerdji, A. Dapergolas, P. David, M. David, P. De Cat, F. de Felice, P. de Laverny, F. De Luise, R. De March, D. de Martino, R. de Souza, J. Debosscher, E. del Pozo, M. Delbo, A. Delgado, H. E. Delgado, F. di Marco, P. Di Matteo, S. Diakite, E. Distefano, C. Dolding, S. Dos Anjos, P. Drazinos, J. Durán, Y. Dzigan, E. Ecale, B. Edvardsson, H. Enke, M. Erdmann, D. Escolar, M. Espina, N. W. Evans, G. Eynard Bontemps, C. Fabre, M. Fabrizio, S. Faigler, A. J. Falcão, M. Farràs Casas, F. Faye, L. Federici, G. Fedorets, J. Fernández-Hernández, P. Fernique, A. Fienga, F. Figueras, F. Filippi, K. Findeisen, A. Fonti, M. Fouesneau, E. Fraile, M. Fraser, J. Fuchs, R. Furnell, M. Gai, S. Galleti, L. Galluccio, D. Garabato, F. García-Sedano, P. Garé, A. Garofalo, N. Garralda, P. Gavras, J. Gerssen, R. Geyer, G. Gilmore, S. Girona, G. Giuffrida, M. Gomes, A. González-Marcos, J. González-Núñez, J. J. González-Vidal, M. Granvik, A. Guerrier, P. Guillout, J. Guiraud, A. Gúrpide, R. Gutiérrez-Sánchez, L. P. Guy, R. Haigron, D. Hatzidimitriou, M. Haywood, U. Heiter, A. Helmi, D. Hobbs, W. Hofmann, B. Holl, G. Holland, J. A. S. Hunt, A. Hypki, V. Icardi, M. Irwin, G. Jevardat de Fombelle, P. Jofré, P. G. Jonker, A. Jorissen, F. Julbe, A. Karampelas, A. Kochoska, R. Kohley, K. Kolenberg, E. Kontizas, S. E. Koposov, G. Kordopatis, P. Koubsky, A. Kowalczyk, A. Krone-Martins, M. Kudryashova, I. Kull, R. K. Bachchan, F. Lacoste-Seris, A. F. Lanza, J. B. Lavigne, C. Le Poncin-Lafitte, Y. Lebreton, T. Lebzelter, S. Leccia, N. Leclerc, I. Lecoeur-Taibi, V. Lemaitre, H. Lenhardt, F. Leroux, S. Liao, E. Licata, H. E. P. Lindstrøm, T. A. Lister, E. Livanou, A. Lobel, W. Löffler, M. López, A. Lopez-Lozano, D. Lorenz, T. Loureiro, I. MacDonald, T. Magalhães Fernandes, S. Managau, R. G. Mann, G. Mantelet, O. Marchal, J. M. Marchant, M. Marconi, J. Marie, S. Marinoni, P. M. Marrese, G. Marschalkó, D. J. Marshall, J. M. Martín-Fleitas, M. Martino, N. Mary, G. Matijevič, T. Mazeh, P. J.

McMillan, S. Messina, A. Mestre, D. Michalik, N. R. Millar, B. M. H. Miranda, D. Molina, R. Molinaro, M. Molinaro, L. Molnár, M. Moniez, P. Montegriffo, D. Monteiro, R. Mor, A. Mora, R. Morbidelli, T. Morel, S. Morgenthaler, T. Morley, D. Morris, A. F. Mulone, T. Muraveva, I. Musella, J. Narbonne, G. Nelemans, L. Nicastro, L. Noval, C. Ordénovic, J. Ordieres-Meré, P. Osborne, C. Pagani, I. Pagano, F. Pailler, H. Palacin, L. Palaversa, P. Parsons, T. Paulsen, M. Pecoraro, R. Pedrosa, H. Pentikäinen, J. Pereira, B. Pichon, A. M. Piersimoni, F. X. Pineau, E. Plachy, G. Plum, E. Poujoulet, A. Prša, L. Pulone, S. Ragaini, S. Rago, N. Rambaux, M. Ramos-Lerate, P. Ranalli, G. Rauw, A. Read, S. Regibo, F. Renk, C. Reylé, R. A. Ribeiro, L. Rimoldini, V. Ripepi, A. Riva, G. Rixon, M. Roelens, M. Romero-Gómez, N. Rowell, F. Royer, A. Rudolph, L. Ruiz-Dern, G. Sadowski, T. Sagristà Sellés, J. Sahlmann, J. Salgado, E. Salguero, M. Sarasso, H. Savietto, A. Schnorhk, M. Schultheis, E. Sciacca, M. Segol, J. C. Segovia, D. Segransan, E. Serpell, I. C. Shih, R. Smareglia, R. L. Smart, C. Smith, E. Solano, F. Solitro, R. Sordo, S. Soria Nieto, J. Souchay, A. Spagna, F. Spoto, U. Stampa, I. A. Steele, H. Steidelmüller, C. A. Stephenson, H. Stoev, F. F. Suess, M. Süveges, J. Surdej, L. Szabados, E. Szegedi-Elek, D. Tapiador, F. Taris, G. Tauran, M. B. Taylor, R. Teixeira, D. Terrett, B. Tingley, S. C. Trager, C. Turon, A. Ulla, E. Utrilla, G. Valentini, A. van Elteren, E. Van Hemelryck, M. van Leeuwen, M. Varadi, A. Vecchiato, J. Veljanoski, T. Via, D. Vicente, S. Vogt, H. Voss, V. Votruba, S. Voutsinas, G. Walmsley, M. Weiler, K. Weingrill, D. Werner, T. Wevers, G. Whitehead, Ł. Wyrzykowski, A. Yoldas, M. Žerjal, S. Zucker, C. Zurbach, T. Zwitter, A. Alecu, M. Allen, C. Allende Prieto, A. Amorim, G. Anglada-Escudé, V. Arsenijevic, S. Azaz, P. Balm, M. Beck, H. H. Bernstein, L. Bigot, A. Bijaoui, C. Blasco, M. Bonfigli, G. Bono, S. Boudreault, A. Bressan, S. Brown, P. M. Brunet, P. Bunclark, R. Buonanno, A. G. Butkevich, C. Carret, C. Carrion, L. Chemin, F. Chéreau, L. Corcione, E. Darmigny, K. S. de Boer, P. de Teodoro, P. T. de Zeeuw, C. Delle Luche, C. D. Domingues, P. Dubath, F. Fodor, B. Frézouls, A. Fries, D. Fustes, D. Fyfe, E. Gallardo, J. Gallegos, D. Gardiol, M. Gebran, A. Gomboc, A. Gómez, E. Grux, A. Gueguen, A. Heyrovsky, J. Hoar, G. Iannicola, Y. Isasi Parache, A. M. Janotto, E. Joliet, A. Jonckheere, R. Keil, D. W. Kim, P. Klagyivik, J. Klar, J. Knude, O. Kochukhov, I. Kolka, J. Kos, A. Kutka, V. Lainey, D. LeBouquin, C. Liu, D. Loreggia, V. V. Makarov, M. G. Marseille, C. Martayan, O. Martinez-Rubi, B. Massart, F. Meynadier, S. Mignot, U. Munari, A. T. Nguyen, T. Nordlander, P. Ocvirk, K. S. O'Flaherty, A. Olias Sanz, P. Ortiz, J. Osorio, D. Oszkiewicz, A. Ouzounis, M. Palmer, P. Park, E. Pasquato, C. Peltzer, J. Peralta, F. Péturaud, T. Pieniluoma, E. Pigozzi, J. Poels, G. Prat, T. Prod'homme, F. Raison, J. M. Rebordao, D. Risquez, B. Rocca-Volmerange, S. Rosen, M. I. Ruiz-Fuertes, F. Russo, S. Sembay, I. Serraller Vizcaino, A. Short, A. Siebert, H. Silva, D. Sinachopoulos, E. Slezak, M. Soffel, D. Sosnowska, V. Straižys, M. ter Linden, D. Terrell, S. Theil, C. Tiede, L. Troisi, P. Tsalmantza, D. Tur, M. Vaccari, F. Vachier, P. Valles, W. Van Hamme, L. Veltz, J. Virtanen, J. M. Wallut, R. Wichmann, M. I. Wilkinson, H. Ziaeepour, and S. Zschocke. The Gaia mission. A&A, 595:A1, November 2016a. doi: 10.1051/0004-6361/201629272.

Gaia Collaboration, T. Prusti, J. H. J. de Bruijne, A. G. A. Brown, A. Vallenari, C. Babusiaux, C. A. L. Bailer-Jones, U. Bastian, M. Biermann, D. W. Evans, L. Eyer, F. Jansen, C. Jordi, S. A. Klioner, U. Lammers, L. Lindegren, X. Luri, F. Mignard, D. J. Milligan, C. Panem, V. Poinsignon, D. Pourbaix, S. Randich, G. Sarri, P. Sartoretti, H. I. Siddiqui, C. Soubiran, V. Valette, F. van Leeuwen, N. A. Walton, C. Aerts, F. Arenou, M. Cropper,

R. Drimmel, E. Høg, D. Katz, M. G. Lattanzi, W. O'Mullane, E. K. Grebel, A. D. Holland, C. Huc, X. Passot, L. Bramante, C. Cacciari, J. Castañeda, L. Chaoul, N. Cheek, F. De Angeli, C. Fabricius, R. Guerra, J. Hernández, A. Jean-Antoine-Piccolo, E. Masana, R. Messineo, N. Mowlavi, K. Nienartowicz, D. Ordóñez-Blanco, P. Panuzzo, J. Portell, P. J. Richards, M. Riello, G. M. Seabroke, P. Tanga, F. Thévenin, J. Torra, S. G. Els, G. Gracia-Abril, G. Comoretto, M. Garcia-Reinaldos, T. Lock, E. Mercier, M. Altmann, R. Andrae, T. L. Astraatmadja, I. Bellas-Velidis, K. Benson, J. Berthier, R. Blomme, G. Busso, B. Carry, A. Cellino, G. Clementini, S. Cowell, O. Creevey, J. Cuypers, M. Davidson, J. De Ridder, A. de Torres, L. Delchambre, A. Dell'Oro, C. Ducourant, Y. Frémat, M. García-Torres, E. Gosset, J. L. Halbwachs, N. C. Hambly, D. L. Harrison, M. Hauser, D. Hestroffer, S. T. Hodgkin, H. E. Huckle, A. Hutton, G. Jasniewicz, S. Jordan, M. Kontizas, A. J. Korn, A. C. Lanzafame, M. Manteiga, A. Moitinho, K. Muinonen, J. Osinde, E. Pancino, T. Pauwels, J. M. Petit, A. Recio-Blanco, A. C. Robin, L. M. Sarro, C. Siopis, M. Smith, K. W. Smith, A. Sozzetti, W. Thuillot, W. van Reeven, Y. Viala, U. Abbas, A. Abreu Aramburu, S. Accart, J. J. Aguado, P. M. Allan, W. Allasia, G. Altavilla, M. A. Álvarez, J. Alves, R. I. Anderson, A. H. Andrei, E. Anglada Varela, E. Antiche, T. Antoja, S. Antón, B. Arcay, A. Atzei, L. Ayache, N. Bach, S. G. Baker, L. Balaguer-Núñez, C. Barache, C. Barata, A. Barbier, F. Barblan, M. Baroni, D. Barrado y Navascués, M. Barros, M. A. Barstow, U. Becciani, M. Bellazzini, G. Bellei, A. Bello García, V. Belokurov, P. Bendjoya, A. Berihuete, L. Bianchi, O. Bienaymé, F. Billebaud, N. Blagorodnova, S. Blanco-Cuaresma, T. Boch, A. Bombrun, R. Borrachero, S. Bouquillon, G. Bourda, H. Bouy, A. Bragaglia, M. A. Breddels, N. Brouillet, T. Brüsemeister, B. Bucciarelli, F. Budnik, P. Burgess, R. Burgon, A. Burlacu, D. Busonero, R. Buzzi, E. Caffau, J. Cambras, H. Campbell, R. Cancelliere, T. Cantat-Gaudin, T. Carlucci, J. M. Carrasco, M. Castellani, P. Charlot, J. Charnas, P. Charvet, F. Chassat, A. Chiavassa, M. Clotet, G. Cocozza, R. S. Collins, P. Collins, G. Costigan, F. Crifo, N. J. G. Cross, M. Crosta, C. Crowley, C. Dafonte, Y. Damerdji, A. Dapergolas, P. David, M. David, P. De Cat, F. de Felice, P. de Laverny, F. De Luise, R. De March, D. de Martino, R. de Souza, J. Debosscher, E. del Pozo, M. Delbo, A. Delgado, H. E. Delgado, F. di Marco, P. Di Matteo, S. Diakite, E. Distefano, C. Dolding, S. Dos Anjos, P. Drazinos, J. Durán, Y. Dzigan, E. Ecale, B. Edvardsson, H. Enke, M. Erdmann, D. Escolar, M. Espina, N. W. Evans, G. Eynard Bontemps, C. Fabre, M. Fabrizio, S. Faigler, A. J. Falcão, M. Farràs Casas, F. Faye, L. Federici, G. Fedorets, J. Fernández-Hernández, P. Fernique, A. Fienga, F. Figueras, F. Filippi, K. Findeisen, A. Fonti, M. Fouesneau, E. Fraile, M. Fraser, J. Fuchs, R. Furnell, M. Gai, S. Galleti, L. Galluccio, D. Garabato, F. García-Sedano, P. Garé, A. Garofalo, N. Garralda, P. Gavras, J. Gerssen, R. Geyer, G. Gilmore, S. Girona, G. Giuffrida, M. Gomes, A. González-Marcos, J. González-Núñez, J. J. González-Vidal, M. Granvik, A. Guerrier, P. Guillout, J. Guiraud, A. Gúrpide, R. Gutiérrez-Sánchez, L. P. Guy, R. Haigron, D. Hatzidimitriou, M. Haywood, U. Heiter, A. Helmi, D. Hobbs, W. Hofmann, B. Holl, G. Holland, J. A. S. Hunt, A. Hypki, V. Icardi, M. Irwin, G. Jevardat de Fombelle, P. Jofré, P. G. Jonker, A. Jorissen, F. Julbe, A. Karampelas, A. Kochoska, R. Kohley, K. Kolenberg, E. Kontizas, S. E. Koposov, G. Kordopatis, P. Koubsky, A. Kowalczyk, A. Krone-Martins, M. Kudryashova, I. Kull, R. K. Bachchan, F. Lacoste-Seris, A. F. Lanza, J. B. Lavigne, C. Le Poncin-Lafitte, Y. Lebreton, T. Lebzelter, S. Leccia, N. Leclerc, I. Lecoeur-Taibi, V. Lemaitre, H. Lenhardt, F. Leroux, S. Liao, E. Licata, H. E. P. Lindstrøm, T. A. Lister,

E. Livanou, A. Lobel, W. Löffler, M. López, A. Lopez-Lozano, D. Lorenz, T. Loureiro, I. MacDonald, T. Magalhães Fernandes, S. Managau, R. G. Mann, G. Mantelet, O. Marchal, J. M. Marchant, M. Marconi, J. Marie, S. Marinoni, P. M. Marrese, G. Marschalkó, D. J. Marshall, J. M. Martín-Fleitas, M. Martino, N. Mary, G. Matijevič, T. Mazeh, P. J. McMillan, S. Messina, A. Mestre, D. Michalik, N. R. Millar, B. M. H. Miranda, D. Molina, R. Molinaro, M. Molinaro, L. Molnár, M. Moniez, P. Montegriffo, D. Monteiro, R. Mor, A. Mora, R. Morbidelli, T. Morel, S. Morgenthaler, T. Morley, D. Morris, A. F. Mulone, T. Muraveva, I. Musella, J. Narbonne, G. Nelemans, L. Nicastro, L. Noval, C. Ordénovic, J. Ordieres-Meré, P. Osborne, C. Pagani, I. Pagano, F. Pailler, H. Palacin, L. Palaversa, P. Parsons, T. Paulsen, M. Pecoraro, R. Pedrosa, H. Pentikäinen, J. Pereira, B. Pichon, A. M. Piersimoni, F. X. Pineau, E. Plachy, G. Plum, E. Poujoulet, A. Prša, L. Pulone, S. Ragaini, S. Rago, N. Rambaux, M. Ramos-Lerate, P. Ranalli, G. Rauw, A. Read, S. Regibo, F. Renk, C. Reylé, R. A. Ribeiro, L. Rimoldini, V. Ripepi, A. Riva, G. Rixon, M. Roelens, M. Romero-Gómez, N. Rowell, F. Royer, A. Rudolph, L. Ruiz-Dern, G. Sadowski, T. Sagristà Sellés, J. Sahlmann, J. Salgado, E. Salguero, M. Sarasso, H. Savietto, A. Schnorhk, M. Schultheis, E. Sciacca, M. Segol, J. C. Segovia, D. Segransan, E. Serpell, I. C. Shih, R. Smareglia, R. L. Smart, C. Smith, E. Solano, F. Solitro, R. Sordo, S. Soria Nieto, J. Souchay, A. Spagna, F. Spoto, U. Stampa, I. A. Steele, H. Steidelmüller, C. A. Stephenson, H. Stoev, F. F. Suess, M. Süveges, J. Surdej, L. Szabados, E. Szegedi-Elek, D. Tapiador, F. Taris, G. Tauran, M. B. Taylor, R. Teixeira, D. Terrett, B. Tingley, S. C. Trager, C. Turon, A. Ulla, E. Utrilla, G. Valentini, A. van Elteren, E. Van Hemelryck, M. van Leeuwen, M. Varadi, A. Vecchiato, J. Veljanoski, T. Via, D. Vicente, S. Vogt, H. Voss, V. Votruba, S. Voutsinas, G. Walmsley, M. Weiler, K. Weingrill, D. Werner, T. Wevers, G. Whitehead, Ł. Wyrzykowski, A. Yoldas, M. Žerjal, S. Zucker, C. Zurbach, T. Zwitter, A. Alecu, M. Allen, C. Allende Prieto, A. Amorim, G. Anglada-Escudé, V. Arsenijevic, S. Azaz, P. Balm, M. Beck, H. H. Bernstein, L. Bigot, A. Bijaoui, C. Blasco, M. Bonfigli, G. Bono, S. Boudreault, A. Bressan, S. Brown, P. M. Brunet, P. Bunclark, R. Buonanno, A. G. Butkevich, C. Carret, C. Carrion, L. Chemin, F. Chéreau, L. Corcione, E. Darmigny, K. S. de Boer, P. de Teodoro, P. T. de Zeeuw, C. Delle Luche, C. D. Domingues, P. Dubath, F. Fodor, B. Frézouls, A. Fries, D. Fustes, D. Fyfe, E. Gallardo, J. Gallegos, D. Gardiol, M. Gebran, A. Gomboc, A. Gómez, E. Grux, A. Gueguen, A. Heyrovsky, J. Hoar, G. Iannicola, Y. Isasi Parache, A. M. Janotto, E. Joliet, A. Jonckheere, R. Keil, D. W. Kim, P. Klagyivik, J. Klar, J. Knude, O. Kochukhov, I. Kolka, J. Kos, A. Kutka, V. Lainey, D. LeBouquin, C. Liu, D. Loreggia, V. V. Makarov, M. G. Marseille, C. Martayan, O. Martinez-Rubi, B. Massart, F. Meynadier, S. Mignot, U. Munari, A. T. Nguyen, T. Nordlander, P. Ocvirk, K. S. O'Flaherty, A. Olias Sanz, P. Ortiz, J. Osorio, D. Oszkiewicz, A. Ouzounis, M. Palmer, P. Park, E. Pasquato, C. Peltzer, J. Peralta, F. Péturaud, T. Pieniluoma, E. Pigozzi, J. Poels, G. Prat, T. Prod'homme, F. Raison, J. M. Rebordao, D. Risquez, B. Rocca-Volmerange, S. Rosen, M. I. Ruiz-Fuertes, F. Russo, S. Sembay, I. Serraller Vizcaino, A. Short, A. Siebert, H. Silva, D. Sinachopoulos, E. Slezak, M. Soffel, D. Sosnowska, V. Straižys, M. ter Linden, D. Terrell, S. Theil, C. Tiede, L. Troisi, P. Tsalmantza, D. Tur, M. Vaccari, F. Vachier, P. Valles, W. Van Hamme, L. Veltz, J. Virtanen, J. M. Wallut, R. Wichmann, M. I. Wilkinson, H. Ziaeepour, and S. Zschocke. The Gaia mission. A&A, 595:A1, November 2016b. doi: 10.1051/0004-6361/201629272.

Gaia Collaboration, A. Vallenari, A. G. A. Brown, T. Prusti, J. H. J. de Bruijne, F. Arenou, C. Babusiaux, M. Biermann, O. L. Creevey, C. Ducourant, D. W. Evans, L. Eyer, R. Guerra, A. Hutton, C. Jordi, S. A. Klioner, U. L. Lammers, L. Lindegren, X. Luri, F. Mignard, C. Panem, D. Pourbaix, S. Randich, P. Sartoretti, C. Soubiran, P. Tanga, N. A. Walton, C. A. L. Bailer-Jones, U. Bastian, R. Drimmel, F. Jansen, D. Katz, M. G. Lattanzi, F. van Leeuwen, J. Bakker, C. Cacciari, J. Castañeda, F. De Angeli, C. Fabricius, M. Fouesneau, Y. Frémat, L. Galluccio, A. Guerrier, U. Heiter, E. Masana, R. Messineo, N. Mowlavi, C. Nicolas, K. Nienartowicz, F. Pailler, P. Panuzzo, F. Riclet, W. Roux, G. M. Seabroke, R. Sordo, F. Thévenin, G. Gracia-Abril, J. Portell, D. Teyssier, M. Altmann, R. Andrae, M. Audard, I. Bellas-Velidis, K. Benson, J. Berthier, R. Blomme, P. W. Burgess, D. Busonero, G. Busso, H. Cánovas, B. Carry, A. Cellino, N. Cheek, G. Clementini, Y. Damerdji, M. Davidson, P. de Teodoro, M. Nuñez Campos, L. Delchambre, A. Dell'Oro, P. Esquej, J. Fernández-Hernández, E. Fraile, D. Garabato, P. García-Lario, E. Gosset, R. Haigron, J. L. Halbwachs, N. C. Hambly, D. L. Harrison, J. Hernández, D. Hestroffer, S. T. Hodgkin, B. Holl, K. Janßen, G. Jevardat de Fombelle, S. Jordan, A. Krone-Martins, A. C. Lanzafame, W. Löffler, O. Marchal, P. M. Marrese, A. Moitinho, K. Muinonen, P. Osborne, E. Pancino, T. Pauwels, A. Recio-Blanco, C. Reylé, M. Riello, L. Rimoldini, T. Roegiers, J. Rybizki, L. M. Sarro, C. Siopis, M. Smith, A. Sozzetti, E. Utrilla, M. van Leeuwen, U. Abbas, P. Ábrahám, A. Abreu Aramburu, C. Aerts, J. J. Aguado, M. Ajaj, F. Aldea-Montero, G. Altavilla, M. A. Álvarez, J. Alves, F. Anders, R. I. Anderson, E. Anglada Varela, T. Antoja, D. Baines, S. G. Baker, L. Balaguer-Núñez, E. Balbinot, Z. Balog, C. Barache, D. Barbato, M. Barros, M. A. Barstow, S. Bartolomé, J. L. Bassilana, N. Bauchet, U. Becciani, M. Bellazzini, A. Berihuete, M. Bernet, S. Bertone, L. Bianchi, A. Binnenfeld, S. Blanco-Cuaresma, A. Blazere, T. Boch, A. Bombrun, D. Bossini, S. Bouquillon, A. Bragaglia, L. Bramante, E. Breedt, A. Bressan, N. Brouillet, E. Brugaletta, B. Bucciarelli, A. Burlacu, A. G. Butkevich, R. Buzzi, E. Caffau, R. Cancelliere, T. Cantat-Gaudin, R. Carballo, T. Carlucci, M. I. Carnerero, J. M. Carrasco, L. Casamiquela, M. Castellani, A. Castro-Ginard, L. Chaoul, P. Charlot, L. Chemin, V. Chiaramida, A. Chiavassa, N. Chornay, G. Comoretto, G. Contursi, W. J. Cooper, T. Cornez, S. Cowell, F. Crifo, M. Cropper, M. Crosta, C. Crowley, C. Dafonte, A. Dapergolas, M. David, P. David, P. de Laverny, F. De Luise, R. De March, J. De Ridder, R. de Souza, A. de Torres, E. F. del Peloso, E. del Pozo, M. Delbo, A. Delgado, J. B. Delisle, C. Demouchy, T. E. Dharmawardena, P. Di Matteo, S. Diakite, C. Diener, E. Distefano, C. Dolding, B. Edvardsson, H. Enke, C. Fabre, M. Fabrizio, S. Faigler, G. Fedorets, P. Fernique, A. Fienga, F. Figueras, Y. Fournier, C. Fouron, F. Fragkoudi, M. Gai, A. Garcia-Gutierrez, M. Garcia-Reinaldos, M. García-Torres, A. Garofalo, A. Gavel, P. Gavras, E. Gerlach, R. Geyer, P. Giacobbe, G. Gilmore, S. Girona, G. Giuffrida, R. Gomel, A. Gomez, J. González-Núñez, I. González-Santamaría, J. J. González-Vidal, M. Granvik, P. Guillout, J. Guiraud, R. Gutiérrez-Sánchez, L. P. Guy, D. Hatzidimitriou, M. Hauser, M. Haywood, A. Helmer, A. Helmi, M. H. Sarmiento, S. L. Hidalgo, T. Hilger, N. Hładczuk, D. Hobbs, G. Holland, H. E. Huckle, K. Jardine, G. Jasniewicz, A. Jean-Antoine Piccolo, Ó. Jiménez-Arranz, A. Jorissen, J. Juaristi Campillo, F. Julbe, L. Karbevska, P. Kervella, S. Khanna, M. Kontizas, G. Kordopatis, A. J. Korn, Á. Kóspál, Z. Kostrzewa-Rutkowska, K. Kruszyńska, M. Kun, P. Laizeau, S. Lambert, A. F. Lanza, Y. Lasne, J. F. Le Campion, Y. Lebreton, T. Lebzelter, S. Leccia, N. Leclerc, I. Lecoeur-Taibi, S. Liao, E. L. Licata, H. E. P. Lindstrøm, T. A. Lister, E. Livanou,

A. Lobel, A. Lorca, C. Loup, P. Madrero Pardo, A. Magdaleno Romeo, S. Managau, R. G. Mann, M. Manteiga, J. M. Marchant, M. Marconi, J. Marcos, M. M. S. Marcos Santos, D. Marín Pina, S. Marinoni, F. Marocco, D. J. Marshall, L. Martin Polo, J. M. Martín-Fleitas, G. Marton, N. Mary, A. Masip, D. Massari, A. Mastrobuono-Battisti, T. Mazeh, P. J. McMillan, S. Messina, D. Michalik, N. R. Millar, A. Mints, D. Molina, R. Molinaro, L. Molnár, G. Monari, M. Monguió, P. Montegriffo, A. Montero, R. Mor, A. Mora, R. Morbidelli, T. Morel, D. Morris, T. Muraveva, C. P. Murphy, I. Musella, Z. Nagy, L. Noval, F. Ocaña, A. Ogden, C. Ordenovic, J. O. Osinde, C. Pagani, I. Pagano, L. Palaversa, P. A. Palicio, L. Pallas-Quintela, A. Panahi, S. Payne-Wardenaar, X. Peñalosa Esteller, A. Penttilä, B. Pichon, A. M. Piersimoni, F. X. Pineau, E. Plachy, G. Plum, E. Poggio, A. Prša, L. Pulone, E. Racero, S. Ragaini, M. Rainer, C. M. Raiteri, N. Rambaux, P. Ramos, M. Ramos-Lerate, P. Re Fiorentin, S. Regibo, P. J. Richards, C. Rios Diaz, V. Ripepi, A. Riva, H. W. Rix, G. Rixon, N. Robichon, A. C. Robin, C. Robin, M. Roelens, H. R. O. Rogues, L. Rohrbasser, M. Romero-Gómez, N. Rowell, F. Royer, D. Ruz Mieres, K. A. Rybicki, G. Sadowski, A. Sáez Núñez, A. Sagristà Sellés, J. Sahlmann, E. Salguero, N. Samaras, V. Sanchez Gimenez, N. Sanna, R. Santoveña, M. Sarasso, M. Schultheis, E. Sciacca, M. Segol, J. C. Segovia, D. Ségransan, D. Semeux, S. Shahaf, H. I. Siddiqui, A. Siebert, L. Siltala, A. Silvelo, E. Slezak, I. Slezak, R. L. Smart, O. N. Snaith, E. Solano, F. Solitro, D. Souami, J. Souchay, A. Spagna, L. Spina, F. Spoto, I. A. Steele, H. Steidelmüller, C. A. Stephenson, M. Süveges, J. Surdej, L. Szabados, E. Szegedi-Elek, F. Taris, M. B. Taylor, R. Teixeira, L. Tolomei, N. Tonello, F. Torra, J. Torra, G. Torralba Elipe, M. Trabucchi, A. T. Tsounis, C. Turon, A. Ulla, N. Unger, M. V. Vaillant, E. van Dillen, W. van Reeven, O. Vanel, A. Vecchiato, Y. Viala, D. Vicente, S. Voutsinas, M. Weiler, T. Wevers, Ł. Wyrzykowski, A. Yoldas, P. Yvard, H. Zhao, J. Zorec, S. Zucker, and T. Zwitter. Gaia Data Release 3. Summary of the content and survey properties. A&A, 674:A1, June 2023a. doi: 10.1051/0004-6361/202243940.

Gaia Collaboration, A. Vallenari, A. G. A. Brown, T. Prusti, J. H. J. de Bruijne, F. Arenou, C. Babusiaux, M. Biermann, O. L. Creevey, C. Ducourant, D. W. Evans, L. Eyer, R. Guerra, A. Hutton, C. Jordi, S. A. Klioner, U. L. Lammers, L. Lindegren, X. Luri, F. Mignard, C. Panem, D. Pourbaix, S. Randich, P. Sartoretti, C. Soubiran, P. Tanga, N. A. Walton, C. A. L. Bailer-Jones, U. Bastian, R. Drimmel, F. Jansen, D. Katz, M. G. Lattanzi, F. van Leeuwen, J. Bakker, C. Cacciari, J. Castañeda, F. De Angeli, C. Fabricius, M. Fouesneau, Y. Frémat, L. Galluccio, A. Guerrier, U. Heiter, E. Masana, R. Messineo, N. Mowlavi, C. Nicolas, K. Nienartowicz, F. Pailler, P. Panuzzo, F. Riclet, W. Roux, G. M. Seabroke, R. Sordo, F. Thévenin, G. Gracia-Abril, J. Portell, D. Teyssier, M. Altmann, R. Andrae, M. Audard, I. Bellas-Velidis, K. Benson, J. Berthier, R. Blomme, P. W. Burgess, D. Busonero, G. Busso, H. Cánovas, B. Carry, A. Cellino, N. Cheek, G. Clementini, Y. Damerdji, M. Davidson, P. de Teodoro, M. Nuñez Campos, L. Delchambre, A. Dell'Oro, P. Esquej, J. Fernández-Hernández, E. Fraile, D. Garabato, P. García-Lario, E. Gosset, R. Haigron, J. L. Halbwachs, N. C. Hambly, D. L. Harrison, J. Hernández, D. Hestroffer, S. T. Hodgkin, B. Holl, K. Janßen, G. Jevardat de Fombelle, S. Jordan, A. Krone-Martins, A. C. Lanzafame, W. Löffler, O. Marchal, P. M. Marrese, A. Moitinho, K. Muinonen, P. Osborne, E. Pancino, T. Pauwels, A. Recio-Blanco, C. Reylé, M. Riello, L. Rimoldini, T. Roegiers, J. Rybizki, L. M. Sarro, C. Siopis, M. Smith, A. Sozzetti, E. Utrilla, M. van Leeuwen, U. Abbas, P. Ábrahám, A. Abreu Aramburu, C. Aerts, J. J.

Aguado, M. Ajaj, F. Aldea-Montero, G. Altavilla, M. A. Álvarez, J. Alves, F. Anders, R. I. Anderson, E. Anglada Varela, T. Antoja, D. Baines, S. G. Baker, L. Balaguer-Núñez, E. Balbinot, Z. Balog, C. Barache, D. Barbato, M. Barros, M. A. Barstow, S. Bartolomé, J. L. Bassilana, N. Bauchet, U. Becciani, M. Bellazzini, A. Berihuete, M. Bernet, S. Bertone, L. Bianchi, A. Binnenfeld, S. Blanco-Cuaresma, A. Blazere, T. Boch, A. Bombrun, D. Bossini, S. Bouquillon, A. Bragaglia, L. Bramante, E. Breedt, A. Bressan, N. Brouillet, E. Brugaletta, B. Bucciarelli, A. Burlacu, A. G. Butkevich, R. Buzzi, E. Caffau, R. Cancelliere, T. Cantat-Gaudin, R. Carballo, T. Carlucci, M. I. Carnerero, J. M. Carrasco, L. Casamiquela, M. Castellani, A. Castro-Ginard, L. Chaoul, P. Charlot, L. Chemin, V. Chiaramida, A. Chiavassa, N. Chornay, G. Comoretto, G. Contursi, W. J. Cooper, T. Cornez, S. Cowell, F. Crifo, M. Cropper, M. Crosta, C. Crowley, C. Dafonte, A. Dapergolas, M. David, P. David, P. de Laverny, F. De Luise, R. De March, J. De Ridder, R. de Souza, A. de Torres, E. F. del Peloso, E. del Pozo, M. Delbo, A. Delgado, J. B. Delisle, C. Demouchy, T. E. Dharmawardena, P. Di Matteo, S. Diakite, C. Diener, E. Distefano, C. Dolding, B. Edvardsson, H. Enke, C. Fabre, M. Fabrizio, S. Faigler, G. Fedorets, P. Fernique, A. Fienga, F. Figueras, Y. Fournier, C. Fouron, F. Fragkoudi, M. Gai, A. Garcia-Gutierrez, M. Garcia-Reinaldos, M. García-Torres, A. Garofalo, A. Gavel, P. Gavras, E. Gerlach, R. Geyer, P. Giacobbe, G. Gilmore, S. Girona, G. Giuffrida, R. Gomel, A. Gomez, J. González-Núñez, I. González-Santamaría, J. J. González-Vidal, M. Granvik, P. Guillout, J. Guiraud, R. Gutiérrez-Sánchez, L. P. Guy, D. Hatzidimitriou, M. Hauser, M. Haywood, A. Helmer, A. Helmi, M. H. Sarmiento, S. L. Hidalgo, T. Hilger, N. Hładczuk, D. Hobbs, G. Holland, H. E. Huckle, K. Jardine, G. Jasniewicz, A. Jean-Antoine Piccolo, Ó. Jiménez-Arranz, A. Jorissen, J. Juaristi Campillo, F. Julbe, L. Karbevska, P. Kervella, S. Khanna, M. Kontizas, G. Kordopatis, A. J. Korn, Á. Kóspál, Z. Kostrzewa-Rutkowska, K. Kruszyńska, M. Kun, P. Laizeau, S. Lambert, A. F. Lanza, Y. Lasne, J. F. Le Campion, Y. Lebreton, T. Lebzelter, S. Leccia, N. Leclerc, I. Lecoeur-Taibi, S. Liao, E. L. Licata, H. E. P. Lindstrøm, T. A. Lister, E. Livanou, A. Lobel, A. Lorca, C. Loup, P. Madrero Pardo, A. Magdaleno Romeo, S. Managau, R. G. Mann, M. Manteiga, J. M. Marchant, M. Marconi, J. Marcos, M. M. S. Marcos Santos, D. Marín Pina, S. Marinoni, F. Marocco, D. J. Marshall, L. Martin Polo, J. M. Martín-Fleitas, G. Marton, N. Mary, A. Masip, D. Massari, A. Mastrobuono-Battisti, T. Mazeh, P. J. McMillan, S. Messina, D. Michalik, N. R. Millar, A. Mints, D. Molina, R. Molinaro, L. Molnár, G. Monari, M. Monguió, P. Montegriffo, A. Montero, R. Mor, A. Mora, R. Morbidelli, T. Morel, D. Morris, T. Muraveva, C. P. Murphy, I. Musella, Z. Nagy, L. Noval, F. Ocaña, A. Ogden, C. Ordenovic, J. O. Osinde, C. Pagani, I. Pagano, L. Palaversa, P. A. Palicio, L. Pallas-Quintela, A. Panahi, S. Payne-Wardenaar, X. Peñalosa Esteller, A. Penttilä, B. Pichon, A. M. Piersimoni, F. X. Pineau, E. Plachy, G. Plum, E. Poggio, A. Prša, L. Pulone, E. Racero, S. Ragaini, M. Rainer, C. M. Raiteri, N. Rambaux, P. Ramos, M. Ramos-Lerate, P. Re Fiorentin, S. Regibo, P. J. Richards, C. Rios Diaz, V. Ripepi, A. Riva, H. W. Rix, G. Rixon, N. Robichon, A. C. Robin, C. Robin, M. Roelens, H. R. O. Rogues, L. Rohrbasser, M. Romero-Gómez, N. Rowell, F. Royer, D. Ruz Mieres, K. A. Rybicki, G. Sadowski, A. Sáez Núñez, A. Sagristà Sellés, J. Sahlmann, E. Salguero, N. Samaras, V. Sanchez Gimenez, N. Sanna, R. Santoveña, M. Sarasso, M. Schultheis, E. Sciacca, M. Segol, J. C. Segovia, D. Ségransan, D. Semeux, S. Shahaf, H. I. Siddiqui, A. Siebert, L. Siltala, A. Silvelo, E. Slezak, I. Slezak, R. L. Smart, O. N. Snaith, E. Solano,

F. Solitro, D. Souami, J. Souchay, A. Spagna, L. Spina, F. Spoto, I. A. Steele, H. Steidelmüller, C. A. Stephenson, M. Süveges, J. Surdej, L. Szabados, E. Szegedi-Elek, F. Taris, M. B. Taylor, R. Teixeira, L. Tolomei, N. Tonello, F. Torra, J. Torra, G. Torralba Elipe, M. Trabucchi, A. T. Tsounis, C. Turon, A. Ulla, N. Unger, M. V. Vaillant, E. van Dillen, W. van Reeven, O. Vanel, A. Vecchiato, Y. Viala, D. Vicente, S. Voutsinas, M. Weiler, T. Wevers, Ł. Wyrzykowski, A. Yoldas, P. Yvard, H. Zhao, J. Zorec, S. Zucker, and T. Zwitter. Gaia Data Release 3. Summary of the content and survey properties. A&A, 674:A1, June 2023b. doi: 10.1051/0004-6361/202243940.

A. Gil and K. Mursula. Hale cycle and long-term trend in variation of galactic cosmic rays related to solar rotation. A&A, 599:A112, March 2017. doi: 10.1051/0004-6361/201629604.

J. Gomes da Silva, N. C. Santos, and X. Bonfils. Long-term Stellar Activity Variations of Stars from the HARPS M-dwarf Sample: Comparison Between Activity Indices. In Christopher Johns-Krull, Matthew K. Browning, and Andrew A. West, editors, *16th Cambridge Workshop on Cool Stars, Stellar Systems, and the Sun*, volume 448 of *Astronomical Society of the Pacific Conference Series*, page 1117, December 2011a. doi: 10.48550/arXiv.1012.3640.

J. Gomes da Silva, N. C. Santos, and X. Bonfils. Long-term Stellar Activity Variations of Stars from the HARPS M-dwarf Sample: Comparison Between Activity Indices. In Christopher Johns-Krull, Matthew K. Browning, and Andrew A. West, editors, *16th Cambridge Workshop on Cool Stars, Stellar Systems, and the Sun*, volume 448 of *Astronomical Society of the Pacific Conference Series*, page 1117, December 2011b. doi: 10.48550/arXiv.1012.3640.

J. Gomes da Silva, N. C. Santos, V. Adibekyan, S. G. Sousa, T. L. Campante, P. Figueira, D. Bossini, E. Delgado-Mena, M. J. P. F. G. Monteiro, P. de Laverny, A. Recio-Blanco, and C. Lovis. Stellar chromospheric activity of 1674 FGK stars from the AMBRE-HARPS sample. I. A catalogue of homogeneous chromospheric activity. A&A, 646:A77, February 2021. doi: 10.1051/0004-6361/202039765.

David F. Gray. *The Observation and Analysis of Stellar Photospheres*. 2008.

R. O. Gray, M. G. Napier, and L. I. Winkler. The Physical Basis of Luminosity Classification in the Late A-, F-, and Early G-Type Stars. I. Precise Spectral Types for 372 Stars. AJ, 121(4):2148–2158, April 2001. doi: 10.1086/319956.

R. O. Gray, C. J. Corbally, R. F. Garrison, M. T. McFadden, and P. E. Robinson. Contributions to the Nearby Stars (NStars) Project: Spectroscopy of Stars Earlier than M0 within 40 Parsecs: The Northern Sample. I. AJ, 126(4):2048–2059, October 2003. doi: 10.1086/378365.

R. O. Gray, C. J. Corbally, R. F. Garrison, M. T. McFadden, E. J. Bubar, C. E. McGahee, A. A. O'Donoghue, and E. R. Knox. Contributions to the Nearby Stars (NStars) Project: Spectroscopy of Stars Earlier than M0 within 40 pc-The Southern Sample. AJ, 132(1): 161–170, July 2006. doi: 10.1086/504637.

N. Grieves, J. Ge, N. Thomas, K. Willis, B. Ma, D. Lorenzo-Oliveira, A. B. A. Queiroz,

L. Ghezzi, C. Chiappini, F. Anders, L. Dutra-Ferreira, G. F. Porto de Mello, B. X. Santiago, L. N. da Costa, R. L. C. Ogando, E. F. del Peloso, J. C. Tan, D. P. Schneider, J. Pepper, K. G. Stassun, B. Zhao, D. Bizyaev, and K. Pan. Chemo-kinematics of the Milky Way from the SDSS-III MARVELS survey. MNRAS, 481(3):3244–3265, December 2018. doi: 10.1093/mnras/sty2431.

George E. Hale. On the Probable Existence of a Magnetic Field in Sun-Spots. ApJ, 28:315, November 1908. doi: 10.1086/141602.

George E. Hale, Ferdinand Ellerman, S. B. Nicholson, and A. H. Joy. The Magnetic Polarity of Sun-Spots. ApJ, 49:153, April 1919. doi: 10.1086/142452.

Jeffrey C. Hall. Stellar Chromospheric Activity. *Living Reviews in Solar Physics*, 5(1):2, December 2008. doi: 10.12942/lrsp-2008-2.

Arnold Hanslmeier. *Einführung in Astronomie und Astrophysik*. Springer Berlin Heidelberg Imprint: Springer Spektrum, Berlin Heidelberg, 4th ed. 2020 edition, 2020. ISBN 9783662604137.

Charles R. Harris, K. Jarrod Millman, Stéfan J. van der Walt, Ralf Gommers, Pauli Virtanen, David Cournapeau, Eric Wieser, Julian Taylor, Sebastian Berg, Nathaniel J. Smith, Robert Kern, Matti Picus, Stephan Hoyer, Marten H. van Kerkwijk, Matthew Brett, Allan Haldane, Jaime Fernández del Río, Mark Wiebe, Pearu Peterson, Pierre Gérard-Marchant, Kevin Sheppard, Tyler Reddy, Warren Weckesser, Hameer Abbasi, Christoph Gohlke, and Travis E. Oliphant. Array programming with NumPy. *Nature*, 585(7825):357–362, September 2020. doi: 10.1038/s41586-020-2649-2. URL `https://doi.org/10.1038/s41586-020-2649-2`.

L. Hartmann, D. R. Soderblom, R. W. Noyes, N. Burnham, and A. H. Vaughan. An analysis of the Vaughan-Preston survey of chromospheric emission. ApJ, 276:254–265, January 1984. doi: 10.1086/161609.

David H. Hathaway. The Solar Cycle. *Living Reviews in Solar Physics*, 12(1):4, December 2015. doi: 10.1007/lrsp-2015-4.

C. Hellier, D. R. Anderson, A. Collier Cameron, L. Delrez, M. Gillon, E. Jehin, M. Lendl, P. F. L. Maxted, M. Neveu-VanMalle, F. Pepe, D. Pollacco, D. Queloz, D. Ségransan, B. Smalley, J. Southworth, A. H. M. J. Triaud, S. Udry, T. Wagg, and R. G. West. WASP-South transiting exoplanets: WASP-130b, WASP-131b, WASP-132b, WASP-139b, WASP-140b, WASP-141b and WASP-142b. MNRAS, 465(3):3693–3707, March 2017. doi: 10.1093/mnras/stw3005.

N. Houk and M. Smith-Moore. *Michigan Catalogue of Two-dimensional Spectral Types for the HD Stars. Volume 4, Declinations -26°.0 to -12°.0.*, volume 4. 1988.

J. D. Hunter. Matplotlib: A 2d graphics environment. *Computing in Science & Engineering*, 9(3):90–95, 2007. doi: 10.1109/MCSE.2007.55.

Howard Isaacson and Debra Fischer. Chromospheric Activity and Jitter Measurements for 2630 Stars on the California Planet Search. ApJ, 725(1):875–885, December 2010. doi: 10.1088/0004-637X/725/1/875.

E. Johnson. Stellar Activity and Radial Velocities in M Dwarfs. *eDiss - SUB Göttingen (Zentralbibliothek)*, July 2024. doi: http://dx.doi.org/10.53846/goediss-10619.

Philip G. Judge, Ricky Egeland, Travis S. Metcalfe, Edward Guinan, and Scott Engle. The Magnetic Future of the Sun. ApJ, 848(1):43, October 2017. doi: 10.3847/1538-4357/aa8d6a.

Mario Jurić, Željko Ivezić, Alyson Brooks, Robert H. Lupton, David Schlegel, Douglas Finkbeiner, Nikhil Padmanabhan, Nicholas Bond, Branimir Sesar, Constance M. Rockosi, Gillian R. Knapp, James E. Gunn, Takahiro Sumi, Donald P. Schneider, J. C. Barentine, Howard J. Brewington, J. Brinkmann, Masataka Fukugita, Michael Harvanek, S. J. Kleinman, Jurek Krzesinski, Dan Long, Jr. Neilsen, Eric H., Atsuko Nitta, Stephanie A. Snedden, and Donald G. York. The Milky Way Tomography with SDSS. I. Stellar Number Density Distribution. ApJ, 673(2):864–914, February 2008. doi: 10.1086/523619.

Philip C. Keenan and Raymond C. McNeil. The Perkins Catalog of Revised MK Types for the Cooler Stars. ApJS, 71:245, October 1989. doi: 10.1086/191373.

M. Lendl, D. R. Anderson, A. Bonfanti, F. Bouchy, A. Burdanov, A. Collier Cameron, L. Delrez, M. Gillon, C. Hellier, E. Jehin, P. F. L. Maxted, L. Dyregaard Nielsen, F. Pepe, D. Pollacco, D. Queloz, D. Ségransan, J. Southworth, B. Smalley, S. Thompson, O. Turner, A. H. M. J. Triaud, S. Udry, and R. G. West. WASP-147b, 160Bb, 164b, and 165b: two hot Saturns and two Jupiters, including two planets with metal-rich hosts. MNRAS, 482 (1):301–312, January 2019. doi: 10.1093/mnras/sty2667.

Jeffrey L. Linsky. Stellar Model Chromospheres and Spectroscopic Diagnostics. ARA&A, 55(1):159–211, August 2017. doi: 10.1146/annurev-astro-091916-055327.

V. Loaiza-Tacuri, Katia Cunha, Verne V. Smith, F. Quispe-Huaynasi, Ellen Costa-Almeida, Luan Ghezzi, and Jorge Melendez. Stellar Characterization and a Chromospheric Activity Analysis of a K2 Sample of Planet-hosting Stars. ApJ, 970(1):53, July 2024. doi: 10.3847/1538-4357/ad4b15.

C. Lovis, X. Dumusque, N. C. Santos, F. Bouchy, M. Mayor, F. Pepe, D. Queloz, D. Ségransan, and S. Udry. The HARPS search for southern extra-solar planets. XXXI. Magnetic activity cycles in solar-type stars: statistics and impact on precise radial velocities. *arXiv e-prints*, art. arXiv:1107.5325, July 2011. doi: 10.48550/arXiv.1107.5325.

L. Magrini, C. Danielski, D. Bossini, M. Rainer, D. Turrini, S. Benatti, A. Brucalassi, M. Tsantaki, E. Delgado Mena, N. Sanna, K. Biazzo, T. L. Campante, M. Van der Swaelmen, S. G. Sousa, K. G. Hełminiak, A. W. Neitzel, V. Adibekyan, G. Bruno, and G. Casali. Ariel stellar characterisation. I. Homogeneous stellar parameters of 187 FGK planet host stars: Description and validation of the method. A&A, 663:A161, July 2022. doi: 10.1051/0004-6361/202243405.

E. E. Mamajek, G. Torres, A. Prsa, P. Harmanec, M. Asplund, P. D. Bennett, N. Capitaine, J. Christensen-Dalsgaard, E. Depagne, W. M. Folkner, M. Haberreiter, S. Hekker, J. L. Hilton, V. Kostov, D. W. Kurtz, J. Laskar, B. D. Mason, E. F. Milone, M. M. Montgomery, M. T. Richards, J. Schou, and S. G. Stewart. IAU 2015 Resolution B2 on Recommended

Zero Points for the Absolute and Apparent Bolometric Magnitude Scales. *arXiv e-prints*, art. arXiv:1510.06262, October 2015. doi: 10.48550/arXiv.1510.06262.

J. T. Mariska. The solar transition region. *Cambridge Astrophysics Series*, 23, January 1992.

S. C. Marsden, P. Petit, S. V. Jeffers, J. Morin, R. Fares, A. Reiners, J. D. do Nascimento, M. Aurière, J. Bouvier, B. D. Carter, C. Catala, B. Dintrans, J. F. Donati, T. Gastine, M. Jardine, R. Konstantinova-Antova, J. Lanoux, F. Lignières, A. Morgenthaler, J. C. Ramìrez-Vèlez, S. Théado, V. Van Grootel, and BCool Collaboration. A BCool magnetic snapshot survey of solar-type stars. MNRAS, 444(4):3517–3536, November 2014. doi: 10.1093/mnras/stu1663.

C. J. Marvin, A. Reiners, G. Anglada-Escudé, S. V. Jeffers, and S. Boro Saikia. Absolute Ca II H & K and H-alpha flux measurements of low-mass stars: Extending R'$_{HK}$ to M dwarfs. A&A, 671:A162, March 2023. doi: 10.1051/0004-6361/201937306.

M. Mayor, F. Pepe, D. Queloz, F. Bouchy, G. Rupprecht, G. Lo Curto, G. Avila, W. Benz, J. L. Bertaux, X. Bonfils, Th. Dall, H. Dekker, B. Delabre, W. Eckert, M. Fleury, A. Gilliotte, D. Gojak, J. C. Guzman, D. Kohler, J. L. Lizon, A. Longinotti, C. Lovis, D. Megevand, L. Pasquini, J. Reyes, J. P. Sivan, D. Sosnowska, R. Soto, S. Udry, A. van Kesteren, L. Weber, and U. Weilenmann. Setting New Standards with HARPS. *The Messenger*, 114:20–24, December 2003.

Michel Mayor and Didier Queloz. A Jupiter-mass companion to a solar-type star. Nature, 378(6555):355–359, November 1995. doi: 10.1038/378355a0.

N. Meunier, M. Kretzschmar, R. Gravet, L. Mignon, and X. Delfosse. Relationship between Ca and Hα chromospheric emission in F-G-K stars: Indication of stellar filaments? A&A, 658:A57, February 2022. doi: 10.1051/0004-6361/202142120.

F. Middelkoop. Magnetic structure in cool stars. IV - Rotation and CA II H and K emission of main-sequence stars. A&A, 107(1):31–35, March 1982a.

Frans Middelkoop. *Ca II H and K emission from late-type stars.* PhD thesis, University of Utrecht, Netherlands, January 1982b.

M. Mittag, J. H. M. M. Schmitt, and K. P. Schröder. Ca II H+K fluxes from S-indices of large samples: a reliable and consistent conversion based on PHOENIX model atmospheres. A&A, 549:A117, January 2013. doi: 10.1051/0004-6361/201219868.

R. W. Noyes, L. W. Hartmann, S. L. Baliunas, D. K. Duncan, and A. H. Vaughan. Rotation, convection, and magnetic activity in lower main-sequence stars. ApJ, 279:763–777, April 1984. doi: 10.1086/161945.

L. Pasquini and R. Pallavicini. H-alpha absolute chromospheric fluxes in G and K dwarfs and subgiants. A&A, 251:199, November 1991.

A. G. M. Pietrow. *Physical properties of chromospheric features: Plage, peacock jets, and calibrating it all.* PhD thesis, Stockholm University, May 2022.

Adrian Price-Whelan, Brigitta Sipőcz, Daniel Lenz, Johnny Greco, Nathaniel Starkman, Dan

Foreman-Mackey, P. L. Lim, Semyeong Oh, Sergey Koposov, and Syrtis Major. adrn/gala: v1.3, October 2020. URL https://doi.org/10.5281/zenodo.4159870.

Adrian M. Price-Whelan. Gala: A python package for galactic dynamics. *The Journal of Open Source Software*, 2(18), oct 2017. doi: 10.21105/joss.00388. URL https://doi.org/10.21105%2Fjoss.00388.

G. Raskin, H. van Winckel, H. Hensberge, A. Jorissen, H. Lehmann, C. Waelkens, G. Avila, J. P. de Cuyper, P. Degroote, R. Dubosson, L. Dumortier, Y. Frémat, U. Laux, B. Michaud, J. Morren, J. Perez Padilla, W. Pessemier, S. Prins, K. Smolders, S. van Eck, and J. Winkler. HERMES: a high-resolution fibre-fed spectrograph for the Mercator telescope. A&A, 526:A69, February 2011. doi: 10.1051/0004-6361/201015435.

A. Reiners and G. Basri. Chromospheric Activity, Rotation, and Rotational Braking in M and L Dwarfs. ApJ, 684(2):1390–1403, September 2008. doi: 10.1086/590073.

R. G. M. Rutten. Magnetic structure in cool stars. VII. Absolute surface flux in CA IIH and K line cores. A&A, 130:353–360, January 1984.

D. Salabert, R. A. García, P. G. Beck, R. Egeland, P. L. Pallé, S. Mathur, T. S. Metcalfe, Jr. do Nascimento, J. D., T. Ceillier, M. F. Andersen, and A. Triviño Hage. Photospheric and chromospheric magnetic activity of seismic solar analogs. Observational inputs on the solar-stellar connection from Kepler and Hermes. A&A, 596:A31, November 2016a. doi: 10.1051/0004-6361/201628583.

D. Salabert, C. Régulo, R. A. García, P. G. Beck, J. Ballot, O. L. Creevey, F. Pérez Hernández, Jr. do Nascimento, J. D., E. Corsaro, R. Egeland, S. Mathur, T. S. Metcalfe, L. Bigot, T. Ceillier, and P. L. Pallé. Magnetic variability in the young solar analog KIC 10644253. Observations from the Kepler satellite and the HERMES spectrograph. A&A, 589:A118, May 2016b. doi: 10.1051/0004-6361/201527978.

C. J. Schrijver and C. Zwaan. *Solar and Stellar Magnetic Activity*. Cambridge Astrophysics. Cambridge University Press, 2000.

C. Schröder, A. Reiners, and J. H. M. M. Schmitt. Ca II HK emission in rapidly rotating stars. Evidence for an onset of the solar-type dynamo. A&A, 493(3):1099–1107, January 2009. doi: 10.1051/0004-6361:200810377.

A. Skumanich. Time Scales for Ca II Emission Decay, Rotational Braking, and Lithium Depletion. ApJ, 171:565, February 1972. doi: 10.1086/151310.

A. G. Sreejith, L. Fossati, A. Youngblood, K. France, and S. Ambily. Ca II H&K stellar activity parameter: a proxy for extreme ultraviolet stellar fluxes. A&A, 644:A67, December 2020. doi: 10.1051/0004-6361/202039167.

A. Suárez Mascareño, R. Rebolo, and J. I. González Hernández. Magnetic cycles and rotation periods of late-type stars from photometric time series. A&A, 595:A12, October 2016. doi: 10.1051/0004-6361/201628586.

Giovanna Tinetti, Pierre Drossart, Paul Eccleston, Paul Hartogh, Astrid Heske, Jérémy Leconte, Giusi Micela, Marc Ollivier, Göran Pilbratt, Ludovic Puig, Diego Turrini, Bart

Vandenbussche, Paulina Wolkenberg, Jean-Philippe Beaulieu, Lars A. Buchave, Martin Ferus, Matt Griffin, Manuel Guedel, Kay Justtanont, Pierre-Olivier Lagage, Pedro Machado, Giuseppe Malaguti, Michiel Min, Hans Ulrik Nørgaard-Nielsen, Mirek Rataj, Tom Ray, Ignasi Ribas, Mark Swain, Robert Szabo, Stephanie Werner, Joanna Barstow, Matt Burleigh, James Cho, Vincent Coudé du Foresto, Athena Coustenis, Leen Decin, Therese Encrenaz, Marina Galand, Michael Gillon, Ravit Helled, Juan Carlos Morales, Antonio García Muñoz, Andrea Moneti, Isabella Pagano, Enzo Pascale, Giuseppe Piccioni, David Pinfield, Subhajit Sarkar, Franck Selsis, Jonathan Tennyson, Amaury Triaud, Olivia Venot, Ingo Waldmann, David Waltham, Gillian Wright, Jerome Amiaux, Jean-Louis Auguères, Michel Berthé, Naidu Bezawada, Georgia Bishop, Neil Bowles, Deirdre Coffey, Josep Colomé, Martin Crook, Pierre-Elie Crouzet, Vania Da Peppo, Isabel Escudero Sanz, Mauro Focardi, Martin Frericks, Tom Hunt, Ralf Kohley, Kevin Middleton, Gianluca Morgante, Roland Ottensamer, Emanuele Pace, Chris Pearson, Richard Stamper, Kate Symonds, Miriam Rengel, Etienne Renotte, Peter Ade, Laura Affer, Christophe Alard, Nicole Allard, Francesca Altieri, Yves André, Claudio Arena, Ioannis Argyriou, Alan Aylward, Cristian Baccani, Gaspar Bakos, Marek Banaszkiewicz, Mike Barlow, Virginie Batista, Giancarlo Bellucci, Serena Benatti, Pernelle Bernardi, Bruno Bézard, Maria Blecka, Emeline Bolmont, Bertrand Bonfond, Rosaria Bonito, Aldo S. Bonomo, John Robert Brucato, Allan Sacha Brun, Ian Bryson, Waldemar Bujwan, Sarah Casewell, Bejamin Charnay, Cesare Cecchi Pestellini, Guo Chen, Angela Ciaravella, Riccardo Claudi, Rodolphe Clédassou, Mario Damasso, Mario Damiano, Camilla Danielski, Pieter Deroo, Anna Maria Di Giorgio, Carsten Dominik, Vanessa Doublier, Simon Doyle, René Doyon, Benjamin Drummond, Bastien Duong, Stephen Eales, Billy Edwards, Maria Farina, Ettore Flaccomio, Leigh Fletcher, François Forget, Steve Fossey, Markus Fränz, Yuka Fujii, Álvaro García-Piquer, Walter Gear, Hervé Geoffray, Jean Claude Gérard, Lluis Gesa, H. Gomez, Rafał Graczyk, Caitlin Griffith, Denis Grodent, Mario Giuseppe Guarcello, Jacques Gustin, Keiko Hamano, Peter Hargrave, Yann Hello, Kevin Heng, Enrique Herrero, Allan Hornstrup, Benoit Hubert, Shigeru Ida, Masahiro Ikoma, Nicolas Iro, Patrick Irwin, Christopher Jarchow, Jean Jaubert, Hugh Jones, Queyrel Julien, Shingo Kameda, Franz Kerschbaum, Pierre Kervella, Tommi Koskinen, Matthijs Krijger, Norbert Krupp, Marina Lafarga, Federico Landini, Emanuel Lellouch, Giuseppe Leto, A. Luntzer, Theresa Rank-Lüftinger, Antonio Maggio, Jesus Maldonado, Jean-Pierre Maillard, Urs Mall, Jean-Baptiste Marquette, Stephane Mathis, Pierre Maxted, Taro Matsuo, Alexander Medvedev, Yamila Miguel, Vincent Minier, Giuseppe Morello, Alessandro Mura, Norio Narita, Valerio Nascimbeni, N. Nguyen Tong, Vladimiro Noce, Fabrizio Oliva, Enric Palle, Paul Palmer, Maurizio Pancrazzi, Andreas Papageorgiou, Vivien Parmentier, Manuel Perger, Antonino Petralia, Stefano Pezzuto, Ray Pierrehumbert, Ignazio Pillitteri, Giampaolo Piotto, Giampaolo Pisano, Loredana Prisinzano, Aikaterini Radioti, Jean-Michel Réess, Ladislav Rezac, Marco Rocchetto, Albert Rosich, Nicoletta Sanna, Alexandre Santerne, Giorgio Savini, Gaetano Scandariato, Bruno Sicardy, Carles Sierra, Giuseppe Sindoni, Konrad Skup, Ignas Snellen, Mateusz Sobiecki, Lauriane Soret, Alessandro Sozzetti, A. Stiepen, Antoine Strugarek, Jake Taylor, William Taylor, Luca Terenzi, Marcell Tessenyi, Angelos Tsiaras, C. Tucker, Diana Valencia, Gautam Vasisht, Allona Vazan, Francesc Vilardell, Sabrine Vinatier, Serena Viti, Rens Waters, Piotr Wawer, Anna Wawrzaszek, Anthony Whitworth, Yuk L. Yung, Sergey N. Yurchenko, María Rosa Zapatero Osorio, Robert Zellem, Tiziano Zingales, and Frans Zwart. A chemical survey of exoplanets with ARIEL. *Experimental Astronomy*, 46(1):135–209, November 2018. doi: 10.1007/s10686-018-9598-x.

A. H. Vaughan and G. W. Preston. A survey of chromospheric CA II H and K emission in field stars of the solar neighborhood. PASP, 92:385–391, August 1980. doi: 10.1086/130683.

A. H. Vaughan, G. W. Preston, and O. C. Wilson. Flux measurements of Ca II and K emission. PASP, 90:267–274, June 1978. doi: 10.1086/130324.

Michael L. Waskom. seaborn: statistical data visualization. *Journal of Open Source Software*, 6(60):3021, 2021. doi: 10.21105/joss.03021. URL `https://doi.org/10.21105/joss.03021`.

Alfred Weigert. *Astronomie und Astrophysik : ein Grundkurs*. WILEY-VCH, Weinheim, 5., aktualis. u. erw. aufl. edition, 2009. ISBN 9783527407934.

M. Wenger, F. Ochsenbein, D. Egret, P. Dubois, F. Bonnarel, S. Borde, F. Genova, G. Jasniewicz, S. Laloë, S. Lesteven, and R. Monier. The SIMBAD astronomical database. The CDS reference database for astronomical objects. A&AS, 143:9–22, April 2000. doi: 10.1051/aas:2000332.

Russel J. White, Jared M. Gabor, and Lynne A. Hillenbrand. High-Dispersion Optical Spectra of Nearby Stars Younger Than the Sun. AJ, 133(6):2524–2536, June 2007. doi: 10.1086/514336.

O. C. Wilson. Flux Measurements at the Centers of Stellar H- and K-Lines. ApJ, 153:221, July 1968. doi: 10.1086/149652.

O. C. Wilson. Chromospheric variations in main-sequence stars. ApJ, 226:379–396, December 1978. doi: 10.1086/156618.